ELECTRICAL ENGINEERING AND ENERGY



ISSN: 3062-3979

VOLUME 4, ISSUE 1, 2025

Electrical Engineering and Energy
Volume 4, Issue 1, Published: April 30, 2025
ISSN: 3062-3979

Editors in Chief

Prof.Dr. Hasan Aydoğan
haydoğan@selcuk.edu.tr
Selçuk University

Prof. Dr. Mehmet Çunkaş
mcunkas@selcuk.edu.tr
Selçuk University

Editorial Board

Prof. Dr. Jürgen Krahl
praesident@th-owl.de
Technische Hochschule Ostwestfalan-Lippe University Of Applied Science And Arts, Germany

Prof. Dr. Nídia de Sá Caetano
nsc@isep.ipp.pt
Polytechnic Institute of Porto, Portugal

Dr. Sara Rajabihamedani
sara.rajabi@unitus.it
University degli studi della Tuscia, Italy

Assoc. Prof. Dr. Mario HIRZ
mario.hirz@tugraz.at
Graz University of Technology, Austria

Prof. Dr. Ahmet Duran Şahin
sahind@itu.edu.tr
Istanbul Technical University, Türkiye

Prof. Dr. Arif Hepbaşlı
arif.hepbasli@yasar.edu.tr
Yasar University, Türkiye

Prof. Dr. Mustafa Acaroğlu
acaroglu@selcuk.edu.tr
Selcuk University, Türkiye

Prof. Dr. Bülent Yeşilata
byesilata@ybu.edu.tr
Ankara Yildirim Beyazit University, Türkiye

Assoc. Prof. Dr. Hulusi Karaca
hkaraca@selcuk.edu.tr
Selçuk University, Türkiye

Assoc. Prof. Dr. Teodora Hristova
teodora@mgu.bg
University of Mining and Geology “St. Ivan Rilski, Bulgaria

Assoc. Prof . Dr. Mümtaz Mutluer
mmutluer@ktun.edu.tr
Konya Technical University, Türkiye

Dr. Mustafa Nevzat Örnek
mnornek@ktun.edu.tr
Konya Technical University, Türkiye

Dr. Kaisan Muhammad Usman
mukaisan@abu.edu.ng
Ahmadu Bello University, Zaria, Nigeria

Electrical Engineering and Energy
Volume 4, Issue 1, Published: April 30, 2025

Content

Moving Average Filter based DSTATCOM Control Approach
Ali Sait Özer, Fehmi Sevilmiş, Hulusi Karaca
Pages:1-10

A Comparative Analysis of Genetic Algorithm Replacement Strategies in a Real-World Optimization Problem: An Elitism and Diversity Oriented Perspective
Hüseyin Doğan
Pages:11-32

Investigation of the Effects of TiO_2 and Al_2O_3 Nanoparticles on Exhaust Gas Temperature in Direct Injection Gasoline Engines
Mustafa Selman Gokmen, Hasan Aydogan
Pages:33-39

Comparative Analysis of Grid-Following (GFL) and Grid-Forming (GFM) Inverters: Control and Transition Capabilities
Fatih Burak, Hulusi Karaca
Pages:40-51

Evaluation of Magnet Demagnetization Behavior in Permanent Magnet Linear Synchronous Motors
Enes Yücel, Mehmet Çunkaş, Łukasz Knypiński
Pages:52-63

ELECTRICAL ENGINEERING AND ENERGY

OPEN ACCESS

A Moving Average Filter based DSTATCOM Control Approach

Ali Sait Özer[1], Fehmi Sevilmiş[2], and Hulusi Karaca[2]

[1] Dept. of Control and Automation Technology, Konya Technical University, Konya, Türkiye
[2] Dept. of Electrical and Electronics Engineering, Selçuk University, Konya, Türkiye

Submitted: 5 April 2025
Accepted: 28 April 2025
Published: 30 April 2025

Corresponding author
Ali Sait Özer,
asozer@ktun.edu.tr

Copyright, Distributed under Creative Commons CC-BY 4.0

Abstract: Self-excited induction generators (SEIGs) are commonly preferred in stand-alone renewable energy systems due to their low cost and robust construction. However, the voltage and frequency stability at the SEIG output may be adversely affected by varying reactive and active power demands depending on the load profile. In such systems, DSTATCOM is used to provide voltage and frequency regulation, and its performance largely depends on the applied control algorithm. In this study, a moving average filter (MAF) based *dq* control algorithm is proposed for DSTATCOM supported SEIG systems. The MAF structure contributes to more accurate calculation of reference source currents by reducing the effect of harmonic content. The proposed control method is tested under nonlinear load and unbalanced-nonlinear load conditions. The results show that the system maintains voltage and frequency stability and successfully suppresses disturbances.

Keywords Distribution Static Compensator (DSTATCOM), Moving Average Filter (MAF), Self-Excited Induction Generator (SEIG), Wind Energy.

1. Introduction

The importance of renewable energy sources is increasing in accordance with the increasing global energy demand and environmental sustainability targets. Among these sources, wind energy stands out with its clean, inexhaustible, and low operating cost structure and is considered as a strategic alternative (Kundu et al. 2024). The generator technology used in wind turbines plays a direct determining role in the efficiency, reliability and power quality of the system.

Self-Excited Induction Generators (SEIGs) stand out with their low cost, robust construction, brushless rotor systems and low maintenance requirements, especially in small-scale off-grid applications (Sibrahim et al. 2024). In addition, standard asynchronous machines can be used as generators with a simple capacitor bank, making SEIG systems an economical and accessible solution. In this respect, they are widely preferred in rural areas, mobile energy systems and microgrids based on variable energy sources such as wind. However, SEIGs have a sensitive structure against load changes. This is because the output voltage and frequency of the generator can only remain at reference values if the active power balance as well as the reactive power demanded by the load and the SEIG is correctly balanced. As the load profile changes, the active power demand changes as well as the reactive power demand, which may cause voltage

fluctuations and rotor speed deviations in the SEIG system and adversely affect the frequency stability. Therefore, the regulation of SEIG output in terms of both voltage and frequency requires the system to have a control infrastructure that can react flexibly and quickly to dynamic conditions (Shailly et al. 2025)

To meet this requirement, passive compensation methods such as fixed capacitor banks were first used to provide the reactive power demanded by the SEIG and the load, and then solutions such as thyristor-controlled Static Var Compensator (SVC) were developed. Although these systems offer attractive options due to their low cost and applicability, they are insufficient to meet the dynamic needs of the systems due to their limited response speed to sudden load changes, their inability to suppress harmonic distortions and their low sensitivity in voltage regulation. In addition, these methods can only provide reactive power compensation; since they cannot provide active power support, they cannot contribute to frequency regulation in SEIG systems. Especially under harmonic and unbalanced load conditions, these limitations become more apparent and have negative effects on system stability, power quality and reliability. To overcome these disadvantages, active power electronics-based solutions, especially Distribution Static Compensator (DSTATCOM) topologies come to the fore (Giri et al. 2020). DSTATCOM offers an effective solution for SEIG systems thanks to its ability to react quickly to sudden changes in load and to perform both reactive power compensation and harmonic suppression functions simultaneously. DSTATCOM, which can dynamically adapt to different load scenarios thanks to its power electronics-based structure, ensures that the system voltage remains at the reference value, while also improving power quality (Ozer et al. 2024). On the other hand, for the SEIG output frequency to remain stable, the active power drawn from the generator must be kept in balance. Sudden changes in the load may disturb this balance and cause fluctuations in the rotor speed and thus frequency deviations. To stabilize this situation, an battery energy storage system (BESS) is integrated into the DSTATCOM structure to provide not only reactive but also active power support. Thus, a part of the active power requirement of the system is met through DSTATCOM, relieving the load on the SEIG and keeping the frequency constant.

The effectiveness of DSTATCOM directly depends on the performance of the control algorithm. In this context, there are various control methods developed in literature. Methods such as Instantaneous Reactive Power Theory (IRPT), Synchronous Reference Frame (*dq*) and Current Synchronous Detection (CSD) are widely used to calculate the reference currents required for the control of DSTATCOM (Ram et al. 2024). Among these methods, the *dq* method stands out due to its time-invariant (DC level) components, high immunity to harmonics and ease of application (Rajendran et al. 2013).

Low Pass Filters (LPFs) are generally used during the separation of load current components in SRF structure. However, these filters may cause performance losses in harmonic and unbalanced load conditions. While LPFs cause phase delay and accuracy loss in transient states, they are insufficient especially in suppressing low frequency harmonics. In addition, asymmetric behavior between phases under unbalanced load conditions adversely affects the stability of classical filtering structures.

In this study, the advantages of the *dq*-based structure are retained; however, a control algorithm is proposed by integrating a moving average filter (MAF) instead of classical LPF modules. MAF provides a more stable filtering in transient states by averaging the signal over the time window. MAF, which is more effective than LPF in suppressing sudden fluctuations especially in signals containing harmonics, produces accurate reference current components by better tolerating under unbalanced load conditions. Thus, DSTATCOM can intervene in the SEIG system faster and more accurately, significantly increasing system performance in terms of voltage regulation, SEIG frequency and power quality.

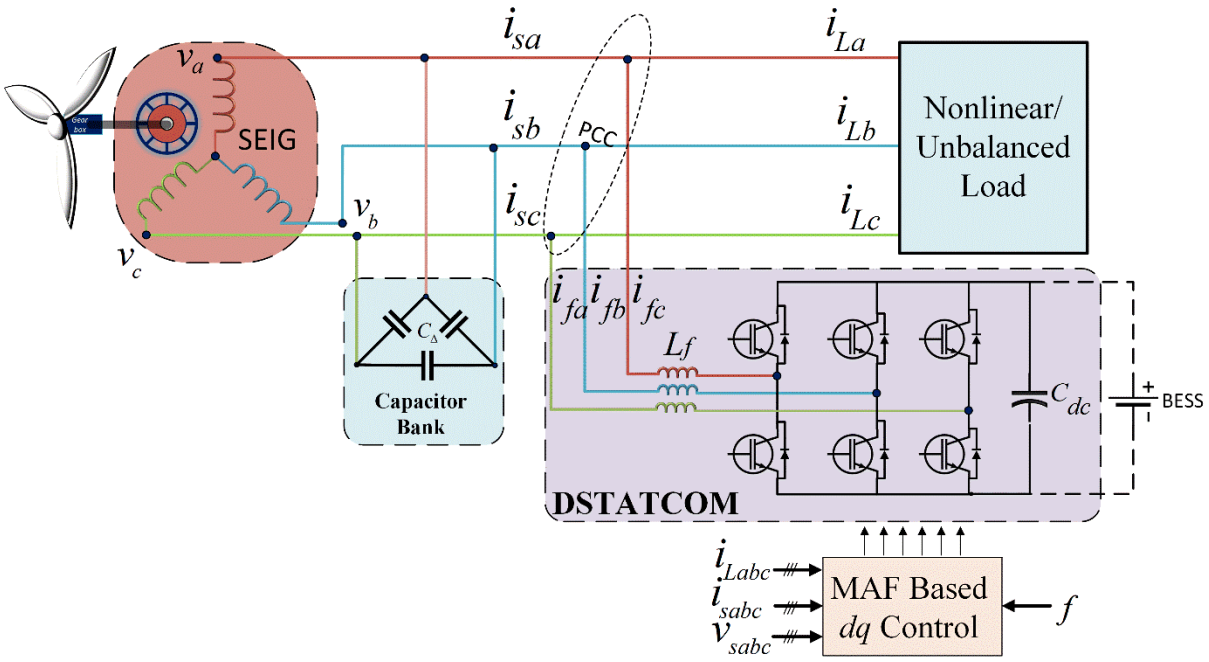

Figure 1 Schematic of DSTATCOM-based SEIG system

2. DSTATCOM-based SEIG System

Figure 1 shows the general structure of the DSTATCOM supported SEIG system. The system consists of a self-excited induction generator (SEIG), delta-connected excitation capacitors, nonlinear/unbalanced loads, and DSTATCOM-assisted energy storage system (BESS) providing active and reactive power. The reactive power required for the magnetization of the SEIG is provided by the capacitor banks; these capacitors are also involved in the suppression of harmonic components caused by the high switching frequency of the voltage source converter (VSC) (Chilipi et al. 2020).

DSTATCOM is connected in parallel with the point of common coupling (PCC) of the system via three-phase coupling inductances (L_f). DSTATCOM supports voltage regulation by activating to meet the reactive power requirements of both SEIG and the load in case of load changes. It also contributes to frequency regulation by providing active power through the integrated BESS structure and keeps the active load on the SEIG constant.

VSC, which is the main component of DSTATCOM, consists of insulated gated bipolar transistors (IGBTs) and generates three-phase output voltage through PWM control signals.

3. MAF-based *dq* control method

Figure 2 presents the block diagram of the proposed MAF-based *dq* control method. In this structure, the load currents are subjected to abc-*dq* conversion and the fundamental components of the obtained i_{Ld} and i_{Lq} are obtained using a moving average filter (MAF). Thus, the harmonic content is filtered, and a more stable structure is created for reference current calculations. The obtained active and reactive current components are processed by PI controllers; thus, reference source currents i_{sa}^* i_{sb}^* and i_{sc}^* are generated and VSC is controlled based on these currents.

3.1 Description of the suggested MAF

The LPFs used to filter i_{Ld} and i_{Lq} suffer from two problems: they lead to the phase delay and cannot

sufficiently suppress harmonic components caused by nonlinear and unbalanced loads. To address these challenges, in this paper, moving average filters (MAFs) are utilized instead of LPFs, as can be seen in Figure 2. The MAF structure is uncomplicated and straightforward to implement, which has contributed to its growing popularity in recent times (Ozer et al. 2022).

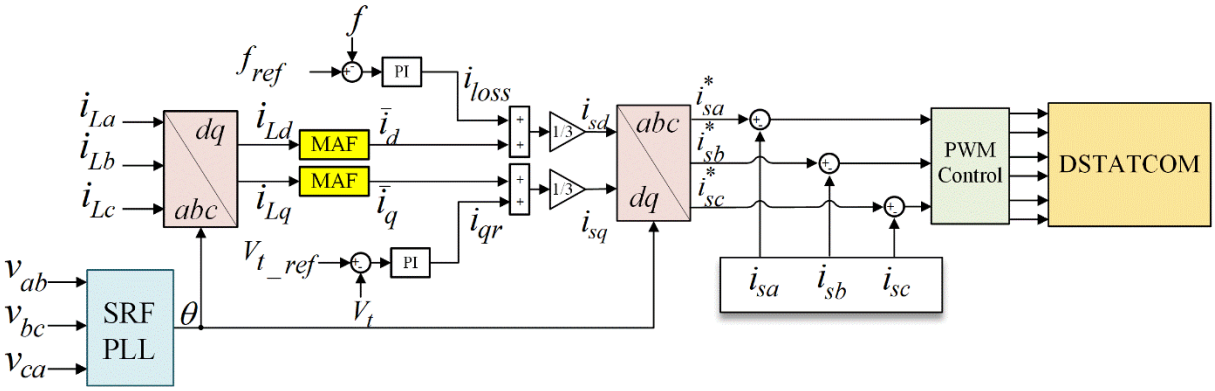

Figure 2 Block diagram of the MAF-based *dq* method

The MAF can act as an ideal LPF in certain cases. Its s-domain and z-domain transfer functions can be expressed as (Golestan et al. 2014)

$$\mathrm{MAF(s)} = \frac{1-e^{-T_\omega s}}{T_\omega s} \tag{1}$$

$$\mathrm{MAF(s)} = \frac{1}{N}\frac{1-z^{-N}}{1-z^{-1}} \tag{2}$$

where T_ω and N stand for window-length of MAF and MAF's order, respectively. The MAF's order N is defined as $f_s T_\omega$, where f_s is the sampling frequency. Using (2), the block diagram of MAF for digital implementation can be easily obtained, as illustrated in Figure 3. As demonstrated, its simple structure facilitates straightforward implementation in DSTATCOM control based on *dq*-theory.

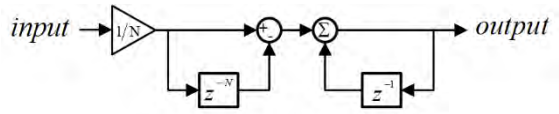

Figure 3 Block diagram of MAF for digital implementation

3.2 *dq*-based Method

The *dq*-based method developed for active and reactive power control in three-phase power systems provides with its fast and stable response to dynamic load changes. This method converts the three-phase quantities in the system to the synchronous reference frame; thus control operations are performed more precisely. The general structure of the method is presented as a block diagram in Figure 2.

When applying the *dq* method, the load currents (i_{Labc}), SEIG terminal voltages (v_{sabc}) and SEIG frequency (f) are measured and used as feedback signals. The measured load currents are transferred to the synchronous reference frame (abc-*dq* conversion) as in Equation (3)

$$\begin{bmatrix} i_{Ld} \\ i_{Lq} \end{bmatrix} = \frac{2}{3}\begin{bmatrix} \cos\omega t & \cos(\omega t-120) & \cos(\omega t+120) \\ \sin\omega t & \sin(\omega t-120) & \sin(\omega t+120) \end{bmatrix}\begin{bmatrix} i_{La} \\ i_{Lb} \\ i_{Lc} \end{bmatrix} \tag{3}$$

The *dq*-axis components of the load current, i_{Ld} and i_{Lq} contain both fundamental and harmonic

components. In this study, MAF is employed to extract the fundamental components of the load currents by suppressing the harmonic content. MAF enables it to attenuate harmonics effectively while providing a more stable output with reduced phase delay during transient conditions. The fundamental components obtained at the output of the MAF are defined as follows for use in reference to current calculations:

$$\overline{i_d} = MAF(i_{Ld}), \quad \overline{i_q} = MAF(i_{Lq}) \tag{4}$$

In addition, two PI controllers are used in the *dq*-based method. The first one is used to keep the output frequency of the system at a constant and stable level, while the other one is used to regulate the SEIG terminal voltage. In order for DSTATCOM to maintain frequency regulation, it is mandatory to generate a certain level of active current. Otherwise, the frequency of the system may deviate over time and the generator may become unstable.

The active current component i_{sd} used for frequency estimation is calculated based on the frequency feedback in the system. For this purpose, the measured system frequency f is compared with the reference frequency value f_{ref} and the error signal between them is applied to the input of the PI controller.

$$f_{er(n)} = f_{ref(n)} - f_{(n)} \tag{5}$$

The output signal obtained from the PI controller gives the i_{loss} component, which represents the active power demand of the system. This component is calculated as follows:

$$i_{loss(n)} = i_{lossn(n-1)} + K_{pd(n)}(f_{er(n)} - f_{er(n-1)}) + K_{id(n)} f_{er(n)} \tag{6}$$

The active current component i_{sd}, is calculated using the i_{loss} value generated at the output of the PI controller, as shown in Equation (7).

$$i_{sd} = \frac{i_{loss} + \overline{i_d}}{3} \tag{7}$$

To maintain the SEIG terminal voltage at a stable and desired level, the required reactive power must be accurately determined and supplied. For this purpose, the reactive component of the reference current, i_{sq}, is used to regulate the voltage amplitude. To calculate the i_{sq} component, the peak value of the SEIG terminal voltage must first be determined. The voltage amplitude is calculated as

$$V_t = \sqrt{\frac{2}{3}(V_{sa}^2 + V_{sb}^2 + V_{sc}^2)} \tag{8}$$

The calculated voltage peak value is compared with the reference voltage amplitude (V_{tref}) and the difference between them is applied to the input of the PI controller. The error signal for the terminal voltage amplitude of SEIG is expressed as

$$V_{ter(n)} = V_{tref(n)} - V_{t(n)} \tag{9}$$

In this context, V_{tref} is the reference value determined for the SEIG terminal voltage and $V_{t(n)}$ is the measured instantaneous SEIG terminal voltage. The output signal obtained from the PI controller gives the reactive current component i_{qr}, which is computed as

$$i_{qr(n)} = i_{dn(n-1)} + K_{pd(n)}(V_{te(n)} - V_{te(n-1)}) + K_{iq(n)} V_{te(n)} \tag{10}$$

Within this control framework, K_{pq} and K_{iq} represent the proportional and integral gains of the PI controller, respectively. Through this structure, the required reactive current component is obtained to maintain the

terminal voltage at the desired level. The reactive current component, i_{sq}, is calculated using the i_{qr} value generated at the output of the PI controller, as expressed in Equation (11).

$$i_{sq} = \frac{i_{qr} + \overline{i_q}}{3} \tag{11}$$

The obtained i_{sd} and i_{sq} components are used to calculate the three-phase reference source currents i_{sa}^*, i_{sb}^* and i_{sc}^* via the *dq*-abc inverse transform.

$$\begin{bmatrix} i_{sa}^* \\ i_{sb}^* \\ i_{sc}^* \end{bmatrix} = \begin{bmatrix} \cos\theta & \sin\theta & 1 \\ \cos(\theta - \frac{2\pi}{3}) & \sin(\theta - \frac{2\pi}{3}) & 1 \\ \cos(\theta + \frac{2\pi}{3}) & \sin(\theta + \frac{2\pi}{3}) & 1 \end{bmatrix} \begin{bmatrix} i_{sd} \\ i_{sq} \\ i_0^* \end{bmatrix} \tag{12}$$

After the reference source currents (i^*_{sabc}) are generated, these currents are compared with the measured instantaneous currents (i_{sabc}) of the SEIG. PWM pulses required are generated according to the error signal obtained. These PWM signals are applied to the IGBT switching elements to provide the required active and reactive power to the system. Thus, DSTATCOM provides precise and fast control to meet the active and reactive power requirement.

4. Results and Discussion

In this section, the performance of the proposed MAF-based *dq* control algorithm in a DSTATCOM-assisted SEIG system is evaluated. The analysis focuses on the behavior of the system under harsh operating scenarios with nonlinear loads and unbalanced-nonlinear load conditions. These conditions are frequently encountered in standalone applications and have a direct impact on system stability and power quality. Critical performance indicators such as voltage regulation, harmonic content reduction and phase balance are investigated to demonstrate the effectiveness of the proposed method.

4.1 Performance of DSTATCOM-based SEIG under nonlinear load

In the first test scenario, the behavior of the system under nonlinear loads is investigated. Nonlinear loads cause harmonic current generation, which is an important quality problem in power systems. These harmonics can lead to distortion of the voltage waveform, overheating of equipment, reduction of energy efficiency and malfunctions in sensitive devices. In real life, such loads are commonly found in many industrial and commercial applications such as three-phase diode rectifiers, regulated speed drives, welding machines, UPS systems and computer power supplies. Therefore, the ability of SEIG-based systems to maintain stable voltage regulation under nonlinear load conditions is vital for the overall power quality of the system. In this test, the response of the proposed MAF-based *dq* control structure to harmonic distortions is evaluated.

In Figures 4, the load currents (i_{L_abc}), DSTATCOM currents (i_{fabc}), SEIG currents (i_{sabc}), and SEIG terminal voltages (v_{ab}, v_{bc}, v_{ca}) of system for proposed MAF-based *dq* control approach are shown under nonlinear load. Figure 5 illustrates the amplitude of the SEIG voltages (V_t) and the SEIG frequency (f) under nonlinear load conditions.

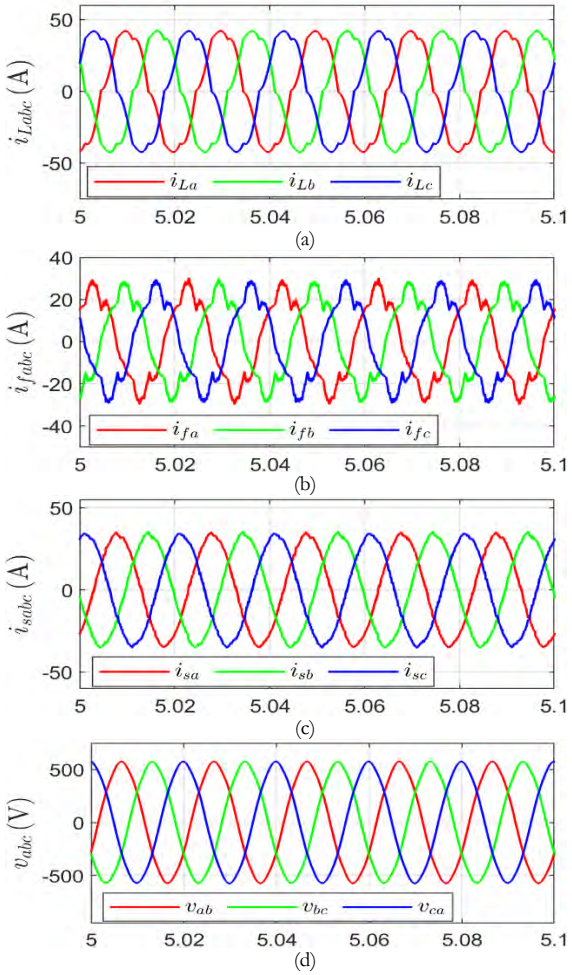

Figure 4 Performance of proposed MAF-based *dq* control method under nonlinear load (a) Load currents, (b) DSTATCOM currents, (c) SEIG currents, (d) SEIG terminal voltages

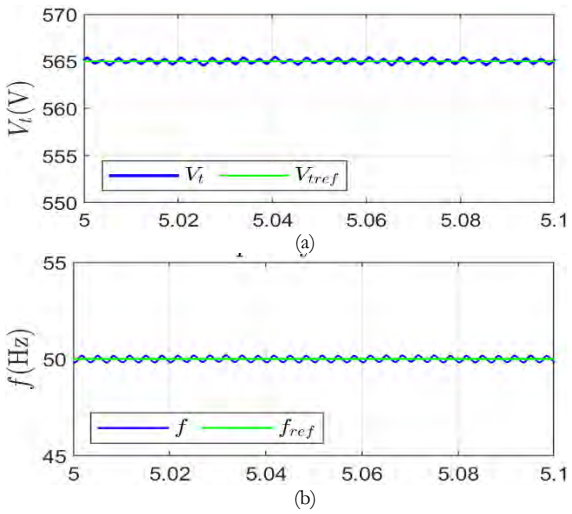

Figure 5 Performance of proposed MAF-based *dq* control method under nonlinear load (a) Amplitude of SEIG voltages, (b) SEIG frequency

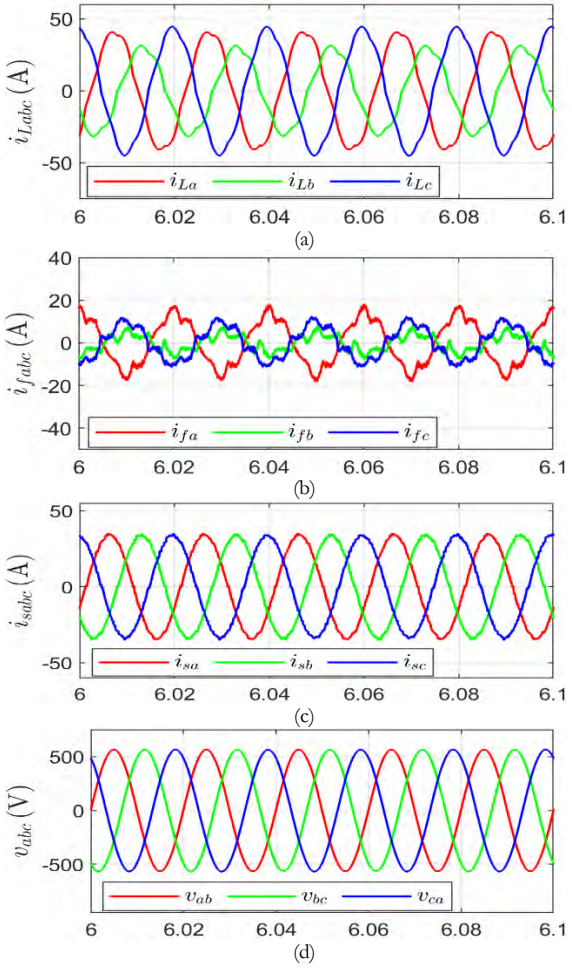

Figure 6 Performance of proposed MAF-based *dq* control method under nonlinear unbalanced load (a) Load currents, (b) DSTATCOM currents, (c) SEIG currents, (d) SEIG terminal voltages

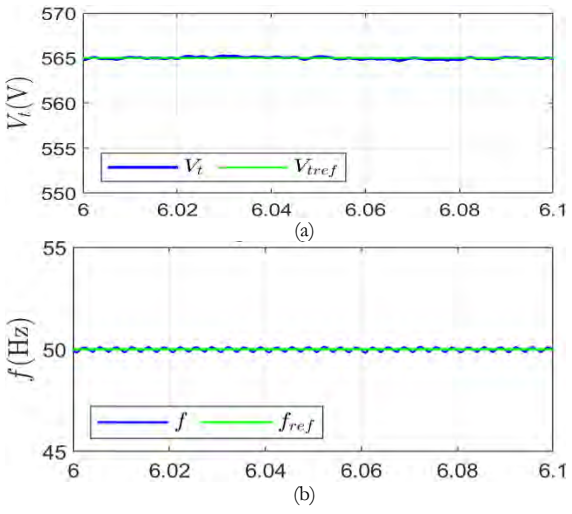

Figure 7 Performance of proposed MAF-based *dq* control method under nonlinear unbalanced load (a) Amplitude of SEIG voltages, (b) SEIG frequency

Figure 4(a) shows the load currents (i_{L_abc}) of the system under nonlinear load. The currents in all three phases contain significant and high frequency harmonic components. This clearly shows that nonlinear loads impose significant harmonic distortion on the system.

The phase currents (i_{fabc}) generated by the DSTATCOM are presented in Figure 4(b). These currents are produced to suppress the harmonic components caused by nonlinear loads. As a result, their waveforms are not purely sinusoidal and exhibit differences among phases. Thanks to the proposed MAF-based *dq* control algorithm, the DSTATCOM successfully performs the intended compensation task, thereby reducing the harmonic content in the system currents.

Figure 4(c) shows the output currents (i_{sabc}) by the SEIG. The fact that these currents are smooth, balanced, and nearly sinusoidal, indicating that the disruptive effects on the load side are effectively compensated by DSTATCOM, allowing the generator to produce balanced output currents.

Waveforms of SEIG terminal voltages (v_{abc}) are given in Figure 4(d). In all three phases, the voltages are symmetrical, constant amplitude and close to sinusoidal. This shows that the voltage regulation of the system is successfully achieved. This result shows that the proposed control structure can maintain the voltage quality despite the nonlinear load effect.

The voltage and frequency behavior are evaluated in Figure 5. In Figure 5(a), the peak value of the SEIG terminal voltage V_t is presented in comparison with the reference value V_{tref}. As observed, the terminal voltage is very close to the reference value and contains only low amplitude oscillations. This shows that the voltage regulation is achieved effectively. Figure 5(b) shows the SEIG output frequency. The frequency is kept constant at approximately 50 Hz and no significant deviation is observed except for small amplitude oscillations. This shows that the proposed MAF-based *dq* control algorithm can successfully regulate the system frequency.

4.2 Performance of DSTATCOM-based SEIG under unbalanced-nonlinear load

In another scenario, the system is simultaneously subjected to the unbalanced-nonlinear load conditions. Such complex conditions are among the most challenging scenarios frequently encountered in real world applications and seriously affect the stability and power quality of power systems. While nonlinear loads cause harmonic distortion in the system, unbalanced loads cause current and voltage imbalances between phases. In this test, it is analyzed whether the proposed MAF-based *dq* control method can effectively regulate the SEIG terminal voltage and system frequency in the simultaneous presence of these two disturbances.

Figure 6(a) shows the load currents (i_{L_abc}) of the system under the unbalanced-nonlinear load conditions. The current waveforms are not only far from sinusoidal but also contain significant amplitude differences between the phases. This clearly shows that both harmonic and phase imbalance effects are present simultaneously on the load.

The phase currents (i_{fabc}) generated by DSTATCOM are given in Figure 6(b). These currents are generated to suppress load-induced harmonic and distortions and are non-sinusoidal in shape and vary between phases. This is expected because DSTATCOM tries to compensate for the disturbing currents and the output currents are generated accordingly. Thanks to the proposed MAF-based *dq* control algorithm, these compensation currents are generated in the desired form and the overall power quality of the system is improved.

Figure 6(c) shows the SEIG output currents (i_{sabc}), which are balanced, smooth and close to sinusoidal, indicating that the DSTATCOM effectively suppresses load disturbances and the generator output can be maintained without disturbances.

The behavior of the terminal voltages (v_{abc}) is given in Figure 6(d). The voltage waveforms are symmetrical,

uniform and constant amplitude in all three phases. This shows that the system can successfully maintain voltage regulation despite the unbalanced nonlinear load conditions.

The voltage and frequency behaviors are evaluated in Figure 7. In Figure 7(a), the peak value of the SEIG terminal voltage is compared with the reference value. The difference was very low, and the terminal voltage could be stabilized at the reference level. The frequency profile shown in Figure 7(b) remains constant around 50 Hz and contains only low oscillations. These results show that the proposed MAF-based *dq* control method performs well in terms of both voltage and frequency regulation.

5. Conclusions

In this study, a MAF-based *dq* control method is proposed for standalone DSATCOM-assisted SEIG systems. The proposed approach enables both voltage and frequency regulation of the SEIG. The *dq*-axis components of the load currents are processed using MAF, which effectively reduces the harmonic content. This enhances the accuracy of reference current calculation and improves the overall system response. The method is evaluated under nonlinear and unbalanced load conditions, and the results demonstrate that the system successfully achieves the desired performance.

Declaration of Ethical Standards

As the authors of this study, we declare that he complies with all ethical standards.

Credit Authorship Contribution Statement

A.S.Ozer: Software, Validation, Formal analysis, Writing -Original Draft, Visualization.
F.Sevilmis: Methodology, Software, Validation, Visualization.
H.Karaca: Investigation, Resources, Writing, Review & Editing, Supervision, Funding acquisition.

Declaration of Competing Interest

The authors declared that they have no conflict of interest.

Funding / Acknowledgements

The authors were supported within the scope of the research by the Selcuk University Scientific Research Projects Unit with Project No: 20111012.

Data Availability

No datasets were generated or analyzed during the current study.

References

Chilipi, R., Sumaiti, A. A., & Singh, B. (2020). Control of self-excited induction generator-based micro-hydro power generation system feeding single-phase and three-phase loads. In *2020 IEEE Industry Applications Society Annual Meeting*, 1–8.

Giri, A. K., Arya, S. R., Maurya, R., & Chittibabu, B. (2020). Control of VSC for enhancement of power quality in off-grid distributed power generation. *IET renewable power generation*, *14*(5), 771-778.

Golestan, S., Ramezani, M., Guerrero, J. M., Freijedo, F. D., & Monfared, M. (2014). Moving average filter based phase-locked loops: Performance analysis and design guidelines. *IEEE Transactions on Power Electronics*, 29(6), 2750–2763.

Kundu, S., Singh, M., & Giri, A. K. (2024). SPV-wind-BES-based islanded electrical supply system for remote applications with power quality enhancement. *Electrical Engineering*, 106(1), 279–294.

Ozer, A. S., Sevilmiş, F., Karaca, H., & Ahmed, H. (2024). Power quality enhancement of DSTATCOM using E²PLL-based control method for wind energy applications. In *2024 XV International Symposium on Industrial Electronics and Applications (INDEL)* (pp. 1–6). IEEE.

Ozer, A. S., Sevilmiş, F., Karaca, H., & Arabacı, H. (2022). Enhanced control method for voltage regulation of DSTATCOM based SEIG. *Energy Reports*, 8, 839–847.

Rajendran, S., Govindarajan, U., Reuben, A. B., & Srinivasan, A. (2013). Shunt reactive VAR compensator for grid-connected induction generator in wind energy conversion systems. *IET Power Electronics*, 6(9), 1872-1883.

Ram, A., Sharma, P. R., & Ahuja, R. K. (2024). Enhancement of power quality using U-SOGI based control algorithm for DSTATCOM. *Ain Shams Engineering Journal*, 15(1), 102296.

Sibrahim, M., Aissou, S., Rouas, R., Haddad, S., & Benamrouche, N. (2024). Experimental determination of minimum capacitor for self-excitation of induction generators. *International Journal of Power Electronics and Drive Systems (IJPEDS)*, 15(1), 109–116.

Shailly, D., Chittora, P., & Singh, M. (2025). Performance analysis of multiple delayed signal cancellation (MDSC) for power quality improvement for fixed speed SEIG-based distributed generation. *Electrical Engineering*, 1–20.

ELECTRICAL ENGINEERING AND ENERGY

OPEN ACCESS

A Comparative Analysis of Genetic Algorithm Replacement Strategies in a Real-World Optimization Problem: An Elitism and Diversity Oriented Perspective

Hüseyin Doğan

Department of Mechatronics Engineering, Faculty of Technology, Selcuk University, Konya, Türkiye

Submitted: 10 April 2025
Accepted: 29 April 2025
Published: 30 April 2025

Corresponding author
Hüseyin Doğan,
huseyindogan@selcuk.edu.tr

Copyright, Distributed under Creative Commons CC-BY 4.0

Abstract: In this study, generation replacement strategies used in genetic algorithms are comparatively analysed in the context of a real-world optimization problem, with a focus on the balance between elitism and diversity. The problem under consideration involves solving the equations of the Selective Harmonic Elimination (SHE) method, which is widely used for controlling Multilevel Inverters (MLIs). Six algorithms, each employing a different replacement mechanism, were tested under four distinct scenarios composed of various population sizes and iteration counts. The results were evaluated using fundamental statistical metrics, boxplots, and convergence curves. The findings reveal that elitist strategies perform better in large-population, long-duration scenarios, whereas approaches prioritizing diversity yield more effective results under limited resource conditions. This study systematically demonstrates the impact of different replacement strategies on optimization performance and offers valuable insights for strategy selection in real-world optimization problems.

Keywords Genetic Algorithm, Replacement Strategy, Elitism, Diversity, Selective Harmonic Elimination (SHE), Multilevel Inverter (MLI)

1. Introduction

Genetic Algorithm (GA) is a population-based metaheuristic optimization method inspired by evolutionary processes observed in nature. Originally introduced by John Holland (Holland, 1992), this approach aims to solve a given optimization problem through an iterative computational process based on biological mechanisms such as natural selection, genetic crossover, and mutation. One of the most critical aspects of the algorithm is the establishment of a fitness evaluation mechanism that mimics the evolutionary principle wherein individuals better adapted to environmental conditions have a higher chance of survival and gene propagation. Accordingly, a fitness (objective) function must be defined in a way that both satisfies system requirements and respects problem-specific constraints. Individuals in the population are evaluated throughout various stages of the algorithm based on the values obtained from this function.

The algorithm begins with a population composed of individuals, each representing a potential solution to the given problem, and the initial fitness scores of these individuals are calculated based on the defined objective function. Following this initial stage, the iterative process begins. At the start of each iteration, a

subset of individuals is selected based on their fitness scores. These selected individuals are then subjected to small variations through various genetic operators in order to explore potentially better solutions.

By the end of the iteration, a new generation is formed, which is expected to contain better alternatives in terms of overall solution quality. This new generation is referred to as the "offspring" while the generation at the beginning of the iteration is called the "parents". The fitness scores of the offspring are recalculated, and the individuals are reassigned as parents for the next iteration. This process continues until a satisfactory solution is reached or a predefined number of iterations is completed.

GAs have been widely applied across various fields—from engineering to economics—due to their strong global search capability and effectiveness in solving complex problems that are multimodal, nonlinear, or subject to multiple constraints. This broad range of applications is evident in numerous studies, including optimal power flow in electrical grids (Bakirtzis et al., 2002; Osman et al., 2004), parameter tuning in control systems (J. Zhang et al., 2009), feature selection in machine learning (Halim et al., 2021; Smith & Bull, 2005), scheduling and routing optimization in manufacturing systems (Gen & Cheng, 1999), financial forecasting (Kim & Han, 2000) and supply chain and inventory management (Disney et al., 2000).

The generation update phase performed at the end of each iteration ("Survivor Selection" or "Replacement") is not explicitly defined in the structure of the classical GA. More precisely, in the standard approach, no special method is applied during this phase; instead, the new generation (offspring) simply replaces the previous one (parents). However, this can result in the loss of potentially high-quality individuals from the earlier population, thereby slowing down the overall optimization process. To address this issue, various methods have been proposed in the literature in which certain individuals from the previous generation are preserved and transferred to the next generation either directly or through a specific selection process. These approaches are generally classified under the concept of "elitism" (Du et al., 2018).

Studies in the literature generally have focused on the key components of genetic algorithms—such as selection, crossover, and mutation operations—that significantly affect their performance (Alhijawi & Awajan, 2024; Ali et al., 2020; Hassanat et al., 2019; Hong et al., 2002; Katoch et al., 2021; F. Zhang et al., 2008). In contrast, generation update strategies are often treated as a fixed structural component and are rarely subjected to detailed analysis. In several existing studies, replacement methods are typically introduced as part of a newly proposed GA variant (Ahn & Ramakrishna, 2003), rather than being independently evaluated or compared with alternative approaches. In the limited number of studies that do involve comparisons, evaluations are mostly conducted using standard test functions (Brouwer et al., 2022), which often fail to reflect the dynamic and constrained nature of real-world optimization problems.

In this study, the effects of different replacement strategies used in genetic algorithms were systematically compared in the context of solving the equations of the Selective Harmonic Elimination (SHE) method, which represents a real-world optimization problem. SHE is one of the most widely used control techniques in multilevel inverters (MLIs). The primary goal of this method is to eliminate specific harmonic components in the inverter output voltage while keeping the fundamental harmonic amplitude as close as possible to a desired reference value. To achieve this, mathematical expressions are derived for the relevant harmonics, where the switching angles are defined as variables. Satisfying all objectives simultaneously requires determining the optimal set of switching angles that solve these equations concurrently (Yang et al., 2017). However, due to the nonlinear structure and trigonometric nature of the equations, solving SHE becomes increasingly challenging as the number of inverter levels rises.

Within this scope, six genetic algorithm variants were investigated; one with a standard structure and no replacement applied, and the remaining five employing different generation update mechanisms. The algorithms were tested under four different scenarios composed of various combinations of population sizes

and iteration counts, with independent runs conducted for each. The results were evaluated using key statistical metrics such as Best, Median, Worst, and Std (standard deviation), along with boxplot visualizations. Additionally, the solutions obtained were applied to the switching devices of a multilevel inverter modelled in MATLAB/Simulink, and the algorithms were further assessed based on fundamental component error and harmonic suppression performance in the output voltage.

The findings of this study reveal that while elitist strategies used during the replacement phase positively impact GA performance, they also pose a risk of reducing population diversity in scenarios with limited resources, such as low population sizes and restricted iteration counts.

In such cases, the rapid dominance of elite individuals within the population may lead to the premature elimination of individuals with relatively poor fitness but potential for long-term convergence to the global optimum. As a result, the algorithm's overall exploratory ability weakens, and the likelihood of getting trapped in local minima increases. On the other hand, diversity-oriented approaches help mitigate this risk under resource-constrained conditions and enable a more effective exploration of the solution space. These results indicate that the replacement strategy chosen should not only preserve high-quality individuals but also maintain a balanced structure that sustains diversity depending on the problem environment.

2. Switching Angle Determination via SHE in CHB-MLI Systems

In conventional two-level inverters, the output voltage is generated by switching between only two fixed levels, typically +Vdc and –Vdc. In such systems, power switches are operated at high switching frequencies to rapidly alternate the output voltage between these two levels, aiming to approximate an ideal sinusoidal waveform. While this configuration is simple and cost-effective—due to its ability to operate with a single DC source and requiring fewer semiconductor components—it also presents some significant disadvantages (Bertin et al., 2023). Since the switches must handle high voltage levels during every transition, the lifespan of components is reduced, and the overall reliability of the system is compromised. Moreover, high switching frequencies considerably increase switching losses and electromagnetic interference (EMI).

To overcome the issues observed in conventional two-level inverter structures, various MLI topologies have been developed (El-Hosainy et al., 2017). The core approach of these topologies is to generate the output voltage in a stepwise manner using multiple intermediate voltage levels, thereby producing a waveform that resembles a staircase. As a result, semiconductor devices switch lower voltage levels in each cycle, and this switching occurs only twice per half-cycle. Consequently, the need for high switching frequencies is reduced, which significantly minimizes losses, voltage stress on components, and EMI

Among MLI topologies, one of the most widely adopted structures is the Cascaded H-Bridge Multilevel Inverter (CHB-MLI) (Sunddararaj et al., 2020). In this topology, multiple H-bridge inverter modules—each with identical specifications and supplied by an independent DC source—are connected in series. Each module contributes one voltage level to the staircase-shaped output waveform (Dahidah et al., 2015). As the number of modules increases, the number of steps in the waveform also increases, resulting in an output voltage that more closely approximates a sinusoidal form. In addition to the conventional advantages offered by multilevel inverters, the CHB-MLI topology provides a significant benefit in terms of structural modularity. Thanks to this modularity, the system can be easily reconfigured by adding or removing a module when a change in output voltage level is required. Furthermore, in the event of a fault or maintenance need, the affected module can be isolated and replaced without interfering with the entire system. This reduces maintenance time, simplifies servicing, and enhances overall system reliability.

In the CHB-MLI topology, the output voltage waveform is defined by the switching angles that determine when each module contributes to the output. Since each module generates one voltage level in the staircase waveform, the number of switching angles corresponds to the number of modules used. Therefore, a system

with n modules requires n switching angles ($\theta_1, \theta_2, \ldots, \theta_n$). To accurately compute these angles, n independent equations are needed. method provides a systematic approach for determining these angles (Lingom et al., 2024). Among the resulting n equations, one is formulated to match the fundamental component of the output voltage to the desired reference value, while the remaining $n-1$ equations are each constructed to eliminate a specific harmonic component. As a result, harmonic control in the SHE method emerges both as a direct objective and as a natural outcome of the switching angle calculation process

In this study, the CHB-MLI configuration under consideration is a single-phase, 11-level inverter. Accordingly, five ($n = 5$) H-bridge inverter modules are employed, each supplied by a DC voltage source of 50 V. The output voltage waveform presented in Figure 1 illustrates the stepwise structure formed by the contribution of each module. Here, V_x ($x = 1,2,3,4,5$) represents the output voltage of the corresponding module. Each module is activated at its respective switching angle θ_x adding its voltage to the existing total and thereby increasing the output voltage to the next level. This process continues sequentially during each quarter-cycle, resulting in the desired multilevel voltage profile.

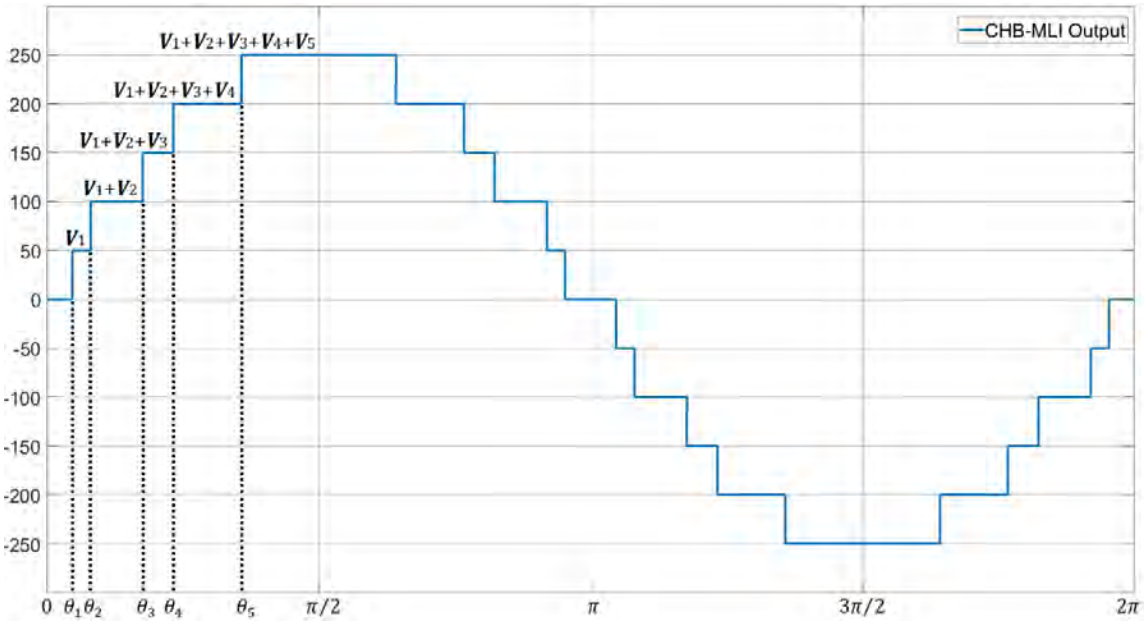

Figure 1 The Output Voltage Waveform for a Single-Phase CHB-MLI

Under the assumption of half-wave symmetry, even-order harmonic components are inherently eliminated from the output voltage waveform as shown in the figure. Furthermore, assuming that all DC sources are equal, a general expression can be defined for each odd harmonic component present in the output voltage. In this equation, h and V_h represent the order of the odd harmonics in the output voltage ($h = 1,3,5 \ldots$) and the amplitude of the hth harmonic component, respectively. θ_i denotes the ith switching angle ($i = 1,2,3,4,5$).

$$V_h = \frac{4V_{DC}}{h\pi} \sum_{i=1}^{5} \cos(h\theta_i) \tag{1}$$

Within the scope of the SHE method, an algebraic system of equations is derived from the general expression above to regulate the desired fundamental component level in the output voltage while suppressing undesired harmonics. These equations represent the amplitudes of the harmonic components expressed as functions of the switching angles. Among them, one corresponds to the fundamental component ($h = 1$), while the remaining four represent the amplitudes of the targeted harmonics to be eliminated ($h = 3,5,7,9$).

The primary objective of the optimization algorithms examined in this study is to numerically solve this system of equations to determine valid switching angles that satisfy the defined criteria.

3. Generation Update Strategies in Genetic Algorithms

In genetic algorithms, generation replacement (also referred to as survivor selection) is a critical phase that determines how the newly generated population at the end of an iteration is transferred to the next generation. This process plays a direct and essential role in preserving genetic diversity, preventing premature convergence, and improving overall solution quality. Replacement strategies are based on different rules regarding how the parent and offspring populations are compared, which individuals are preserved, and which are eliminated.

In this study, several alternative replacement strategies to the classical approach were evaluated, and their effects on the SHE problem were comparatively analyzed. Within this scope, a standard real-coded GA framework was employed across all variants to ensure consistency. Each individual X_i in the population of size N was defined as a solution vector composed of five switching angles θ_j $(j = 1,2,\dots,5)$, as expressed in Equation 2. These angles must satisfy the constraint provided in Equation 3. In all algorithms, the selection process was carried out using the roulette wheel method, single-point crossover was applied during the crossover phase, and a basic mutation strategy was used.

$$X_i = (\theta_1, \theta_2, \theta_3, \theta_4, \theta_5) \;\; i \in \{1,2,\dots,N\} \tag{2}$$

$$0 \le \theta_1 < \theta_2 < \theta_3 < \theta_4 < \theta_5 \le \pi/2 \tag{3}$$

In the algorithms under investigation, the fitness function derived from the SHE equations was defined in Equation 4 to evaluate the individuals in the population (Bektaş et al., 2023). This function is formulated based on a two-component error structure. The first term, $f_1(X_i)$, represents the difference between the obtained fundamental component amplitude and the desired reference value (V_{1ref}). The second term $f_2(X_i)$, evaluates the suppression level of undesired harmonic components corresponding to the 3rd, 5th, 7th and 9th harmonic orders. During this evaluation, weighting coefficients ($w = 2.5, 2, 1.5, 1$) were applied to assign greater importance to lower-order harmonics, making them a higher priority in the optimization process. As a result, minimizing the fitness value leads to a solution where the fundamental component closely matches the target value while the unwanted harmonics are effectively suppressed.

$$f(X_i) = \left(f_1(X_i) + f_2(X_i)\right) \tag{4}$$

$$f_1(X_i) = \left| V_{1ref} - \frac{4V_{DC}}{\pi} \sum_{j=1}^{5} \cos\left(X_{i,j}\right) \right| \tag{5}$$

$$f_2(X_i) = \left(\frac{4V_{DC}}{\pi}\right)^2 \sum_{k=1}^{4} w_k \left(\frac{1}{h_k} \sum_{j=1}^{5} \cos\left(h_k X_{i,j}\right) \right)^2 \tag{6}$$

$$h = 3,5,7,9 \;\; w = 2.5, 2, 1.5, 1$$

The first algorithm included in the comparison, GA01, is the standard genetic algorithm without any replacement strategy applied. In this structure, the offspring individuals ($X_{off}(t)$) generated through selection, crossover, and mutation in each iteration are directly assigned as the parents of the next iteration ($X_{par}(t+1)$), as shown in Equation 7, while the current iteration's parents ($X_{par}(t)$) are discarded. As a result, the population is completely replaced in every generation. This technique is commonly referred to in the evolutionary algorithms literature as the (μ, λ) selection strategy.

$$X^{par}(t+1) = X^{off}(t), F^{par}(t+1) = F^{off}(t) \tag{7}$$

The second algorithm compared (GA02) corresponds to the structure commonly known in the literature as the elitist GA. In this method, at the beginning of each iteration, the n best-performing individuals based on fitness are selected and stored as elite individuals X^e (Equation 8). At the end of the iteration, the n worst-performing individuals X^w among the offspring are identified (Equation 9) and directly replaced with the previously saved elites (Equation 10). After this replacement, the updated offspring population—including the elites—is used as the parent population for the next iteration, as in the standard GA. In this approach, the elite individuals are transferred to the next generation without being subjected to any additional comparison or selection mechanism.

$$X^e(t) = \{X_1^e, X_2^e, \dots, X_n^e\}$$
$$f_1^e \leq f_2^e \dots \leq f_n^e \tag{8}$$

$$X^w(t) = \{X_1^w, X_2^w, \dots, X_n^w\}$$
$$f_1^w \geq f_2^w \dots \geq f_n^w \tag{9}$$

$$X_k^w \leftarrow X_k^e \quad k = 1,2,\dots,n \tag{10}$$

The third algorithm (GA03) is based on a tournament-based replacement strategy with random pairing. In this method, at the end of each iteration, a tournament is conducted between the parent population and the newly generated offspring population. For this purpose, as defined in Equation 10, an index array is created by randomly selecting non-repeating integers from the range $[1, N]$ to represent the offspring individuals. Then, each parent individual $X_i^{par}(t)$ is paired and compared with the corresponding offspring individual $X_k^{off}(t)$ from the index array, as shown in Equation 11. The individual with the better fitness value is selected for transfer to the next generation.

$$p = randperm(N) \tag{11}$$

$$X_i^{par}(t+1) = \begin{cases} X_i^{par}(t), & f_i^{par}(t) < f_k^{off}(t) \\ X_k^{off}(t), & f_k^{off}(t) > f_i^{par}(t) \end{cases} \qquad i = 1,2,\dots,N \ (k = p_i) \tag{12}$$

The fourth algorithm (GA04) adopts a roulette wheel-based replacement strategy. In this structure, the current parent population $X^{par}(t)$ and the newly generated offspring population $X^{off}(t)$ are combined into a unified pool $X^{com}(t)$ consisting of $2N$ individuals (Equation 13). For each individual in this pool, selection probabilities p_i are calculated by taking the inverse of their fitness values and normalizing them, followed by computation of cumulative selection probabilities pk_i (Equation 14). Using these cumulative probabilities, individuals corresponding to randomly generated numbers in the range $[0,1]$ are selected, and a new parent population $X_i^{par}(t+1)$ consisting of N individuals is formed (Equation 15)

$$X^{com}(t) = \left(X^{par}(t) \cup X^{off}(t)\right) \tag{13}$$

$$p_i = \frac{1/f_i^{com}}{p_{sum}} \quad p_{sum} = \sum_{i=1}^{2N} 1/f_i^{com} \qquad i = 1,2,\dots,2N$$
$$pk_i = \sum_{x=1}^{i} p_x \tag{14}$$

$$X_i^{par}(t+1) = \begin{cases} X_1^{com} & 0 < rand \le pk_1 \\ X_2^{com} & pk_1 < rand \le pk_2 \\ \vdots & \vdots \\ X_{2N}^{com} & pk_{2N-1} < rand \le 1 \end{cases} \quad i = 1,2,\dots,N \tag{15}$$

The fifth algorithm (GA05) is based on a ranking-based elitist replacement strategy. In this method, as shown in Equation 13, the parent population and the newly generated offspring population are merged into a common pool. The individuals in this pool are then ranked according to their fitness values (Equation 16), and the best N individuals are directly selected to form the next generation population $X_i^{par}(t+1)$ (Equation 17). This strategy does not involve any comparison, probability, or selection mechanism; instead, it relies solely on absolute fitness ranking. This approach corresponds to the $(\mu + \lambda)$ selection strategy commonly used in evolutionary algorithms.

$$f_1^{com} \le f_2^{com} \dots \le f_{2N}^{com} \tag{16}$$

$$X_i^{par}(t+1) = X_i^{com}(t) \quad f_i^{par}(t+1) = f_i^{com}(t) \qquad i = 1,2,\dots,N \tag{17}$$

The sixth and final algorithm (GA06) implements a partial elitism-based replacement strategy that aims to preserve the best-performing individuals from both the parent and offspring populations while also giving a chance to lower-performing individuals from both generations. In this method, the current parent and offspring populations are first ranked separately according to their fitness values (Equation 18). From each population, q individuals ($q = N/4$) in the top quartile are selected to form the subsets $X^1(t)$ and $X^2(t)$, respectively (Equation 19). Additionally, q individuals are randomly selected from the remaining lower-performing individuals in each population (from the range $[q+1, N]$), forming subsets $X^3(t)$ and $X^4(t)$ (Equation 20). Finally, the union of these four subsets constitutes a combined population $X^{com}(t)$ of N individuals, which is assigned as the parent population $X^{par}(t+1)$ for the next generation (Equation 21). This approach can be considered a hybrid structure that simultaneously promotes elitism and diversity and may be viewed as a variation of the previous replacement strategy.

$$f_1^{par} \le f_2^{par} \dots \le f_N^{par}, f_1^{off} \le f_2^{off} \dots \le f_N^{off} \tag{18}$$

$$X_i^1(t) = X_i^{par}(t), X_i^2(t) = X_i^{off}(t) \qquad i = 1,2,\dots,q \quad (q = N/4) \tag{19}$$

$$\begin{aligned} X_i^3(t) &= \{X_{r1}^{par}, X_{r2}^{par}, \dots, X_{rq}^{par}\} & rx &\in \{q+1, q+2, \dots, N\} \\ X_i^4(t) &= \{X_{r1}^{off}, X_{r2}^{off}, \dots, X_{rq}^{off}\} & x &= 1,2,\dots,q \end{aligned} \tag{20}$$

$$X^{com}(t) = \left(X^1(t) \cup X^2(t) \cup X^3(t) \cup X^4(t)\right) \rightarrow X^{par}(t+1) = X^{com}(t) \tag{21}$$

Generation replacement strategies are designed to prevent the loss of high-quality solutions. While the preservation of good individuals is commonly referred to as elitism in the literature, this approach also introduces the risk of gradually losing population diversity; one of the fundamental driving forces of evolutionary algorithms. Therefore, the balance between elitism and diversity plays a critical role in optimization problems. In this context, the algorithms examined in this study are evaluated with respect to their approaches to elitism and diversity as follows:

- GA01, which does not incorporate any elitism mechanism, completely eliminates parent individuals after each iteration, regardless of their quality. Diversity is maintained solely through the effect of the variation operators applied to the offspring population.
- The only difference between GA02 and the previous algorithm is the preservation of a small elite portion (5%) of the parent population. This limited intervention introduces a mild level of elitism

into the optimization process. However, since elite individuals are carried over to the next generation without any comparison or competition, this may result in the elimination of potentially superior offspring in the later stages of long-term iterations, where differences among individuals diminish. Apart from this, diversity is maintained (as in GA01) only through the offspring, with no contribution from the previous generation.

- The tournament structure in GA03 ensures that individuals with better (i.e., lower) fitness values are largely preserved in the population, indicating a strong elitist characteristic. However, because pairings are made randomly, there is always a possibility that two weak individuals may compete against each other. This helps prevent diversity from being completely lost and allows the partial retention of individuals who, despite low current performance, may hold potential in the evolutionary process.

- GA04, which uses a roulette wheel-based selection, combines the parent and offspring populations into a shared pool, where individuals with better fitness values have a much higher probability of being selected for the next generation. Moreover, due to the stochastic nature of this approach, top-performing individuals may be selected multiple times, increasing the risk of population dominance by a few elites. Although the probability of selecting low-performing individuals is not zero, it remains very low. Thus, compared to the tournament method, GA04 supports diversity to a lesser extent while applying elitism in a stricter and less controlled manner.

- The principle of GA05 is purely deterministic, with no probabilistic components involved. After merging the parent and offspring populations, the top N individuals are directly selected to form the next generation. The selection of the best individuals is guaranteed with 100% certainty, making GA05 more stable and reliable in terms of elitism compared to probabilistic approaches like roulette or tournament selection. However, because the selection is based on absolute ranking, even the best individual is chosen only once. This ensures that elitism is implemented effectively yet in a balanced way. As a result, while elite individuals are preserved, moderately fit individuals also have a chance to remain in the system helping to sustain diversity. That said, this strategy is intolerant toward weaker individuals: those with the worst fitness values are categorically excluded from the next generation.

- GA06 aims to consciously balance elitism and diversity. As in GA05, the transfer of elite individuals is guaranteed, making the elitist aspect of this approach deterministic. However, unlike GA05, the elite individuals are selected separately from both the parent and offspring populations, and their total proportion is lower. Moreover, diversity is not left to the natural course of the evolutionary process; instead, it is actively promoted by applying positive selection bias in favour of weak individuals. While this guarantees the preservation of diversity, it also deliberately restricts the spread of elite solutions. Consequently, in long-term iterations, the suppressing effect on elite individuals may pose a risk of stagnation in solution quality.

4. Results and Discussions

In this study, the performance of six different GA variants employing distinct replacement strategies was compared in the context of solving the SHE equations. For this purpose, each algorithm was tested under four different scenarios. These scenarios were structured based on combinations of population size (N) and number of iterations (T), as outlined below:

(i) $N = 20,\ T = 20$; (ii) $N = 20,\ T = 100$; (iii) $N = 100,\ T = 20$; (iv) $N = 100,\ T = 100$.

The primary objective of designing this scenario structure is to evaluate how the algorithms perform under

both resource-constrained conditions (low N and T) and conditions that allow for broader search capabilities (high N and T).

For each algorithm, 501 independent runs were performed in each scenario. In these runs, the objective function defined in Equation 4 was used to evaluate the quality of the solutions. The reference fundamental component amplitude (V_{1ref}) was set to 250 V. In each run, the best (i.e., lowest) fitness value achieved by the algorithm was recorded. From the resulting set of 501 values, the performance metrics Best, Median, Worst, and Std (standard deviation) were computed and comparatively presented in the relevant tables (Tables 1-4)). To compare the distributions of these values, boxplots (Figures 2, 4, 6, 8) were included, and convergence curves (Figures 3, 5, 7, 9) were used to analyse the average progress trends of the algorithms throughout the iterations.

The results for the first scenario are presented in Table 1 and Figures 2 and 3. This scenario represents a resource-constrained setting in which both the population size and the number of iterations are kept low. The limited number of iterations prevents the algorithms from fully demonstrating their optimization capabilities. Therefore, the ability to perform a fast and effective exploration of the search space becomes critically important. In this context, the small population size places the entire burden of exploration on the algorithm's capacity to maintain diversity.

Table 1 Optimization results for N=20 and T=20

Algorithms	Statistical Summary of Fitness Values			
	Best	**Median**	**Worst**	**Std**
GA01	12.2832	85.3245	269.2885	47.5573
GA02	6.9794	53.5927	248.0116	44.6122
GA03	5.8093	59.8713	250.0669	59.3952
GA04	6.5139	75.7216	266.1919	57.9014
GA05	5.5482	88.4709	268.7646	61.6239
GA06	7.6176	48.1857	178.0961	28.7910

According to the results, GA06, which enforces diversity structurally by design, stands out as the most successful algorithm in terms of both performance metrics and boxplot appearance. It is followed by GA02, which allows diversity to emerge naturally while applying a moderate and controlled level of elitism. Although the Median values of these two algorithms are close, GA06 exhibits a significantly lower Std value, indicating more consistent and stable outcomes.

GA03, which partially allows weaker individuals to survive through tournament selection, ranks just behind these two. GA04, while not as tolerant to diversity as GA03, still offers more flexibility than GA05, placing it next in line. GA05, where elitism is dominant and diversity is nearly disregarded, performs similarly to the standard GA01, and in some cases even worse. Notably, the convergence curves in Figure 3b clearly show that the final performance ranking of the algorithms aligns precisely with the extent to which each strategy supports diversity.

The results for the second scenario are presented in Table 2 and Figures 4 and 5. This scenario represents a longer evolutionary process combined with a small population size. This combination is particularly valuable for observing the algorithms' abilities to maintain diversity and their long-term convergence behaviour.

Table 2 Optimization results for N=20 and T=100

Algorithms	Statistical Summary of Fitness Values			
	Best	**Median**	**Worst**	**Std**
GA01	6.5454	35.2412	99.8045	19.7326
GA02	4.6600	15.2062	54.7889	13.4916
GA03	4.5360	14.8900	115.6199	18.8921
GA04	5.6908	30.5692	104.0617	18.7601
GA05	4.5427	10.1239	111.7354	21.6504
GA06	5.0021	16.4486	70.5006	13.8457

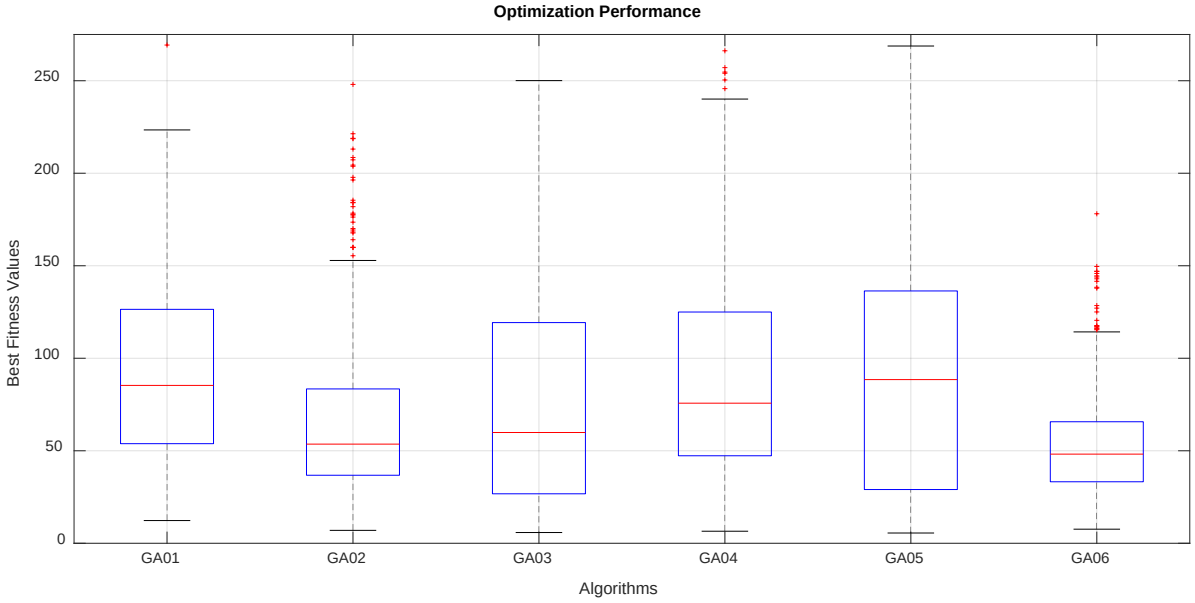

Figure 2 Boxplot graphic of the algorithms for N=20, T=20

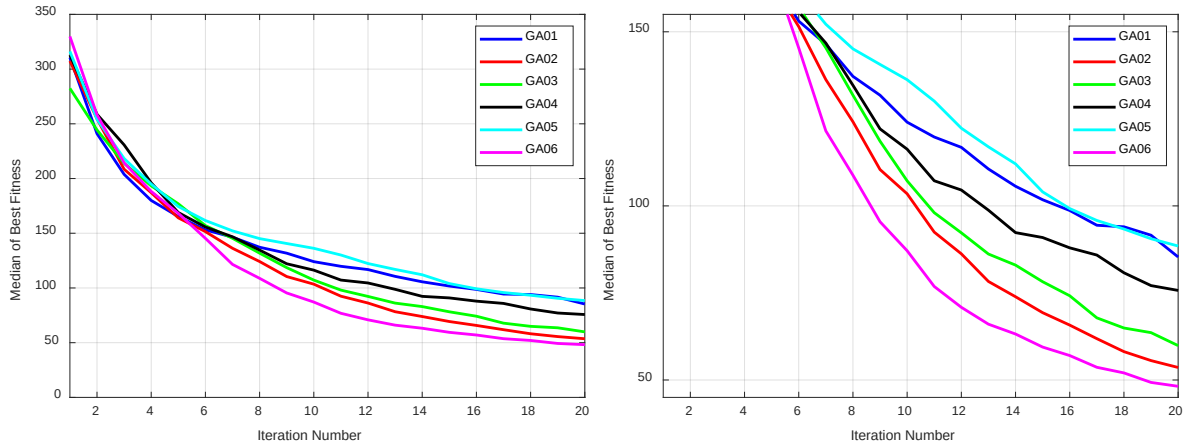

(a) **(b)**

Figure 3 Convergence curves of the algorithms for N=20, T=20; **(a)** normal, **(b)** magnified view

The results indicate that, compared to the first scenario, all algorithms achieved lower fitness values and the performance differences between them became more pronounced. Analysing the boxplots and statistical metrics, it is evident that the increased number of iterations—despite a fixed population size—enabled GA05 to reveal its potential. GA05, which attained the lowest Median value by a significant margin, is followed by GA03, GA02, and GA06, respectively. However, the differences in Median values among these three algorithms are statistically negligible.

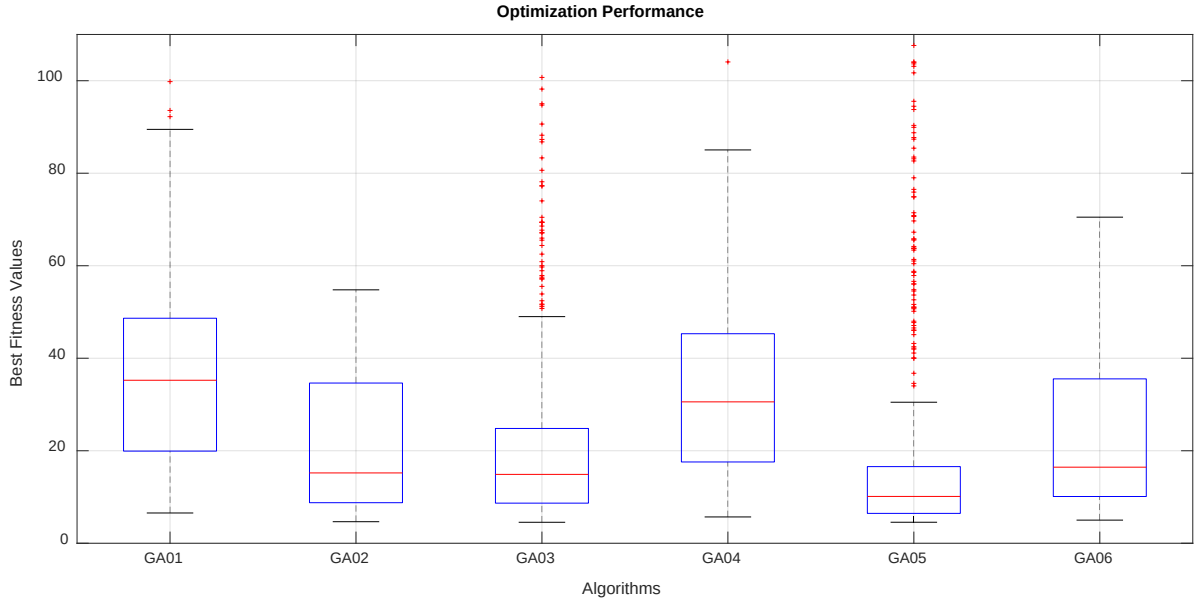

Figure 4 Boxplot graphic of the algorithms for N=20, T=100

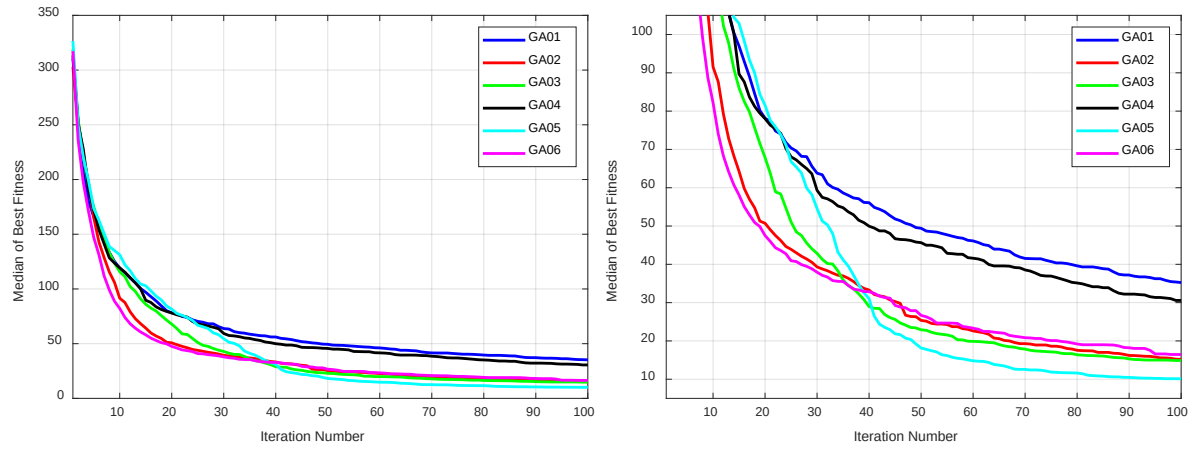

(a) **(b)**

Figure 5 Convergence curves of the algorithms for N=20, T=100; **(a)** normal, **(b)** magnified view

The superiority previously achieved by GA06 and GA02 due to their diversity-oriented designs appears to have relatively diminished in this scenario, while algorithms with stronger elitist structures have begun to take the lead. Nonetheless, the balanced distribution in the boxplots and the low Std values of these two algorithms indicate that the positive influence of diversity is still present.

On the other hand, although GA03 and GA05 performed well overall, their results include a substantial

number of outliers, which contributes to their relatively high standard deviation values. This suggests that under the current population size, elitist strategies have not yet achieved full effectiveness in eliminating low-quality individuals.

GA04, meanwhile, lagged behind these algorithms and exhibited a performance comparable to that of GA01.

The convergence curves clearly reveal the optimization superiority of GA05 and the improved performance of GA03 compared to the previous scenario. Although GA06 and GA02 initially take the lead thanks to the advantages of diversity, they are eventually overtaken—first by GA03, and then by GA05. In the final phase of the iteration process, GA05 opens a significant gap, while the remaining algorithms conclude the process at relatively similar performance levels.

The results for the third scenario are presented in Table 3 and Figures 6 and 7. This scenario is defined by a large population size combined with a limited number of iterations. Such a combination naturally provides diversity to the algorithms but does not offer sufficient time to enhance solution quality. In this context, unlike previous scenarios, population-induced diversity ceases to be an advantage, and elitist strategies capable of acting quickly in the early stages come to the forefront.

This shift is most dramatically reflected in the performance of GA06. Although GA06 previously stood out due to its structural support for diversity, it fails to maintain that advantage under this scenario. On the contrary, the continued application of positive discrimination toward weak individuals and the limited selection of strong ones in a large population setting effectively turns its former advantage into a disadvantage. The decline in performance that began in the second scenario continues here as well, with GA06 falling even behind GA02.

On the other hand, GA05 and GA03, which had previously appeared relatively disadvantaged due to short evolutionary durations, are now able to realize their potential thanks to the increased population size. GA05 once again achieves the lowest Median value, as it did in the second scenario. The fact that this value is nearly identical to that of the previous scenario suggests that for GA05, there is little difference between having a large population versus a high iteration count.

GA03 follows closely behind GA05, and the performance gap between them appears to have narrowed considerably compared to the previous scenario. This indicates that GA03 benefits slightly more from large population settings.

The convergence curves preserve the overall structure observed earlier. However, a notable observation is that GA03 remains neck-and-neck with GA05 until almost the end of the process. In the final few iterations, GA05 gains a slight edge and finishes ahead.

The results for the fourth and final scenario are presented in Table 4 and Figures 8 and 9. This scenario, characterized by both a large population size and a high number of iterations, represents the most ideal evolutionary conditions. This combination enables the algorithms to explore a wide solution space while also applying effective exploitation through the selection of high-quality individuals over an extended period.

Therefore, under this scenario, the overall evolutionary performance of the algorithms is revealed in the clearest and most balanced manner.

The results clearly demonstrate the impact of this ideal setting. GA05 once again emerged as the most successful algorithm, achieving the lowest Median value across all scenarios. This is further supported by its boxplot, which exhibits a narrow structure with very few outliers, indicating that the algorithm produced results that were not only good but also highly consistent. Additionally, GA05 achieved the lowest Std value by a significant margin. This confirms that the elitist strategy yields maximum efficiency when combined with a large population and an extended evolutionary process.

Table 3 Optimization results for N=100 and T=20

Algorithms	Statistical Summary of Fitness Values			
	Best	**Median**	**Worst**	**Std**
GA01	5.7042	32.9837	97.1225	16.6028
GA02	4.9312	17.9718	61.2656	12.8229
GA03	4.5388	12.9656	81.0595	14.1293
GA04	4.8124	21.8115	70.5730	15.7836
GA05	4.4754	10.3718	107.9555	19.2538
GA06	5.7045	20.8530	72.1362	13.5063

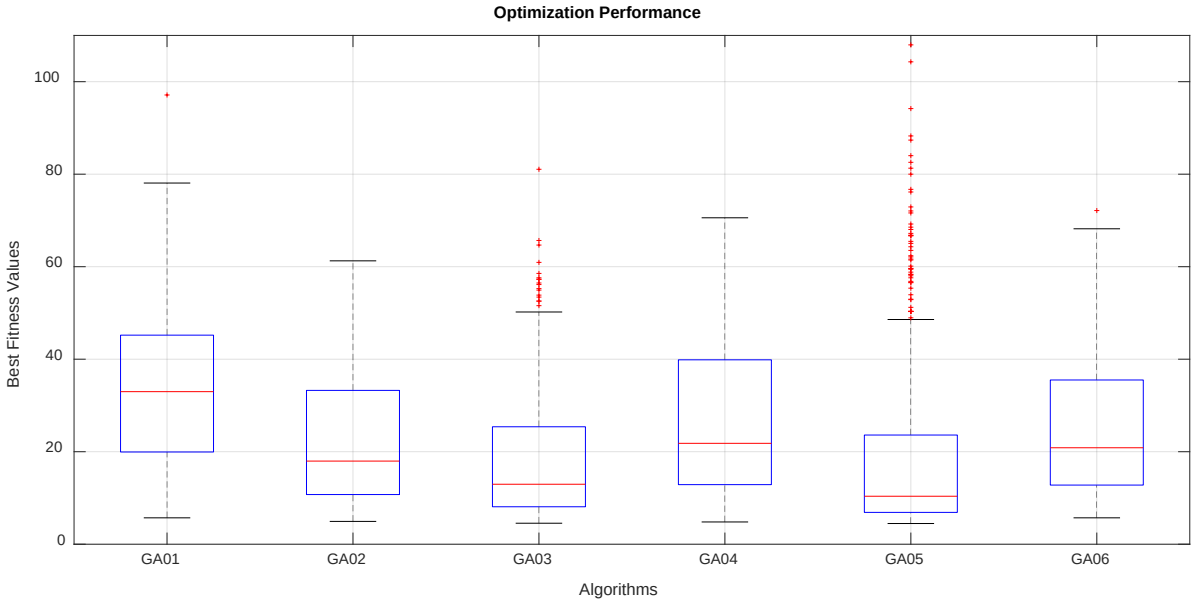

Figure 6 Boxplot graphic of the algorithms for N=100, T=20

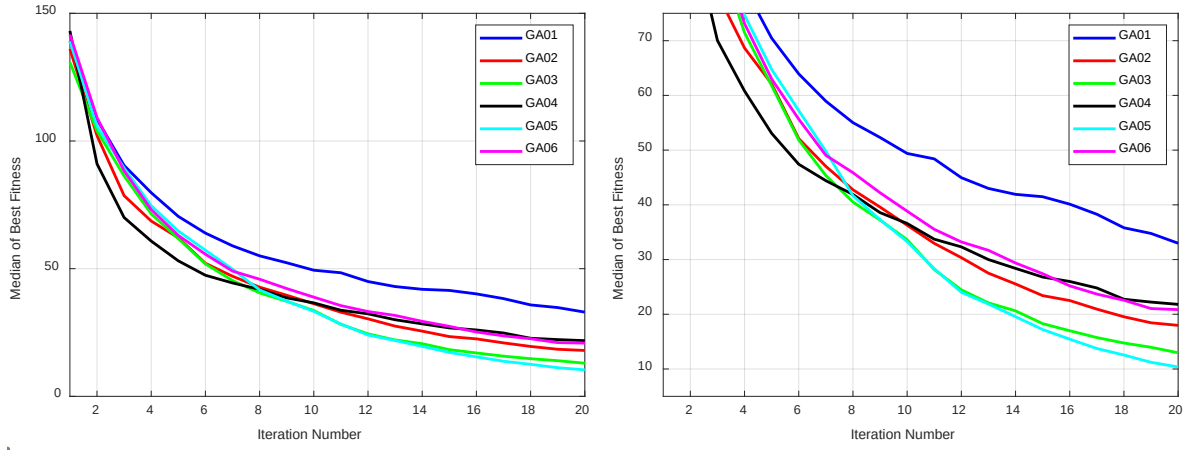

(a) **(b)**

Figure 7 Convergence curves of the algorithms for N=100, T=20; **(a)** normal, **(b)** magnified view

Table 4 Optimization results for N=100 and T=100

Algorithms	Statistical Summary of Fitness Values			
	Best	**Median**	**Worst**	**Std**
GA01	4.6144	10.6678	44.5221	11.3218
GA02	4.3664	5.1320	41.8507	11.5785
GA03	4.3605	5.1953	44.0698	8.9830
GA04	4.4891	8.6848	42.8013	11.4411
GA05	4.3387	4.7604	13.9133	1.2981
GA06	4.5438	7.5069	44.6007	12.4250

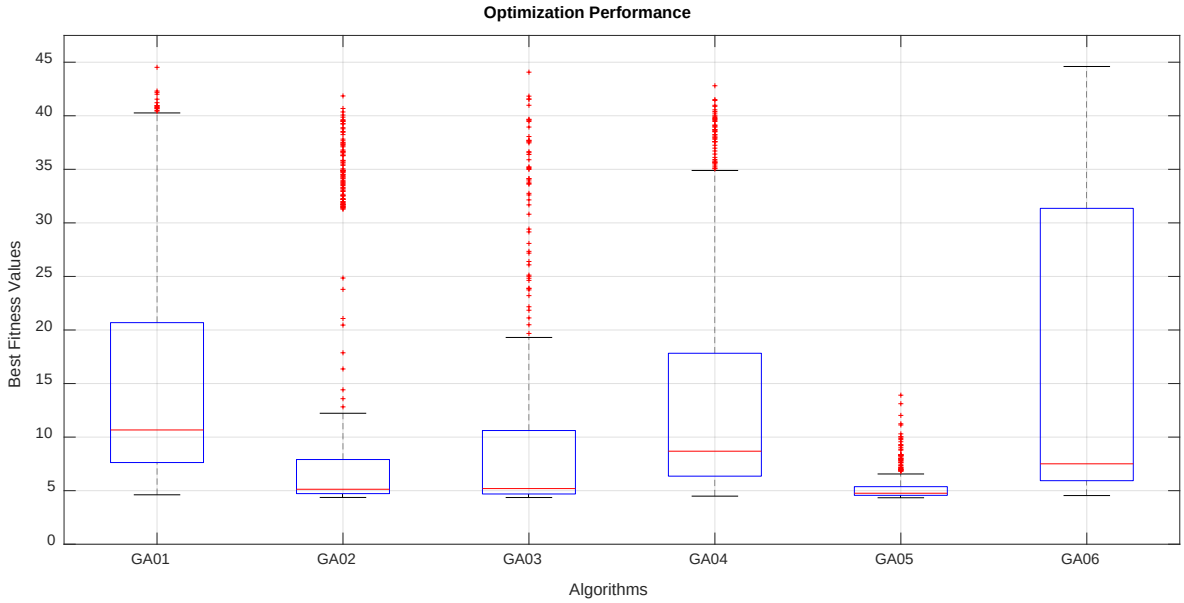

Figure 8 Boxplot graphic of the algorithms for N=100, T=100

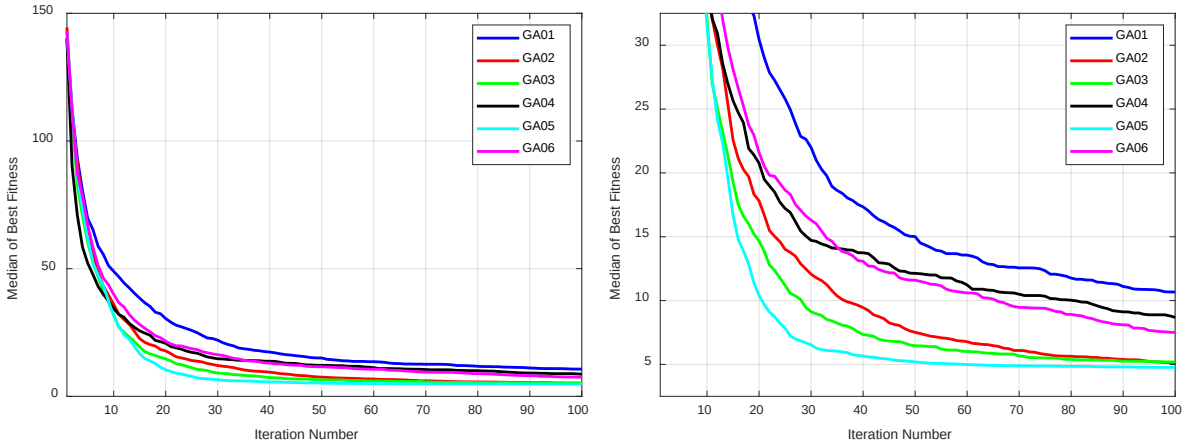

(a) **(b)**

Figure 9 Convergence curves of the algorithms for N=100, T=100; **(a)** normal, **(b)** magnified view

GA02 managed to maintain its competitiveness over the long run, owing to its initial diversity advantage and balanced level of elitism. The performance of GA03 in this scenario also aligns well with previous trends. In terms of the Median metric, there is virtually no difference between GA02 and GA03, and the gap between either of them and GA05 remains relatively small.

However, the main distinction becomes apparent in the standard deviation (Std) values. The Std values of GA02 and GA03 are notably higher than that of GA05. Between the two, GA03 appears to have produced slightly more consistent results. Although the boxplot of GA02 may initially suggest a narrower spread, its high Std value and the concentration of outliers above the box indicate greater variability in its results.

As for GA06, the performance decline observed in previous scenarios continued. Even under this high-population condition, its structure—designed to protect weak individuals—caused it to lag behind. GA04 also underperformed, once again falling short of expectations and ranking among the worst-performing algorithms along with GA01.

The convergence curves clearly reflect the overall trend. GA05, GA03, and GA02 distinctly separate themselves from the other algorithms throughout the process. Starting from the early iterations, GA05 demonstrated the fastest decline in fitness, reaching low values in a short time. However, midway through the process, the rate of decline slowed, and it transitioned into a more stable convergence pattern. Meanwhile, GA03 and GA02, though initially declining more gradually than GA05, consistently improved in later iterations, and by the end, all three algorithms converged to similarly high-quality solutions.

To evaluate the optimization results at the waveform level, the switching angles corresponding to the Median metric for each algorithm and scenario were applied to a CHB-MLI model developed in MATLAB/Simulink. The output voltage waveforms were analyzed by extracting their harmonic spectra, which included the amplitudes of the fundamental component and harmonics up to the 10th order, along with THD levels. The corresponding simulation results are presented in Tables 5–8 and Figures 10–13.

As observed in the results, the THD levels and fundamental component errors are generally consistent with the previously reported fitness values, since these targets were explicitly incorporated into the fitness function. These additional simulation findings visually confirm the quality of the obtained solutions and provide further insights into the waveform-level behavior of the algorithms.

As expected, in the first scenario—characterized by limited population size and low iteration count—the overall performance of the algorithms remained constrained, with none of them achieving a THD value below 1%. Moreover, in some algorithms, a trade-off between the two optimization targets was observed; while THD was reduced, the voltage error increased, or vice versa. Nevertheless, GA02 and GA06, which prioritize diversity, outperformed the others under these constraints by achieving lower THD and voltage error levels, highlighting the advantage of diversity-oriented structures in resource-constrained environments.

In contrast, the fourth scenario, with its large population size and extended evolutionary duration, led to improved overall performance across all algorithms. All achieved THD values below 1%, and the highest voltage error remained within 1.6%. Despite this general improvement, GA02, GA03, and GA05—each employing strong and controlled elitist strategies—distinctly outperformed the remaining algorithms in terms of both harmonic suppression and fundamental component accuracy

Table 5 Optimal switching angles and simulation results for Median metric (N=20,T=20)

Algorithms	Fitness	Optimal Switching Angles (θ)					% THD	% Error
	Scores	θ_1	θ_2	θ_3	θ_4	θ_5	Until 10th	V_1 Voltage
GA01	85.3245	7.9465	18.3534	29.7735	45.8827	65.4568	2.93	-0.32
GA02	53.5927	1.5109	23.3400	36.4685	60.9955	89.8899	1.03	-18.36
GA03	59.8713	11.6788	15.9557	35.1780	53.7048	83.7996	1.90	-12.04
GA04	75.7216	10.0911	15.0053	34.0250	51.6044	83.9939	2.33	-10.84
GA05	88.4709	3.1617	18.7100	29.9396	41.0352	67.7889	3.11	0.36
GA06	48.1857	4.9903	20.2231	33.9298	53.5520	85.7324	1.52	-12.68

Table 6 Optimal switching angles and simulation results for Median metric (N=20,T=100)

Algorithms	Fitness	Optimal Switching Angles (θ)					% THD	% Error
	Scores	θ_1	θ_2	θ_3	θ_4	θ_5	Until 10th	V_1 Voltage
GA01	35.2412	1.4836	20.7879	27.1360	45.4366	65.2832	1.91	0.36
GA02	15.2062	8.7132	13.4753	32.6415	41.8628	65.4789	1.26	0.8
GA03	14.8900	1.2217	20.2579	28.1440	42.7254	64.3385	1.10	1.44
GA04	30.5692	9.4952	13.0744	36.6930	37.5135	64.5422	1.92	1.4
GA05	10.1239	3.0639	18.1193	29.3707	43.7832	64.5049	0.77	1.08
GA06	16.4486	3.9476	17.5527	30.5590	41.3452	65.1237	1.20	1.36

Table 7 Optimal switching angles and simulation results for Median metric (N=100,T=20)

Algorithms	Fitness	Optimal Switching Angles (θ)					% THD	% Error
	Scores	θ_1	θ_2	θ_3	θ_4	θ_5	Until 10th	V_1 Voltage
GA01	32.9837	0.6173	19.2967	29.2596	45.5644	65.6026	1.56	-0.04
GA02	17.9718	9.2698	14.1192	32.0693	43.3065	66.3290	1.21	0.08
GA03	12.9656	4.1939	17.6740	28.6875	42.8704	63.5129	0.97	1.92
GA04	21.8115	5.6635	16.4219	31.2042	41.7955	61.7783	1.16	2.48
GA05	10.3718	10.0673	13.3050	31.9323	42.9492	65.3629	0.80	0.6
GA06	20.8530	3.0644	17.1574	29.8408	40.7698	61.9660	0.94	3

Table 8 Optimal switching angles and simulation results for Median metric (N=100,T=100)

Algorithms	Fitness	Optimal Switching Angles (θ)					% THD	% Error
	Scores	θ_1	θ_2	θ_3	θ_4	θ_5	Until 10th	V_1 Voltage
GA01	10.6678	0.0314	19.4255	28.5023	42.4662	64.3338	0.81	1.56
GA02	5.1320	0.3848	18.9488	29.4598	42.7833	63.6613	0.23	1.6
GA03	5.1953	0.0580	19.0705	29.0255	43.0818	63.8637	0.33	1.52
GA04	8.6848	2.0110	18.2852	29.1365	42.6399	62.6593	0.59	2.2
GA05	4.7604	4.1916	17.6921	30.1474	42.6098	63.9630	0.23	1.48
GA06	7.5069	4.7167	17.2323	30.8623	42.8791	64.6001	0.61	1.04

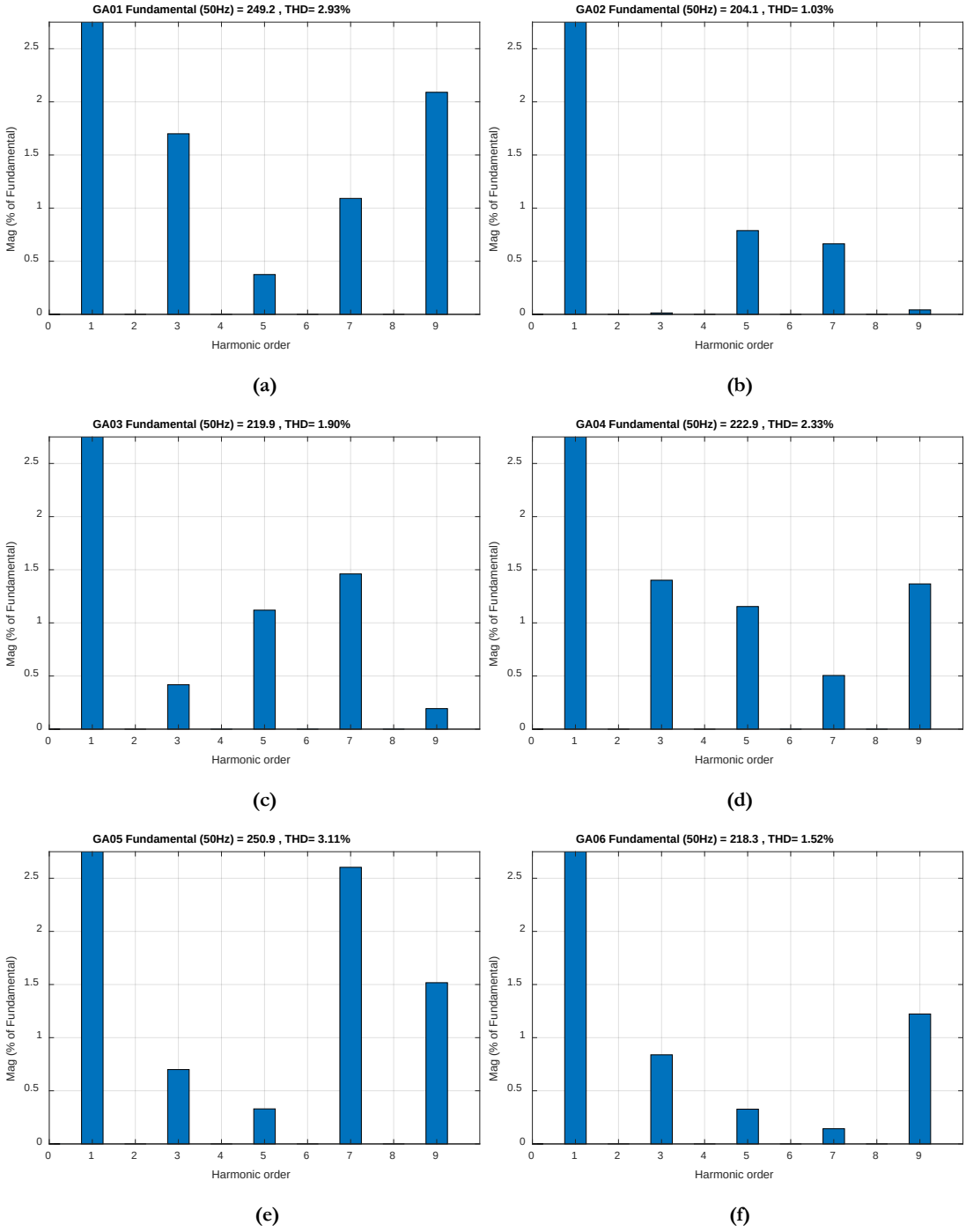

Figure 10 Frequency spectrum and fundamental harmonic values of algorithms at N=20, T=20

(a) GA01; **(b)** GA02; **(c)** GA03; **(d)** GA04; **(e)** GA05; **(f)** GA06

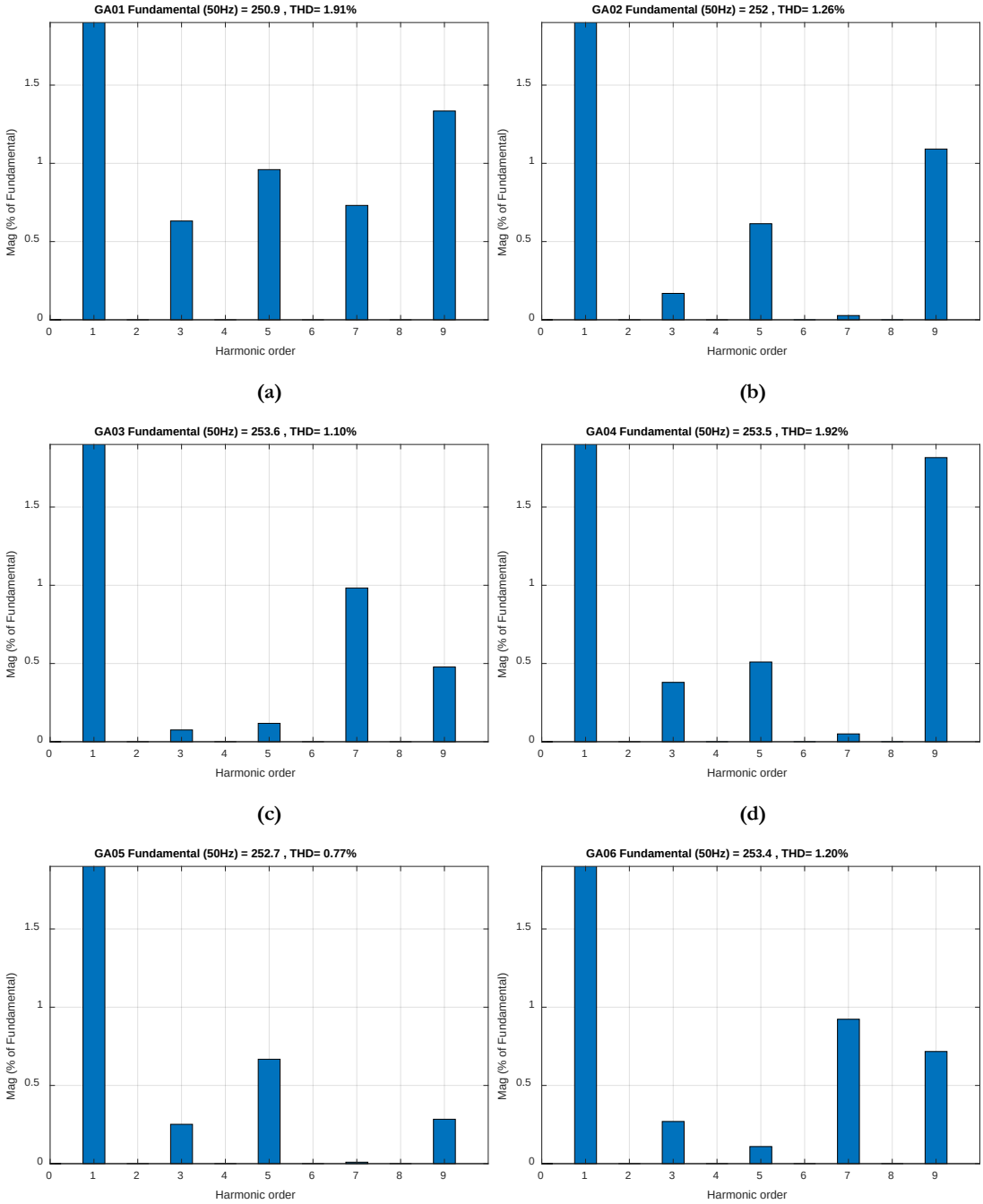

Figure 11 Frequency spectrum and fundamental harmonic values of algorithms at N=20, T=100

(a) GA01; **(b)** GA02; **(c)** GA03; **(d)** GA04; **(e)** GA05; **(f)** GA06

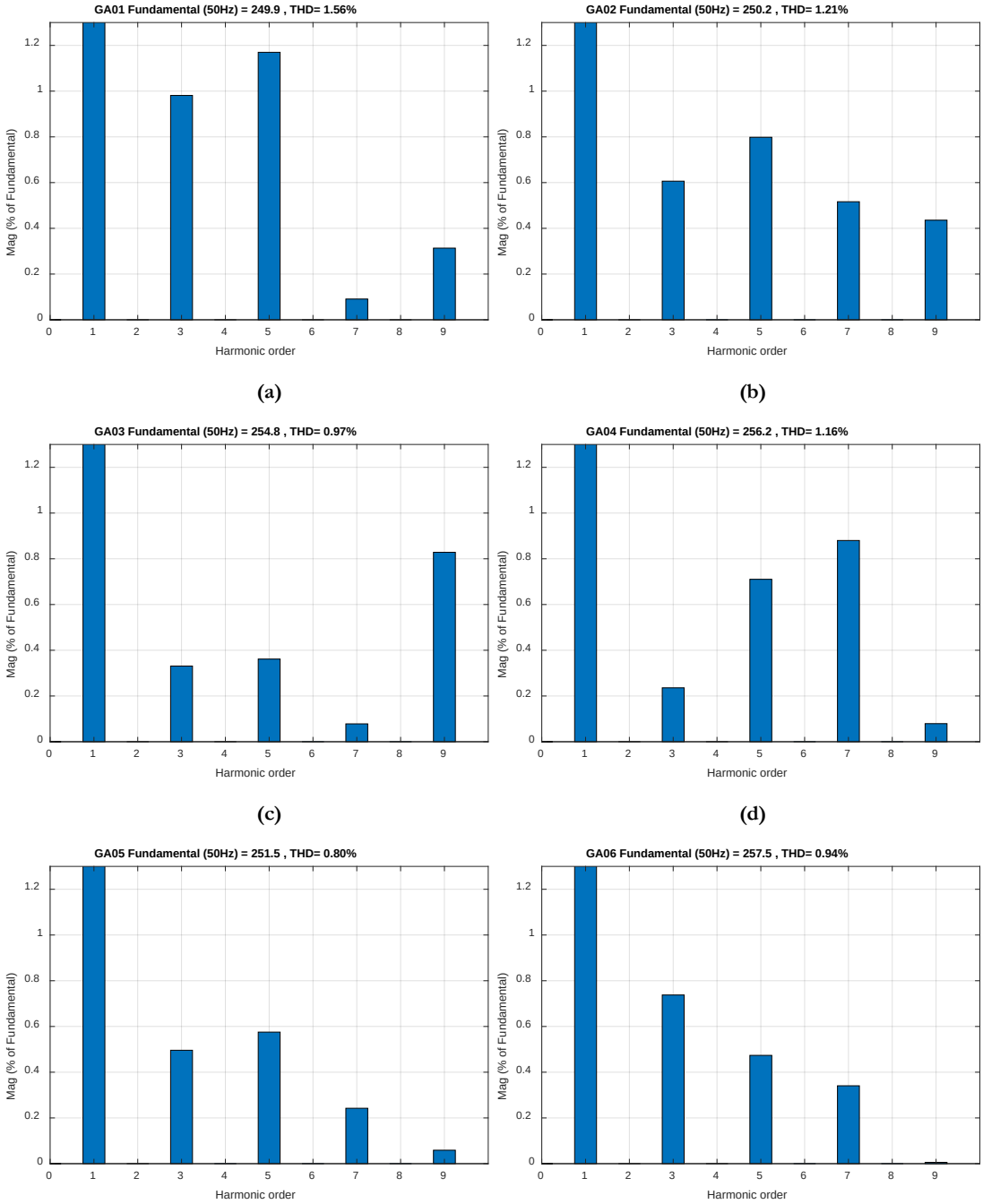

Figure 12 Frequency spectrum and fundamental harmonic values of algorithms at N=100, T=20

(a) GA01; **(b)** GA02; **(c)** GA03; **(d)** GA04; **(e)** GA05; **(f)** GA06

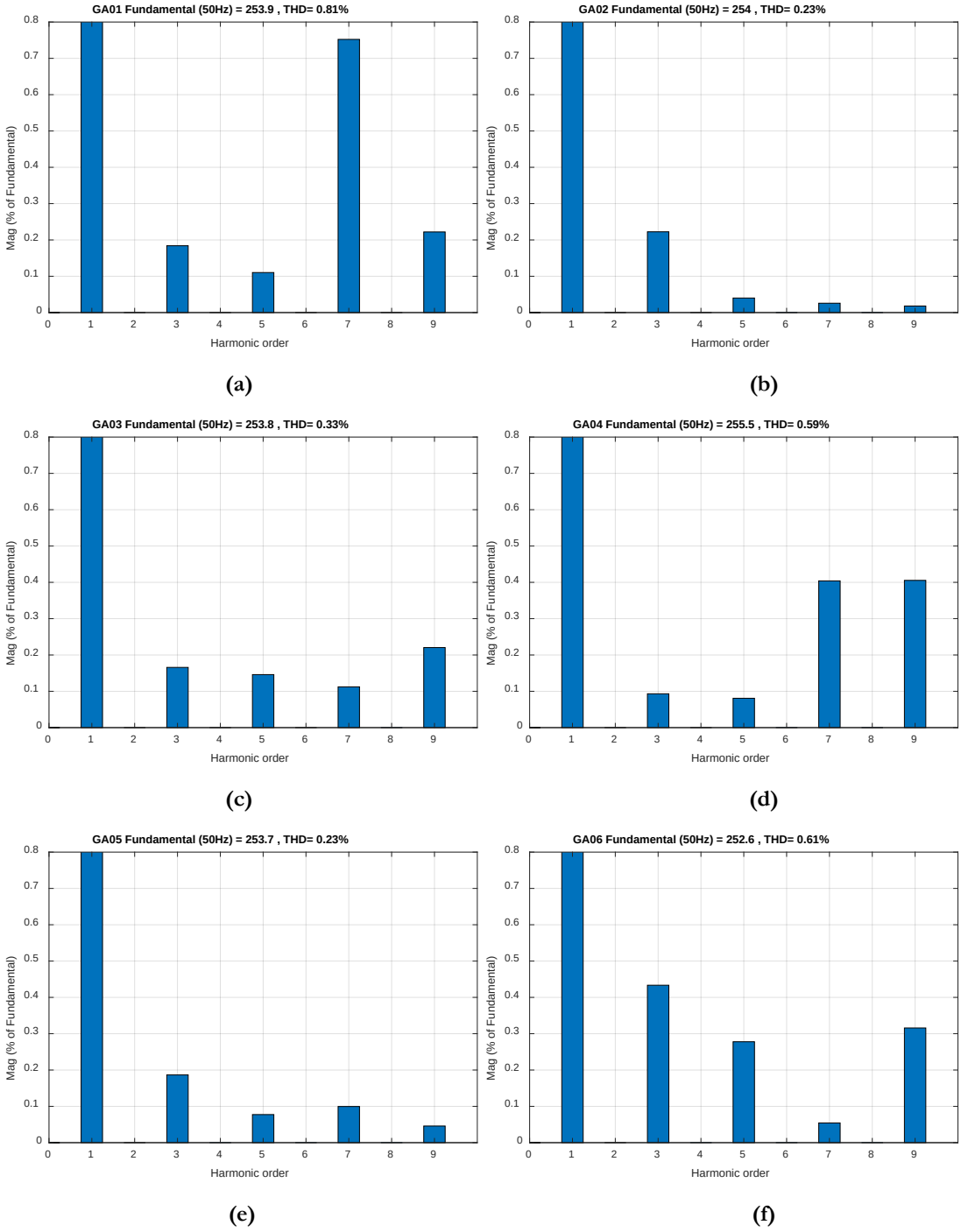

Figure 13 Frequency spectrum and fundamental harmonic values of algorithms at N=100, T=100

(a) GA01; **(b)** GA02; **(c)** GA03; **(d)** GA04; **(e)** GA05; **(f)** GA06

5. Conclusions

In this study, six genetic algorithm variants employing different generation replacement strategies were evaluated in terms of the balance between diversity and elitism and comparatively analyzed on a real-world optimization problem. The results obtained under four scenarios representing different resource conditions revealed that the performance of the algorithms depends not only on their structural design but also significantly on the resource profile of the environment in which they are applied. While strategies with strong elitism demonstrated superior performance in scenarios with high population sizes and iteration

counts, diversity-oriented approaches stood out particularly in resource-constrained settings. These findings emphasize that, rather than seeking a universally superior algorithm, selection should be based on the principle of suitability to the specific problem and available resources.

These results offer a concrete roadmap for identifying which type of generation replacement strategy may be more effective under which resource conditions in real-world optimization problems. This evaluation approach can potentially be extended beyond genetic algorithms and adapted to other metaheuristic algorithms. In particular, conducting similar comparative analyses on multi-objective or constrained optimization problems may further strengthen the scope and validity of the insights obtained.

Declaration of Ethical Standards

As the sole author of this study, I confirm that the research was conducted in full compliance with all ethical standards.

Declaration of Competing Interest

As the sole author of this study, I declare that I have no conflict of interest.

Funding / Acknowledgements

As the sole author, I declare that this study received no external funding.

Data Availability

No datasets were generated or analyzed during the current study.

References

Ahn, C. W., & Ramakrishna, R. S. (2003). Elitism-based compact genetic algorithms. *IEEE Transactions on Evolutionary Computation*, *7*(4), 367–385. https://doi.org/10.1109/TEVC.2003.814633

Alhijawi, B., & Awajan, A. (2024). Genetic algorithms: Theory, genetic operators, solutions, and applications. *Evolutionary Intelligence*, *17*(3), 1245–1256. https://doi.org/10.1007/s12065-023-00822-6

Ali, K. B., Telmoudi, A. J., & Gattoufi, S. (2020). Improved Genetic Algorithm Approach Based on New Virtual Crossover Operators for Dynamic Job Shop Scheduling. *IEEE Access*, *8*, 213318–213329. https://doi.org/10.1109/ACCESS.2020.3040345

Bakirtzis, A. G., Biskas, P. N., Zoumas, C. E., & Petridis, V. (2002). Optimal power flow by enhanced genetic algorithm. *IEEE Transactions on Power Systems*, *17*(2), 229–236. https://doi.org/10.1109/TPWRS.2002.1007886

Bektaş, Y., Karaca, H., Taha, T. A., & Zaynal, H. I. (2023). Red deer algorithm-based selective harmonic elimination technique for multilevel inverters. *Bulletin of Electrical Engineering and Informatics*, *12*(5), 2643–2650. https://doi.org/10.11591/eei.v12i5.5160

Bertin, T., Despesse, G., & Thomas, R. (2023). Comparison between a Cascaded H-Bridge and a Conventional H-Bridge for a 5-kW Grid-Tied Solar Inverter. *Electronics*, *12*(8), 1–25. https://doi.org/10.3390/electronics12081929

Brouwer, N., Dijkzeul, D., Koppenhol, L., Pijning, I., & van den Berg, D. (2022). Survivor selection in a crossoverless evolutionary algorithm. *Proceedings of the Genetic and Evolutionary Computation Conference Companion*, 1631–1639. https://doi.org/10.1145/3520304.3533950

Dahidah, M. S. A., Konstantinou, G., & Agelidis, V. G. (2015). A Review of Multilevel Selective Harmonic Elimination PWM: Formulations, Solving Algorithms, Implementation and Applications. *IEEE Transactions on Power Electronics*, *30*(8), 4091–4106. IEEE Transactions on Power Electronics. https://doi.org/10.1109/TPEL.2014.2355226

Disney, S. M., Naim, M. M., & Towill, D. R. (2000). Genetic algorithm optimisation of a class of inventory control systems. *International Journal of Production Economics*, *68*(3), 259–278. https://doi.org/10.1016/S0925-5273(99)00101-2

Du, H., Wang, Z., Zhan, W., & Guo, J. (2018). Elitism and Distance Strategy for Selection of Evolutionary Algorithms. *IEEE Access*, *6*, 44531–44541. https://doi.org/10.1109/ACCESS.2018.2861760

El-Hosainy, A., Hamed, H. A., Azazi, Haitham. Z., & El-Kholy, E. E. (2017). A review of multilevel inverter topologies, control techniques, and applications. *2017 Nineteenth International Middle East Power Systems Conference (MEPCON)*, 1265–1275. https://doi.org/10.1109/MEPCON.2017.8301344

Gen, M., & Cheng, R. (1999). *Genetic Algorithms and Engineering Optimization*. John Wiley & Sons, Ltd. https://doi.org/10.1002/9780470172261

Halim, Z., Yousaf, M. N., Waqas, M., Sulaiman, M., Abbas, G., Hussain, M., Ahmad, I., & Hanif, M. (2021). An effective genetic algorithm-based feature selection method for intrusion detection systems. *Computers & Security*, *110*, 102448. https://doi.org/10.1016/j.cose.2021.102448

Hassanat, A., Almohammadi, K., Alkafaween, E., Abunawas, E., Hammouri, A., & Prasath, V. B. S. (2019). Choosing Mutation and Crossover Ratios for Genetic Algorithms—A Review with a New Dynamic Approach. *Information*, *10*(12), 1–36. https://doi.org/10.3390/info10120390

Holland, J. H. (1992). *Adaptation in Natural and Artificial Systems: An Introductory Analysis with Applications to Biology, Control, and Artificial Intelligence* (5th ed.). The MIT Press. https://doi.org/10.7551/mitpress/1090.001.0001

Hong, T.-P., Wang, H.-S., Lin, W.-Y., & Lee, W.-Y. (2002). Evolution of Appropriate Crossover and Mutation Operators in a Genetic Process. *Applied Intelligence*, *16*(1), 7–17. https://doi.org/10.1023/A:1012815625611

Katoch, S., Chauhan, S. S., & Kumar, V. (2021). A review on genetic algorithm: Past, present, and future. *Multimedia Tools and Applications*, *80*(5), 8091–8126. https://doi.org/10.1007/s11042-020-10139-6

Kim, K., & Han, I. (2000). Genetic algorithms approach to feature discretization in artificial neural networks for the prediction of stock price index. *Expert Systems with Applications*, *19*(2), 125–132. https://doi.org/10.1016/S0957-4174(00)00027-0

Lingom, P. M., Song-Manguelle, J., Nyobe-Yome, J. M., & Doumbia, M. L. (2024). A Comprehensive Review of Compensation Control Techniques Suitable for Cascaded H-Bridge Multilevel Inverter Operation with Unequal DC Sources or Faulty Cells. *Energies*, *17*(3), 1–17. https://doi.org/10.3390/en17030722

Osman, M. S., Abo-Sinna, M. A., & Mousa, A. A. (2004). A solution to the optimal power flow using genetic algorithm. *Applied Mathematics and Computation*, *155*(2), 391–405. https://doi.org/10.1016/S0096-3003(03)00785-9

Smith, M. G., & Bull, L. (2005). Genetic Programming with a Genetic Algorithm for Feature Construction and Selection. *Genetic Programming and Evolvable Machines*, *6*(3), 265–281. https://doi.org/10.1007/s10710-005-2988-7

Sunddararaj, S. P., Srinivasarangan, S. R., & Nallusamy, S. (2020). An Extensive Review of Multilevel Inverters Based on Their Multifaceted Structural Configuration, Triggering Methods and Applications. *Electronics*, *9*(3), 1–33. https://doi.org/10.3390/electronics9030433

Yang, K., Zhang, Q., Zhang, J., Yuan, R., Guan, Q., Yu, W., & Wang, J. (2017). Unified Selective Harmonic Elimination for Multilevel Converters. *IEEE Transactions on Power Electronics*, *32*(2), 1579–1590. IEEE Transactions on Power Electronics. https://doi.org/10.1109/TPEL.2016.2548080

Zhang, F., Cao, X., & Yang, D. (2008). Intelligent scheduling of public traffic vehicles based on a hybrid genetic algorithm. *Tsinghua Science and Technology*, *13*(5), 625–631. https://doi.org/10.1016/S1007-0214(08)70103-2

Zhang, J., Zhuang, J., Du, H., & Wang, S. (2009). Self-organizing genetic algorithm based tuning of PID controllers. *Information Sciences*, *179*(7), 1007–1018. https://doi.org/10.1016/j.ins.2008.11.038

ELECTRICAL ENGINEERING AND ENERGY

OPEN ACCESS

Investigation of the Effects of TiO_2 and Al_2O_3 Nanoparticles on Exhaust Gas Temperature in Direct Injection Gasoline Engines

Mehmet Selman Gokmen[1], Hasan Aydogan[2]

[1] Necmettin Erbakan University, Seydişehir Vocational High School, Department of Motor Vehicles and Transportation Technologies., Konya Türkiye

[2] Selcuk University, Technology Faculty, Department of Mechanical Engineering, Campus, Konya Türkiye

Submitted: 10 April 2025
Accepted: 21 April 2025
Published: 30 April 2025

Corresponding author
Mehmet Selman Gokmen,
msgokmen@erbakan.edu.tr

Copyright, Distributed under Creative Commons CC-BY 4.0

Abstract:

In this study, the effects of Al_2O_3 and TiO_2 nanoparticles on exhaust gas temperature (EGT) in a direct injection gasoline engine were experimentally investigated. The Al_2O_3 and TiO_2 nanoparticles were added to fuel mixtures in concentrations of 3.5 ppm and 7 ppm, and tested at engine speeds of 1500, 2500, and 3500 rpm. The results demonstrate that nanoparticles enhance heat transfer within the combustion chamber, leading to higher combustion temperatures. This translates to greater energy production in terms of combustion efficiency and engine performance. In conclusion, the use of Al_2O_3 and TiO_2 nanoparticles as fuel additives shows potential for improving engine performance and offers a novel approach for controlling exhaust gas temperature.

Keywords Exhaust gas temperature, Nanoparticles, Gasoline engine

1. Introduction

Fossil fuels are among the most widely used energy sources for power generation, with fuels like gasoline serving as a primary energy source in internal combustion engines. However, the combustion of fossil fuels results in harmful emissions that contribute to global environmental problems and pose significant health risks (Fennell et al., 2014). Gasoline-powered engines emit harmful gases such as carbon dioxide (CO_2), carbon monoxide (CO), nitrogen oxides (NOx), and hydrocarbons (HC) into the atmosphere. These emissions exacerbate air pollution, contributing to global warming, ozone layer depletion, and acid rain. Considering the global environmental impacts of emissions from gasoline engines, studies on technological improvements and fuel additives aimed at reducing these emissions are of paramount importance (Acaroğlu & Aydoğan, 2012).

In this context, various technical solutions have been developed to achieve environmental improvements in gasoline engines. While direct injection gasoline engines have the potential to enhance engine efficiency and optimize fuel consumption, controlling harmful emissions remains challenging due to high exhaust gas temperatures. Additionally, exhaust gas temperature (EGT) is a critical parameter that directly affects engine performance, combustion efficiency, and emissions (Fushimi et al., 2016). High exhaust gas temperatures, particularly at elevated levels, lead to an increase in NOx emissions, which exacerbates environmental damage. NOx emissions are produced during high-temperature combustion and have

adverse effects on both human health and ecosystems. Therefore, controlling and maintaining exhaust gas temperatures at optimal levels is a critical goal for both engine performance and environmental management in gasoline engines(Thurston et al., 2023).

Failure to regulate exhaust gas temperatures also imposes thermal stress on engine components, accelerating wear and reducing the engine's lifespan. High temperatures can affect the long-term durability of components such as exhaust valves, turbocharger systems, and exhaust manifolds. As such, temperature control is vital for optimizing engine efficiency and ensuring engine longevity. Conversely, low exhaust gas temperatures can prevent complete combustion, resulting in increased emissions of CO and HC, which are harmful to the environment. Therefore, maintaining exhaust gas temperatures within an optimal range is essential for both engine performance and emissions control(Hosseini & Chitsaz, 2023).

In recent years, nanotechnology has provided new opportunities to improve fuel efficiency and reduce emissions in the automotive industry. By adding nanoparticles to fuels, the combustion process can be optimized, allowing for better control of exhaust gas temperatures. Nanoparticles such as Al_2O_3 (Aluminum Oxide) and TiO_2 (Titanium Oxide), due to their high thermal conductivity and large surface area, promote more homogeneous fuel combustion. The use of nanoparticles as fuel additives can improve combustion efficiency(Zhang et al., 2022), particularly by achieving higher combustion temperatures, and reduce harmful emissions. TiO_2 contributes to more efficient combustion within the combustion chamber due to its high thermal conductivity, while Al_2O_3 provides more balanced and gradual temperature control(Chaimanatsakun et al., 2024). As a result, nanoparticles not only enhance engine performance but also reduce exhaust gas temperatures and protect engine components from overheating(Khameneian et al., 2022).

The addition of nanoparticles to fuels presents a significant opportunity to lower exhaust gas temperatures, improving engine performance and reducing emissions(G M et al., 2023). While high temperatures are indicative of efficient combustion, excessive temperatures can increase NOx emissions, leading to environmental damage(Kim et al., 2017). Nanoparticles can be utilized to balance temperature increases, thereby enhancing combustion efficiency while keeping harmful emissions under control. Al_2O_3 and TiO_2 nanoparticles, in this context, hold great potential in terms of thermal management and engine performance.

The aim of this study is to investigate the effects of Al_2O_3 and TiO_2 nanoparticles on exhaust gas temperature in direct injection gasoline engines and to experimentally analyze the effects of different nanoparticle concentrations on engine performance. This study seeks to contribute to the literature by revealing the potential impacts of nanoparticles on engine efficiency and emissions control. Specifically, analyzing the effects of Al_2O_3 and TiO_2 nanoparticles on exhaust gas temperature at different engine speeds highlights the potential of fuel additives to improve engine performance. Additionally, evaluating the effects of nanoparticles on the combustion process represents an important step toward enhancing environmental sustainability in engine technologies.

2. Material and Method

The fuel mixtures were prepared using 12 nm-sized Al_2O_3 and TiO_2 nanoparticles with similar properties. Preliminary screening tests were conducted to determine the appropriate fuel ratios, and it was observed that agglomeration occurred when the total particle concentration exceeded 15 ppm. Therefore, the total particle concentration was limited to a maximum of 14 ppm. During the preparation of the mixtures, an ultrasonic homogenizer and a mechanical stirrer were used to ensure the homogeneous dispersion of the nanoparticles within the fuel. As shown in Table 1, a three-level factorial design method was applied for each nanoparticle, resulting in eight different mixtures containing nanoparticles. FuelSave unleaded

gasoline, supplied by Shell, was used as the base fuel for preparing the mixtures and for comparison.

Table 1. Particle Mixture Ratios

Factors	Levels		
Al_2O_3 (ppm)	0	3.5	7
TiO_2 (ppm)	0	3.5	7

In the tests, a Volkswagen gasoline engine, whose specifications are provided in Table 2, was used. The exhaust gas outlet temperatures were measured using a CEM DT8820 compact device with a tolerance of ±1 °C. The measurements were taken when the engine coolant temperature reached 90 °C, using a metal probe placed at the midpoint of the exhaust pipe to minimize the influence of external factors. Five measurements were taken for each engine speed, and the averages of these measurements were calculated.

Table 2. Test Engine Specifications

Property	Specifications
Model	1.2 TSI, Direct Injection
Engine Volume	1197 cm^3
Cylinder Number	4
Compression Ratio	10:1
Engine Power	77 kW
Engine Torque	175 Nm

3. Results

The test results presented in Table 3 were subjected to variance analysis, resulting in an R^2 value of 98.35% and a Mean Absolute Error (MAE) of 12.40. In Figure 1, the response surface graph related to TiO_2 is provided, while in Figure 2, the graph for Al_2O_3 is displayed. Additionally, in the mathematical expression of the response surface function shown in Equation 1, "TiO_2" and "Al_2O_3" represent the particle quantities in ppm, and "ES" denotes the engine speed in rpm.

$$EGT = -21{,}8704 + 0{,}265042 * ES + 1{,}3869 * Al_2O_3 + 25{,}746 * TiO_2 - 0{,}0000233056 * ES^2 - 0{,}000869048 * MH * Al_2O_3 - 0{,}0177024 * ES * TiO_2 - 0{,}218821 * {Al_2O_3}^2 + 2{,}0085 * Al_2O_3 * TiO_2 + 1{,}0941 * {TiO_2}^2 + 0{,}0 * ES^2 * TiO_2 + 0{,}000278912 * ES * {Al_2O_3}^2 - 0{,}0532796 * ES * Al_2O_3 * TiO_2 - 0{,}000945578 * ES * {TiO_2}^2 \quad (1)$$

According to the data presented in the table, the changes in exhaust gas temperature (EGT) at different engine speeds (1500, 2500, 3500 rpm) and nanoparticle concentrations (Al_2O_3 and TiO_2) are significant. In tests conducted with standard gasoline fuel, a noticeable increase in EGT was observed as the engine speed increased. Specifically, the temperature rose from 314°C at 1500 rpm to 598°C at 3500 rpm. These values serve as control data obtained without the addition of nanoparticles and provide a fundamental reference for comparing other fuel mixtures. When Al_2O_3 nanoparticles were added to the fuel at a concentration of 3.5 ppm, EGT increased across all engine speeds compared to the control values. At 1500 rpm, the temperature rose to 327°C, and at 3500 rpm, it reached 614°C. These results indicate that even at low concentrations, Al_2O_3 enhances combustion efficiency, leading to a gradual and stable temperature increase.

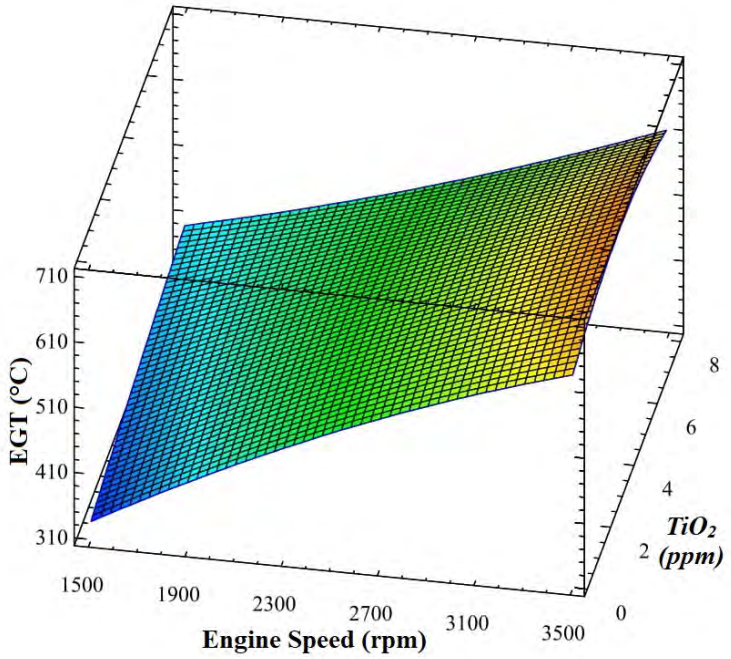

Figure 1. Response surface plot of TiO_2 nanoparticles for EGT

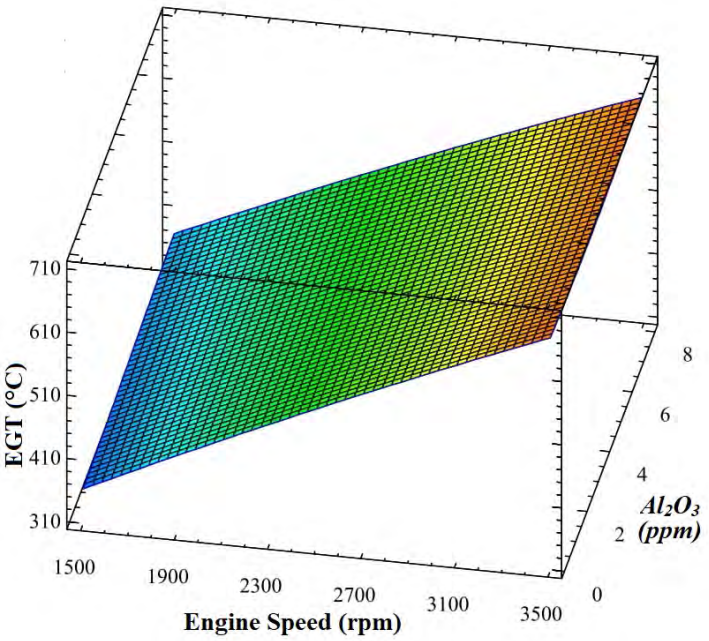

Figure 2. Response surface plot of Al_2O_3 nanoparticles for EGT

Table 3. Measurement Results for EGT

Fuel	ES (rpm)	Al_2O_3 (ppm)	TiO_2 (ppm)	EGT (°C)
Gasoline	1500	0	0	314
	2500	0	0	503
	3500	0	0	598
Fuel 1	1500	3,5	0	327
	2500	3,5	0	518
	3500	3,5	0	614
Fuel 2	1500	7	0	339
	2500	7	0	491
	3500	7	0	675
Fuel 3	1500	0	3,5	355
	2500	0	3,5	532
	3500	0	3,5	695
Fuel 4	1500	3,5	3,5	346
	2500	3,5	3,5	511
	3500	3,5	3,5	658
Fuel 5	1500	7	3,5	395
	2500	7	3,5	504
	3500	7	3,5	637
Fuel 6	1500	0	7	375
	2500	0	7	497
	3500	0	7	642
Fuel 7	1500	3,5	7	397
	2500	3,5	7	515
	3500	3,5	7	632
Fuel 8	1500	7	7	399
	2500	7	7	511
	3500	7	7	639

When the Al_2O_3 concentration was raised to 7 ppm, a temperature of 339°C was recorded at 1500 rpm, and it further increased to 675°C at 3500 rpm. Interestingly, at 2500 rpm, the EGT dropped to 491°C, falling below the control value. This suggests that using higher concentrations of Al_2O_3 may disrupt homogeneity in the combustion chamber, negatively affecting efficiency. Therefore, it is evident that maintaining an optimal nanoparticle concentration is critical for effective performance. In the case of TiO_2 nanoparticles added at a concentration of 3.5 ppm, there was a notable increase in EGT. The temperature rose to 355°C at 1500 rpm and reached 695°C at 3500 rpm. Due to TiO_2's high thermal conductivity, it enabled faster heat transfer, particularly at higher engine speeds, significantly improving combustion efficiency. This

demonstrates that TiO_2 is more effective at increasing temperatures compared to Al_2O_3, and it has a positive impact on engine performance.

When Al_2O_3 and TiO_2 were combined at a concentration of 3.5 ppm, a more balanced temperature increase was observed at both low and medium engine speeds. The temperature rose to 346°C at 1500 rpm and 658°C at 3500 rpm. These findings suggest that the combined use of both nanoparticles provides a balanced thermal effect, helping to control excessive temperature increases and preventing thermal stress on engine components. The effects of using higher concentrations of nanoparticles are also noteworthy. When Al_2O_3 and TiO_2 were combined at a concentration of 7 ppm, the EGT reached 399°C at 1500 rpm, showing a significant increase. However, at 2500 and 3500 rpm, the temperature increases were more limited. This suggests that higher nanoparticle concentrations may enhance efficiency at lower engine speeds but may be less effective at higher speeds than expected.

Overall, Al_2O_3 and TiO_2 nanoparticles have demonstrated positive effects in controlling EGT and improving engine performance. However, exceeding a certain concentration of nanoparticles can disrupt homogeneity in the combustion chamber, limiting the temperature increase and reducing efficiency. Therefore, adding nanoparticles to fuel at optimal concentrations is crucial for enhancing engine performance and maintaining control over EGT.

4. Conclusions

In this study, the effects of Al_2O_3 and TiO_2 nanoparticles on the exhaust gas temperature of a direct injection gasoline engine were experimentally investigated. Tests conducted with nanoparticles at different concentrations (3.5 ppm and 7 ppm) revealed that exhaust gas temperature varied depending on both engine speed and the type and concentration of the nanoparticles. The results showed that TiO_2 nanoparticles, in particular, led to significant increases in exhaust gas temperature in relation to engine speed. In contrast, Al_2O_3 nanoparticles, with their lower thermal conductivity, exhibited a more balanced and gradual effect on exhaust gas temperature. However, the lower-than-expected temperature values observed with 7 ppm TiO_2 indicated that excessive nanoparticle loading may disrupt combustion homogeneity, thereby reducing efficiency. In conclusion, both Al_2O_3 and TiO_2 nanoparticles show potential as additives to enhance engine performance and combustion efficiency. Due to its high thermal conductivity, TiO_2 facilitates faster heat transfer and thus improves combustion efficiency, while Al_2O_3 provides a more balanced temperature increase, contributing to the engine's longevity. Increasing the nanoparticle concentration can improve efficiency up to a certain point, but excessive nanoparticle loading may adversely affect the combustion process and limit the temperature rise. Therefore, the potential of nanoparticles to enhance engine performance and reduce harmful emissions must be optimized through careful use.

To fully optimize the positive effects of nanoparticles on engine performance and emissions control, the optimal nanoparticle concentration must be carefully determined, and excessive loading should be avoided. The effects of nanoparticles on harmful emissions, especially NOx, should be evaluated through more comprehensive studies. In the long term, the effects of nanoparticles on engine component wear and thermal stress should be investigated, and new-generation nanotechnologies should be developed to create more efficient and sustainable engines.

Declaration of Ethical Standards

As the authors of this study, we declare that he complies with all ethical standards.

Credit Authorship Contribution Statement

M.S. Gokmen: Investigation, Experimentation, Writing, Review & Editing.
H. Aydogan: Investigation, Writing, Review & Editing, Supervision.

Declaration of Competing Interest

The authors declared that they have no conflict of interest.

Funding / Acknowledgements

The authors were supported within the scope of the research by the Selcuk University Scientific Research Projects Unit with Project No: 21211039.

Data Availability

No datasets were generated or analyzed during the current study.

References

Acaroğlu, M., & Aydoğan, H. (2012). Biofuels energy sources and future of biofuels energy in Turkey. Biomass and Bioenergy, 36, 69–76. https://doi.org/10.1016/j.biombioe.2011.10.004

Chaimanatsakun, A., Sawatmongkhon, B., Sittichompoo, S., & Theinnoi, K. (2024). Effects of reformed exhaust gas recirculation (REGR) of ethanol-gasoline fuel blends on the combustion and emissions of gasoline direct injection (GDI) engine. Fuel, 355. https://doi.org/10.1016/j.fuel.2023.129506

Fennell, D., Herreros, J., & Tsolakis, A. (2014). Improving gasoline direct injection (GDI) engine efficiency and emissions with hydrogen from exhaust gas fuel reforming. International Journal of Hydrogen Energy, 39(10), 5153–5162. https://doi.org/10.1016/j.ijhydene.2014.01.065

Fushimi, A., Kondo, Y., Kobayashi, S., Fujitani, Y., Saitoh, K., Takami, A., & Tanabe, K. (2016). Chemical composition and source of fine and nanoparticles from recent direct injection gasoline passenger cars: Effects of fuel and ambient temperature. Atmospheric Environment, 124, 77–84. https://doi.org/10.1016/j.atmosenv.2015.11.017

G M, L. L., M, C. Das, Jayabal, R., S, M., D, S., & N, M. (2023). Experimental evaluation and neural network modelling of reactivity-controlled compression ignition engine using cashew nut shell oil biodiesel-alumina nanoparticle blend and gasoline injection. Energy, 282. https://doi.org/10.1016/j.energy.2023.128923

Hosseini, M., & Chitsaz, I. (2023). Knock probability determination in a turbocharged gasoline engine through exhaust gas temperature and artificial neural network. Applied Thermal Engineering, 225. https://doi.org/10.1016/j.applthermaleng.2023.120217

Khameneian, A., Wang, X., Dice, P., Naber, J. D., Shahbakhti, M., Archer, C., Moilanen, P., Glugla, C., & Huberts, G. (2022). A real-time control-oriented discrete nonlinear model development for in-cylinder air charge, residual gas and temperature prediction of a Gasoline Direct Injection engine using cylinder, intake and exhaust pressures. Control Engineering Practice, 119. https://doi.org/10.1016/j.conengprac.2021.104978

Kim, J., Chun, K. M., Song, S., Baek, H. K., & Lee, S. W. (2017). The effects of hydrogen on the combustion, performance and emissions of a turbo gasoline direct-injection engine with exhaust gas recirculation. International Journal of Hydrogen Energy, 42(39), 25074–25087. https://doi.org/10.1016/j.ijhydene.2017.08.097

Thurston, M. G., Sullivan, M. R., & McConky, S. P. (2023). Exhaust-gas temperature model and prognostic feature for diesel engines. Applied Thermal Engineering, 229. https://doi.org/10.1016/j.applthermaleng.2023.120578

Zhang, X., Song, C., Lyu, G., Li, Y., Qiao, Y., & Li, Z. (2022). Physicochemical analysis of the exhaust soot from a gasoline direct injection (GDI) engine and the carbon black. Fuel, 322. https://doi.org/10.1016/j.fuel.2022.124262

ELECTRICAL ENGINEERING AND ENERGY

OPEN ACCESS

Comparative Analysis of Grid-Following (GFL) and Grid-Forming (GFM) Inverters: Control and Transition Capabilities

Fatih Burak [1] and Hulusi Karaca [2]

[1] Electric and Energy, Bor Vocational School, Nigde Omer Halisdemir University, Bor, Nigde, Türkiye

[2] Electrical & Electronics Engineering, Institute of Science, Selcuk University, Selcuklu, Konya, Türkiye

Submitted: 8 April 2025
Accepted: 25 April 2025
Published: 30 April 2025

Corresponding author
Fatih Burak,
fatihburak@ohu.edu.tr

Copyright, Distributed under Creative Commons CC-BY 4.0

Abstract: In recent years, interest in integration of renewable energy (RE) sources (particularly Wind Energy Systems - WES) into the electrical grid for sustainable, innovative solutions and a greener future continues to grow exponentially. To date, most RE sources have been connected to the grid through traditional grid-following inverters (GFL). Although this control method promises grid compatibility and lower complexity, the unpredictable variability of these eco-friendly RE sources leads to undesirable effects when taken into account. With the increasing interaction of renewable energy sources in today's grid, new challenges arise—such as voltage/frequency regulation and the reduction of overall system inertia—that cannot be resolved with conventional grid-following inverters (GFL). Therefore, the concept of grid-forming inverters (GFM) has been adopted.

The aim of this study is to examine the comparison between grid-forming inverters and traditional grid-following inverters, particularly focusing on droop control, and to regulate the simulated test results with appropriate control systems. For this purpose, the study first compares GFM—based on different control techniques (droop, virtual synchronous generator, and synchronverter control) in the literature—with the conventional GFL technique. The circuit tested in this study involves a 40 kVA-rated inverter supplying relevant loads and the grid, with GFL and GFM control modes analyzed separately. Finally, the potential effects of inverters on load variation and grid outages will be considered.

Keywords: Grid-Following Inverter (GFL), Grid-Forming Inverter (GFM).

1. Introduction

When examining the market shares of wind and solar systems—the two main drivers of renewable energy globally—2022 will be remembered as a significant milestone. That year, renewables hit a record high, accounting for 12% of global electricity generation. Another noteworthy point was that fossil-based generation declined for the first time ever. For Türkiye, in 2023, solar energy's share rose from 4.9% (2022) to 5.7% (2023), while wind energy contributed approximately 34 TWh, securing a 10.5% share (2023) of total electricity production. This marked a crucial milestone in the transition from fossil-based generation to clean energy (Serkan Aslan, 2023; Wiatros-Motyka, 2023).

Considering these developments, it no longer seems far away for grid models powered solely by renewable energy—rather than traditional synchronous generator (SG)-based systems—to become part of modern

power networks. However, this potential shift requires a transition period. Because the declining share of SG-based energy in favor of wind and solar sources leads to grid control challenges that must be addressed. First, power systems were originally designed around traditional synchronous generators (SGs). The quality indicators of power systems rely on the behaviour and control of these machines, summarized in four key requirements:

- Constant frequency (e.g., 50 Hz or 60 Hz);
- Constant voltage amplitude;
- System protection during faults;
- A sinusoidal voltage source with low harmonic content and limited harmonic interactions.

For grid-connected Wind Energy Systems (WES)—a type of renewable energy source—four additional requirements apply (Mandrile et al., 2021):

- Renewable power plants (RES) must be equipped with appropriate controllers to withstand multiple fault events.
- Higher inertia is needed to limit the Rate of Change of Frequency (RoCoF) and enable protective relay intervention.
- Static converter-based plants (e.g., RES-PV) must exchange reactive power with the grid per Grid Code Regulations.
- Synchronous Generators (SGs) can operate under symmetrical and asymmetrical faults, injecting both positive and negative sequence fault currents. However, static converters cannot inject high short-circuit currents, so they require additional control algorithms to meet Fault Ride-Through (FRT) requirements by enabling positive/negative sequence current injection.

The dominance of modern power electronics-based renewable generation plants has raised concerns about sustaining these mentioned 4+4 fundamental specifications. Traditional SG systems benefit from inertia and Automatic Voltage Regulators (AVR), which are crucial for grid stability. In contrast, power electronics-based systems lack these features, making conventional grid-following inverters (GFL) insufficient for ensuring stability. Two key inverter designs—grid-forming (GFM) and grid-following (GFL) inverters—have been extensively studied. One reason for this focus is that while the input-side converter topology and control vary depending on the renewable source (e.g., WES & PV), the grid-side inverter (dc-ac) remains the same. Thus, grid integration has become a critical research area with diverse control techniques. The input side typically consists of a rectifier or dc-dc converter, both providing a dc output, allowing the input converter to be modeled as a dc link (Ali et al., 2024).

2. Grid-Following Inverter (GFL)

Currently, most renewable energy sources (RES) are connected to the grid via traditional current-controlled grid-following inverters (GFL). Utilizing the phase-locked loop (PLL) concept, GFL inverters must detect the grid frequency and synchronize themselves to it. Additionally, they primarily inject active power by following the maximum power point tracking (MPPT) algorithm dictated by the input-side converter topology. As their name implies, GFL systems inherently follow the grid under all conditions and cannot contribute to grid stability (Rathnayake et al., 2021). The increasing dominance of renewable energy systems in the grid exacerbates this issue, as power electronics-based inverters—with their limited voltage-frequency regulation—replace synchronous generators (SGs) with high rotational inertia. Notably, the energy stored in the DC-link capacitors of inverters is significantly smaller compared to the inertial energy provided by the large masses of traditional systems.

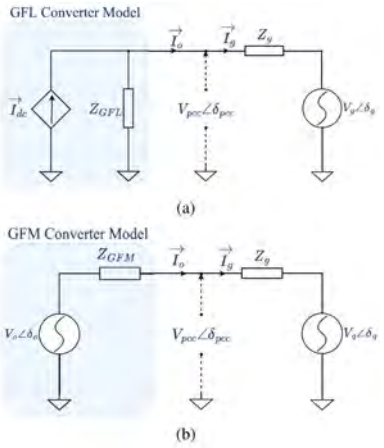

Figure 1 Circuit models of (a) grid-following (GFL) and (b) grid-forming (GFM) systems

The GFL converter can be approximated as a controlled current source with high parallel impedance, as illustrated in Figure 1-a. GFL-based inverter systems regulate currents to inject power or adjust voltage. This is achieved by transforming the three-phase (abc) system into active and reactive components (dq) using Park and Clark transformations (Ali et al., 2024). Active and reactive power are thus regulated via Id and Iq current control. The measured grid voltages and currents feed into the PLL block (Figure 2-a), generating a grid reference angle for these transformations (abc-dq). In the inverter connection circuit (Figure 3), Kirchhoff's voltage law (Equation 1) is applied in the dq-frame to decouple active and reactive power dynamics. As evident, the objective is active-reactive power (PQ) control. However, this PQ-controlled converter system lacks grid regulation capability and exhibits limited small-signal stability performance, particularly in weak grids (Gullu et al., 2024).

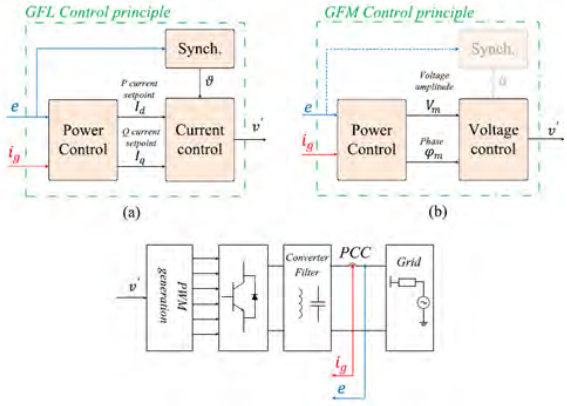

Figure 2 Grid-Following (GFL) (a) and Grid-Forming (GFI) (b) control models (Rosso et al., 2021)

$$\begin{cases} V_d = R \cdot I_d + L \cdot \frac{dI_d}{d_t} - \omega L \cdot I_q + E_d \\ V_q = R \cdot I_q + L \cdot \frac{dI_q}{d_t} + \omega L \cdot I_d + E_q \end{cases} \quad (1)$$

- V_d,V_q : Inverter output voltages (d-q axes)
- I_d,,I_q : Inverter output currents
- R,L : Resistance and inductance of the grid coupling reactance
- w : Grid angular frequency ($\omega = 2\pi f$)
- E_d,E_q : d-q components of the grid voltage (typically E_q=0, E_d =V_{grid})

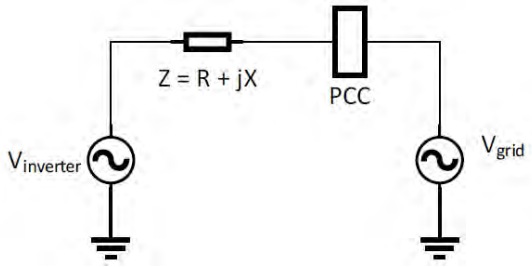

Figure 3 The main electrical interface between the inverter and utility grid (Gullu et al., 2024)

3. Grid Forming Inverter (GFM)

The GFM converter, as illustrated in Figure 1-b, can be represented as a voltage source with low series impedance, symbolizable via Norton or Thevenin equivalents. Unlike grid-following inverters (GFL), grid-forming inverters operate autonomously without grid dependency and possess inherent grid regulation capabilities. While GFL systems regulate power through current control, GFM achieves power control via direct voltage regulation. Crucially, this enables voltage-frequency regulation at the point of common coupling (PCC), compensating for voltage fluctuations (see Figure 2-b). Initially developed to address GFL converter limitations, GFM technology gained early adoption in uninterruptible power supplies (UPS) and microgrid operations due to its control flexibility. Recent studies highlight its stability benefits in both infinite-bus and weak grid applications, making it a focal point in modern power systems research (Ali et al., 2024).

Unlike GFL converters reliant on phase-locked loops (PLLs), many proposed GFM implementations eliminate PLLs, mimicking synchronous machine behaviour to achieve self-synchronization with the grid. Studies demonstrate that PLL-based synchronization in GFL converters adversely affects small-signal stability, particularly under variable grid frequencies (Sevilmiş & Karaca, 2019; Urtasun et al., 2022). Detailed performance comparisons reveal that PLL methods exacerbate stability issues in weak grids. Selecting an appropriate control strategy is critical for GFM operation. Prominent methods include (Rosso et al., 2021):

- Droop control
- Virtual synchronous generator (VSG) control
- Synchronverter
- Power synchronization control (PSC)
- Power balance (matching) control
- Virtual oscillator control (VOC)

3.1 Droop Control

According to Equations (2)-(4), droop control is a simple and highly implementable technique. However, its lack of inherent inertia means it may fail to ensure frequency stability in scenarios with high Rate of Change of Frequency (RoCoF) (Tozak et al., 2024). A key advantage of this method is its ability to regulate voltage and frequency based on measured active and reactive power values without requiring additional synchronization units. Recent observations suggest the need for an adaptive droop control system capable of dynamically adjusting its coefficients to maintain grid synchronization under varying conditions.

$$\dot{\theta}^{ref} = \omega \tag{2}$$

$$\omega = \omega^* + K_{Qv}^{droop}(P^{ref} - P) \tag{3}$$

$$v_{pcc,d}^{ref} = v^* + K_{Qv}^{droop}(Q^{ref} - Q) \tag{4}$$

3.2 Virtual Synchronous Generator (VSG) Control

As previously discussed (Urtasun et al., 2022), grid-forming inverters (GFMs) are fundamentally designed to naturally emulate the capabilities of synchronous generators (SGs) used in conventional systems. This control technique specifically addresses the rotor dynamics of SGs through the swing equation and adapts it for grid control. Equations (5)-(8) describe:

- The frequency output of the SG (Eq. 6),
- The induced voltage (Eq. 7), and
- The excitation current (Eq. 8) for voltage regulation.

Here, the parameters J (inertia constant) and D_p (damping ratio) correspond to the virtual inertia moment required by the grid and the damping coefficient, respectively. By adjusting these values, the virtual synchronous generator (VSG) control can exhibit characteristics similar to droop control (Tozak et al., 2024).

$$\dot{\theta}^{ref} = \omega \tag{5}$$

$$\dot{w} = \frac{1}{Jw}(P^{ref} - P) + \frac{D_P}{J}(w^* - w) \tag{6}$$

$$v_{pcc,abc}^{ref} = 2wM_f i_o \begin{bmatrix} \sin(\theta) \\ \sin(\theta - \frac{2\pi}{3}) \\ \sin(\theta - \frac{4\pi}{3}) \end{bmatrix} \tag{7}$$

$$i_o = \frac{k_p}{M_f}(v^* - \|v_{pcc,dq}\| + \frac{k_i}{M_f}\int(v^* - \|v_{pcc,dq}(\tau)\|)d\tau \tag{8}$$

3.3 Synchronverter

Another control method that emulates synchronous machines is the Synchronverter. Unlike the previously discussed Virtual Synchronous Generator (VSG) control—which primarily focuses on rotor dynamics—the Synchronverter replicates the complete behaviour of a synchronous generator through comprehensive modelling of key parameters, including:

- Electromagnetic torque (T_e)
- Electromotive force (u)
- Reactive power (Q)

These dynamics are formally expressed in Eq. (9). The Synchronverter distinguishes itself through its grid-synchronization capability in grid-connected mode, while offering adjustable parameters, such as inertia damping coefficient and mutual inductance. This adaptability enhances its performance in diverse grid conditions (Rathnayake et al., 2024; Rathnayake et al., 2022).

$$\begin{aligned} T_e &= M_f i_f \langle i, \widetilde{\sin(\theta_r)} \rangle \\ u &= \dot{\theta}_r M_f i_f \widetilde{\sin(\theta_r)} \\ Q &= -\dot{\theta}_r M_f i_f \langle i, \widetilde{\cos(\theta_r)} \rangle \end{aligned} \tag{9}$$

4. Test Results

4.1 GFL Inverter Control Performance Test

The inverter output current and voltage control described by Equation (1) for traditional GFL operation has been implemented in the circuit shown in Figure 9 using MATLAB/Simulink. Figure 4 examines the point of common coupling (PCC) for both islanded and grid-connected scenarios. Current regulation for harmonics is achieved through the LCL filter mentioned previously. The measured grid voltage undergoes axis transformation to the dq-frame for simplified control implementation. As illustrated in Figure 6, synchronization with the grid is established through a synchronous reference frame-based phase-locked loop (SRF-PLL) circuit, which generates the reference angle for output synchronization (Blaabjerg et al., 2006).

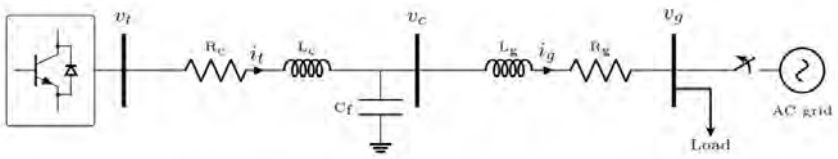

Figure 4 Grid-connected configuration of the comparative inverter topology

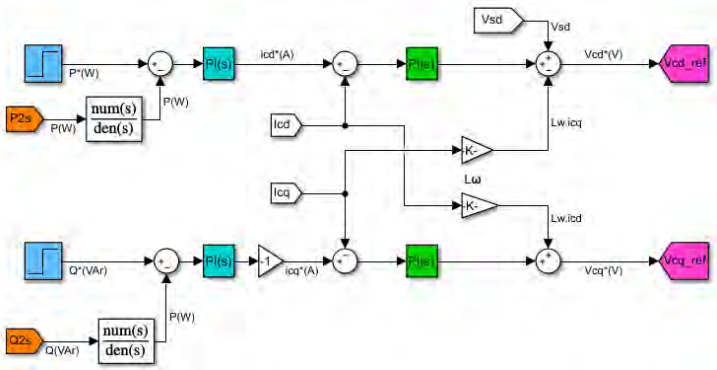

Figure 5 Dual control loops for GFL

The control methodology for the circuit presented in Figure 4 employs a dual-loop control structure. As shown in Figure 5, the outer loop control determines the inverter's active and reactive power by processing the reference power values (P, Q). The current reference values generated by the outer loop enable precise d-axis and q-axis current regulation of the inverter output. Following the inner loop control, the obtained voltage reference values are processed through sinusoidal pulse-width modulation (SPWM) to generate gate signals for the IGBT semiconductors, thereby regulating the inverter output.

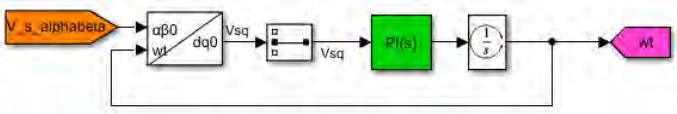

Figure 6 PLL synchronization unit

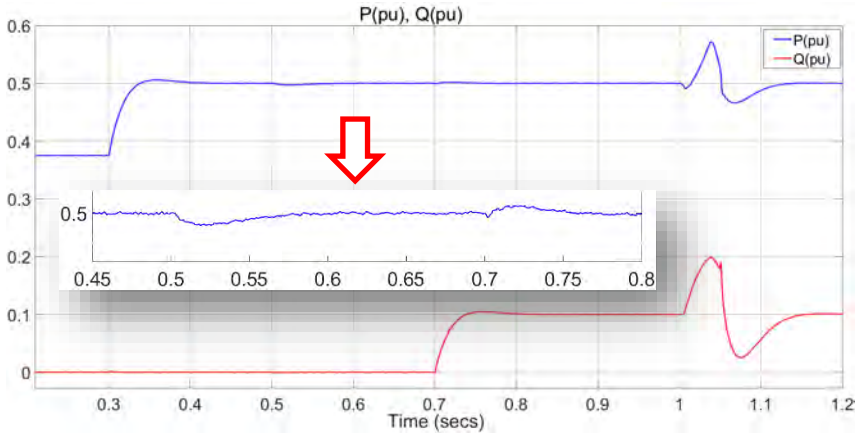

Figure 7 GFL's Active P(pu) and Reactive Q(pu) Power Change

As illustrated in Figure 7, the system demonstrates distinct power response characteristics: the active power rises to 0.5 pu at 0.3 s, followed by reactive power increase at 0.7 s. Notably, the grid-connected mode maintains minimal power fluctuations ($\Delta P < 2\%$, $\Delta Q < 3\%$) during load transitions at t = 0.5 s. However, during the intentional 50 ms islanding event initiated at t = 1 s, the GFL control system exhibits three critical behaviors: (1) unstable active/reactive power regulation with ±15% oscillations, (2) significant power quality degradation, and (3) successful resynchronization within 2 cycles post-grid reconnection. These observations validate the inherent limitations of GFL inverters in maintaining power stability during grid disturbances while confirming their capability for automatic re-synchronization.

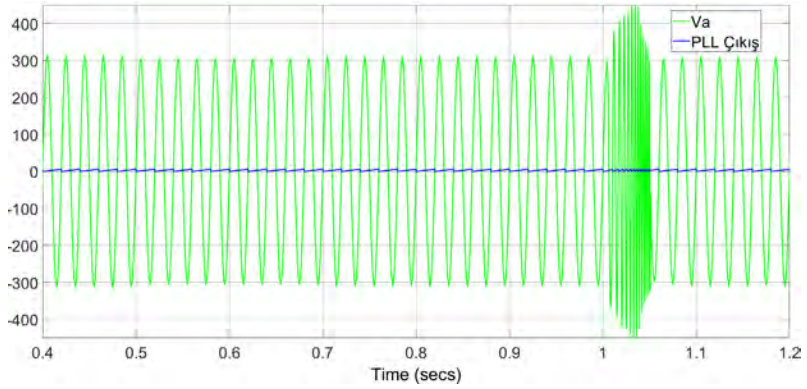

Figure 8 Grid Voltage (V_a) ve PLL Output (w_t)

Figures 8-9 demonstrate the synchronization performance between the PLL output (ωt) and grid voltage (V_a) under different operational conditions. The results show:

- Successful phase locking during normal grid-connected operation
- Immediate loss of synchronization upon grid disconnection, accompanied by frequency deviation exceeding ±2 Hz and transient frequency spikes reaching approx. 250 Hz (for 50 Hz nominal)
- Full synchronization recovery within 3 cycles after grid restoration (50 ms reconnection)

Also, this behaviour quantitatively confirms:

- The PLL's effective tracking capability during stable conditions
- The inherent vulnerability to grid disturbances
- The fast resynchronization characteristic (<100 ms) post-fault.

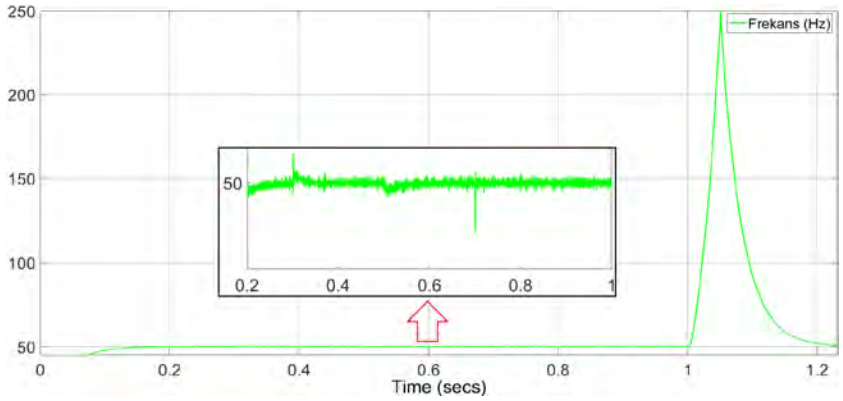

Figure 9 Grid Frequency (Hz)

4.2 GFM Inverter Control Performance Test

In synchronous generators, increased power demand necessitates rotor speed reduction (Salem et al., 2023), consequently inducing frequency decline to provide additional power support. This consistent power-frequency relationship inherent to synchronous machines has been systematically incorporated into grid-forming (GFM) inverters through droop control development (Mohammed et al., 2024). As demonstrated in Figure 10, the implemented droop control mechanism—constructed using Equations (2)-(4)—generates both reference voltage (U_{abc}) and frequency (ω_t) signals.

The governing equations establish two fundamental relationships that the active power (P) is directly regulated through frequency variation, where frequency effectively substitutes the phase angle in power equations. Reactive power (Q) is also controlled via voltage. Accordingly, P and Q represent the measured active and reactive power values, while P_{ref} and Q_{ref} denote their respective reference values. K_p and K_q are the droop gain parameters. If these droop parameters are set to low values, the system responds more slowly; conversely, higher values enable a faster dynamic response.

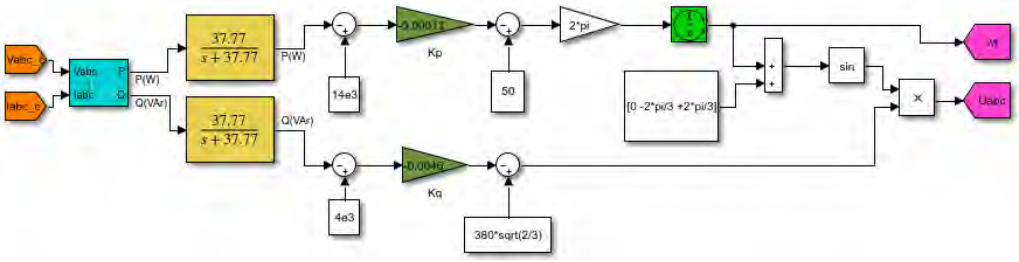

Figure 10 Droop frequency and sinusoidal waveform generation

As illustrated in Figure 10, the calculated input power values are first subjected to filtering and then compared with their respective reference values based on predefined droop coefficients. Subsequently, the resulting control signals are evaluated against the nominal system frequency and terminal voltage. An increase (or decrease) in the measured active power results in a corresponding decrease (or increase) in the output frequency. A similar droop characteristic governs the relationship between reactive power and terminal voltage.

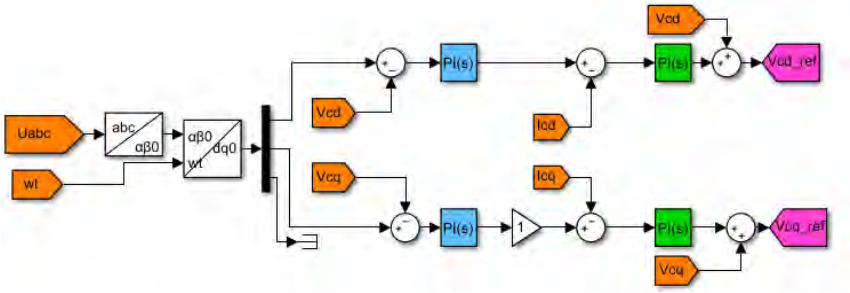

Figure 11 Droop control loops

The obtained terminal voltage (U_{abc}) and the angular frequency (ω_t), which is used for the dq-axis transformations, are fed into the control block illustrated in Figure 11. These signals sequentially pass through the voltage and current control loops, ultimately generating the reference voltages required for PWM signal synthesis. Notably, no Phase-Locked Loop (PLL) block is present in this structure, indicating that synchronization with an existing grid is not required.

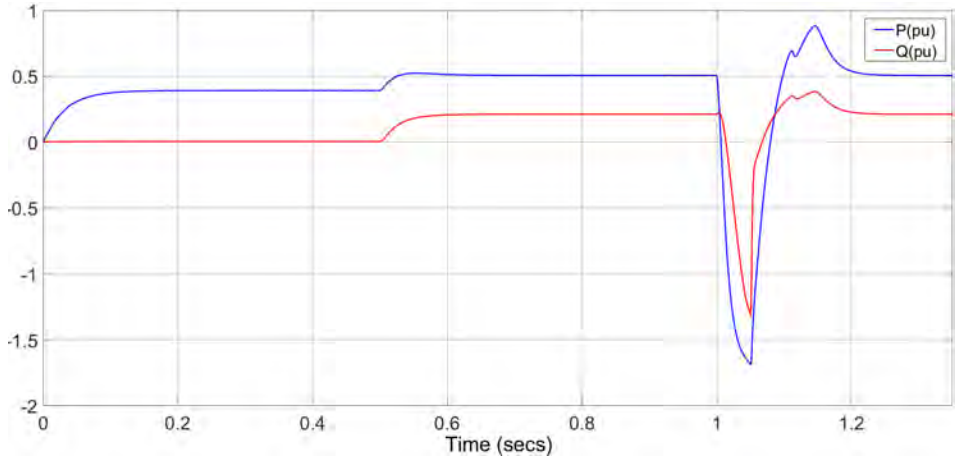

Figure 12 Active and Reactive Power Dynamics in GFM Inverter

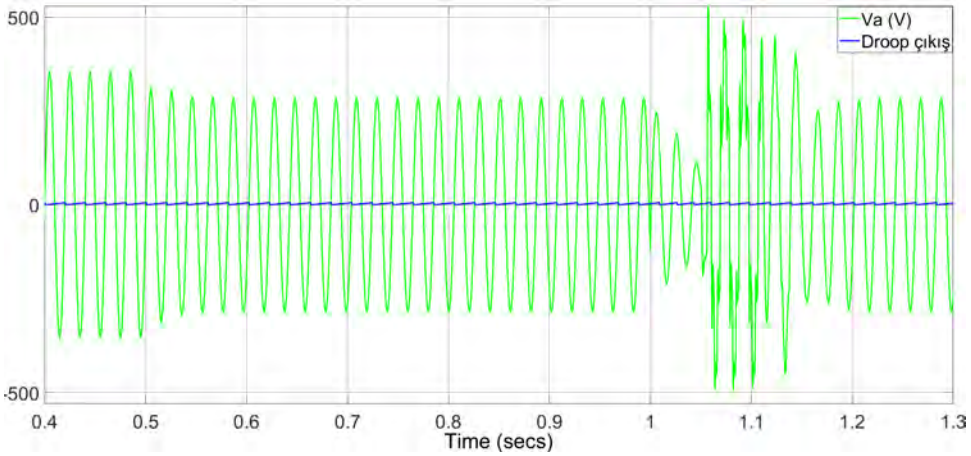

Figure 13 GFM inverter PCC voltage (V_a) and Droop output (w_t)

Initially, the inverter—rated at 14 kW and 4 kVAr (see Figure 10)—supplies a 12 kW load. At t = 0.5 s, an additional load of 12 kW and 10 kVAr is introduced into the system, similar to the scenario in GFL operation. As shown in Figure 12, this additional loading results in an increase in both the active and reactive power output of the GFM inverter. Correspondingly, Figure 14 illustrates a drop in frequency at t = 0.5 s, reflecting the droop mechanism response. This frequency reduction represents the system's dynamic adjustment to accommodate and share the increased load. Furthermore, Figure 15 shows a decrease in terminal voltage due to the increased reactive power demand.

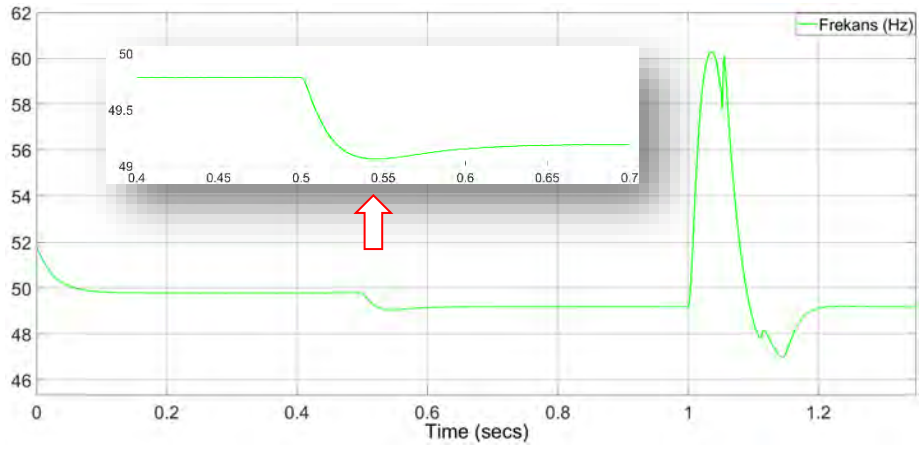

Figure 14 Frequency Deviation Curve (Hz)

Unlike to previous inverter scenario, at t = 1 s, the grid connection is established at the PCC (Point of Common Coupling) within a 50 ms interval; however, in this case, the transition occurs in the opposite direction, i.e., from islanded to grid-connected mode. As observed in the GFL case, the resulting unstable and oscillatory waveforms indicate that both control methods—summarized in Table 1—are complementary in nature, each compensating for the other's limitations under different operating conditions.

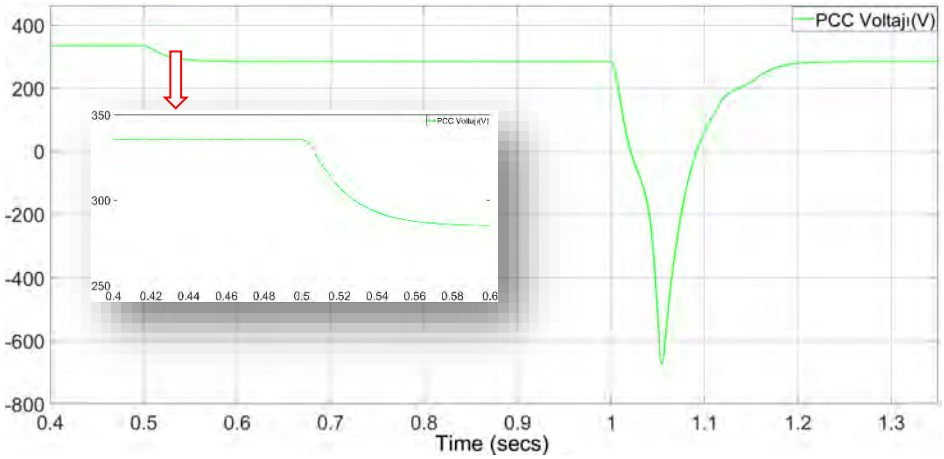

Figure 15 Point of Common Coupling (PCC) voltage deviation profile (V)

Table 1. Detailed Comparison of GFM and GFL Inverters (Mohammed et al., 2024)

Specifications	*Grid-Forming Inverter (GFM)*	*Grid-Following Inverter (GFL)*
Operation	Can operate in islanded mode; generates voltage and frequency independently.	Requires an external grid reference to operate.
Grid Dependency	Operates independently of the grid; can initiate the grid from scratch.	Dependent on the grid for voltage and frequency references.
Control Objective	Regulates voltage and frequency.	Tracks grid voltage and frequency (typically using a PLL).
Inertia	Provides synthetic (virtual) inertia.	Has no inherent inertia; relies on grid inertia.
Applications	Microgrids, islanded systems, weak grids.	Grid-connected systems under stable grid conditions.
Stability	More suitable for weak grids or systems with high renewable energy penetration.	May struggle in weak grids or systems with low inertia.

5. Results and Discussion

Based on the data collected from the literature, the comprehensive Table 1 presents a feature-by-feature comparison of the two main inverter control strategies. In this context, this study simulates droop-based Grid-Forming (GFM) and conventional vector-controlled Grid-Following (GFL) inverters under both islanded and grid-connected scenarios, taking into account various load conditions using MATLAB/Simulink. The respective advantages and limitations of each control method are examined through graphical results under different grid conditions. Notably, the issue of grid dependency highlighted in the table is validated through this study. The inverter control structure, designed to operate either grid-connected or isolated, needs to be carefully designed. Specifically, it is observed that a hybrid control model combining GFM for islanded systems and GFL for grid-connected systems would be beneficial. This model should not be limited to droop control alone but should also incorporate other GFM control strategies available in the literature. Moreover, ensuring smooth and stable transitions between different grid states is identified as a target for future work. Finally, the inclusion of weak grids or rural networks located far from centralized infrastructure is also considered a potential focus in upcoming research.

Declaration of Ethical Standards

As the authors of this study, we declare that he complies with all ethical standards.

Credit Authorship Contribution Statement

F. Burak: Conceptualization, Methodology, Software, Validation, Formal analysis, Writing -Original Draft, Visualization, Writing, Investigation

H. Karaca: Review & Editing, Supervision.

Declaration of Competing Interest

The authors declared that they have no conflict of interest.

Data Availability

No datasets were generated or analyzed during the current study.

References

Ali, M. A., & Arkadan, A. A. (2024, 3-5 April 2024). Dynamic Performance of Grid-forming Inverter Control Techniques - A Comparative Case Study. Paper presented at the 2024 IEEE Green Technologies Conference (GreenTech).

Blaabjerg, F., Teodorescu, R., Liserre, M., & Timbus, A. V. (2006). Overview of Control and Grid Synchronization for Distributed Power Generation Systems. IEEE Transactions on Industrial Electronics, 53(5), 1398-1409.

Gullu, S., Nilian, M., & Batarseh, I. (2024). Enhanced droop control for off-grid and grid-tied scenarios in renewable energy systems. International Journal of Energy Studies, 9(4), 745-773.

Mandrile, F. (2021). Next Generation Inverters Equipped with Virtual Synchronous Compensators for Grid Services and Grid Support. (Ph.D. dissertation). Univ. Politecnico di Torino, Torino.

Mohammed, N., Udawatte, H., Zhou, W., Hill, D., & Bahrani, B. (2024). Grid-Forming Inverters: A Comparative Study of Different Control Strategies in Frequency and Time Domains. IEEE Open Journal of the Industrial Electronics Society, PP, 1-32.

Rathnayake, D., Akrami, M., Phurailatpam, C., Me, S. P., Hadavi, S., Jayasinghe, G., . . . Bahrani, B. (2021). Grid Forming Inverter Modeling, Control, and Applications. IEEE Access, PP, 1-1.

Rathnayake, D. B., Razzaghi, R., & Bahrani, B. (2022). Generalized Virtual Synchronous Generator Control Design for Renewable Power Systems. IEEE Transactions on Sustainable Energy, 13(2), 1021-1036.

Rosso, R., Wang, X., Liserre, M., Lu, X., & Engelken, S. (2021). Grid-Forming Converters: Control Approaches, Grid-Synchronization, and Future Trends—A Review. IEEE Open Journal of Industry Applications, 2, 93-109.

Salem, Q., Aljarrah, R., Karimi, M., & Al-Quraan, A. (2023). Grid-Forming Inverter Control for Power Sharing in Microgrids Based on P/f and Q/V Droop Characteristics. Sustainability, 15(15).

Serkan Aslan, E. I. (2023). Overview of turkish electricity market 2023. Retrieved from https://www.pwc.com.tr/tr/sektorler/enerji/overview-of-turkish-electricity-market-2023.pdf

Sevilmiş, F., & Karaca, H. (2019). Şebeke Etkileşimli Eviriciler Için Faz Kilitleme Döngüsü Yöntemlerinin Performanslarinin Karşilaştirilmasi. [Performance Comparison of Phase Locked Loop Methods for Grid Interactive Inverters]. Konya Journal of Engineering Sciences, 7(4), 713-728.

Tozak, M., Taskin, S., Sengor, I., & Hayes, B. P. (2024). Modeling and Control of Grid Forming Converters: A Systematic Review. IEEE Access, 12, 107818-107843.

Urtasun, I., Urtasun, A., Muguiro, M., & Marroyo, L. (2022, 20-23 June 2022). Dynamic Enhancement of the Droop Control for Grid-Forming Inverters. Paper presented at the 2022 IEEE 23rd Workshop on Control and Modeling for Power Electronics (COMPEL).

Wiatros-Motyka, M. (2023). Global Electricity Review 2023. Retrieved from https://ember-climate.org/insights/research/global-electricity-review-2023.

ELECTRICAL ENGINEERING AND ENERGY

OPEN ACCESS

Evaluation of Magnet Demagnetization Behavior in Permanent Magnet Linear Synchronous Motors

Enes Yücel[1], Mehmet Cunkas[1], Łukasz Knypiński[2]

[1] Electrical & Electronics Engineering, Faculty of Technology, Selcuk University, Konya, Türkiye

[2] Faculty of Control, Robotics and Electrical Engineering, Poznan University of Technology, Poznan, Poland

Submitted: 2 April 2025
Accepted: 25 April 2025
Published: 30 April 2025

Corresponding author
Enes Yucel,
enes.yucel@selcuk.edu.tr

Copyright, Distributed under Creative Commons CC-BY 4.0

Abstract: This paper focus on investigating the demagnetization behavior of permanent magnets in Permanent Magnet Linear Synchronous Motors (PMLSMs) under varying thermal and electrical operation conditions. For this, two complementary Finite Element Method-based approaches are used. The first method utilized magnetostatic analysis to determine the B-H operating points of the magnets under worst-case conditions, allowing the identification of critical regions that tend to move away from the irreversible magnetic field. The second method employed time-domain transient analysis to monitor changes in the induced voltage under varying temperatures and stator current levels. The results revealed that increasing current and temperature significantly reduced the permanent flux density, indicating partial or complete demagnetization. Furthermore, the demagnetization thresholds were shown through safe operating area curves.

Keywords Demagnetization, Permanent Magnet Linear Synchronous Motor, Magnetic Coercivity, Safe Operating

1. Introduction

Permanent Magnet Linear Synchronous Motors (PMLSM) are widely preferred in applications that require high precision, such as laser engravers and 3D printers, thanks to their superior features such as high acceleration, direct drive structure, and precise positioning capability (Song et al., 2017; Yang et al., 2023). However, PMLSM systems are prominent not only in the field of industrial automation but also in medium- and low-speed magnetic train (maglev) applications. Halbach-type PMLSMs, whether coreless or with cores, offer significant advantages over conventional linear induction motors in traction systems due to their high synchronization capability and low operating costs (H. Wang et al., 2018).

Since permanent magnet (PM) motors operate under high temperatures and currents, permanent magnets can easily lose their magnetism. Partial demagnetization reduces the torque and power density of PM motors, while complete demagnetization leads to a complete loss of motor function. To overcome this risk, thicker or higher coercive strength magnets are often used, but this also increases the cost (Xiong et al., 2016). Therefore, the study of the phenomenon of demagnetization in PM motors is of great importance, and many studies have been conducted on this topic.

Mahmouditabar, Vahedi, and Marignetti (2023) elaborated on the basic principles of the concept of demagnetization. Four basic approaches are proposed, such as modelling of nonlinear GH characteristics, analytical evaluation of local demagnetization, and accurate experimental testing methods. Hoang et al. (2024) developed a nonlinear model for the prediction of ID in PMSMs operating under overload and high temperature. They showed that this model provides high agreement with Finite Element Analysis (FEA) and experimental results. Xiong et al. (2016) applied controlled local demagnetization on magnet samples with a specially developed test setup and compared the results with 3D FEA. Eker and Özsoy (2022) experimentally examined the effects of demagnetization failures created at different rates on motor performance and revealed decreases in torque, efficiency, and power factor. Almandoz, Gómez, Ugalde, Poza, and Escalada (2019) proposed a methodology based on finite element analysis and experimental testing, demonstrating how PM machine designs that achieve an optimal balance between cost and durability can be realized.

When the literature in this field is examined, it is seen that demagnetization is mainly considered in permanent magnet synchronous machines (PMSM). In this study, demagnetization trends in permanent magnet linear synchronous motors (PMLSM) are comprehensively investigated based on the deficiency in the literature. Two different analysis approaches are applied in the study. In the first approach, the operating points of the magnets on the B-H curve of the PMLSM under no-load conditions were determined by magnetostatic analysis, and the regions prone to demagnetization were identified. In the second approach, time-dependent transient analysis was applied to evaluate the remanent flux loss of the magnets through the induced voltage (Eq) on the q-axis at different temperature levels and various reverse current conditions. The analyses are carried out by means of FEM-based simulations and the tendency of the magnet material to demagnetize depending on temperature and current is presented in detail using the data obtained. Furthermore, based on the results of the study, safe working areas for magnet selection and motor design are defined, and design recommendations are presented for more efficient operation of PMLSM systems.

2. Demagnetization of Permanent Magnets

There are different causes of demagnetization. If the operating point is in the region where the BH curve runs linearly, there is no demagnetization. However, if the operating point approaches or falls below the "knee point" of the BH curve, partial or irreversible demagnetization may have begun. Therefore, the Remanence flux (B_r) is no longer at the initial value but at a lower value depending on the reverse magnetic field intensity to which it is exposed. This indicates that the magnet cannot maintain its initial remanent value, and some magnetic fields are lost. The operating temperature of the magnet is one of the most important factors affecting the demagnetization coercivity (H_c) and intrinsic demagnetization coercivity (H_{ci}). Magnetic coercivity is a constant material property and is the opposite of the magnetic field strength required to demagnetize a magnet completely. Figure 1 shows the standard BH curve and the point H_c and H_{ci} values corresponding to the point B_r=0 on the intrinsic BH curve. Magnetic Coercivity does not change with increasing current. Coercivity depends on the structure of the material and the operating temperature of the magnet (Üstün, 2000). There are two curves on the magnet BH graph: the intrinsic curve and the normal curve. The red one is the intrinsic curve, and the blue one is the normal curve. The yellow line represents the load line. H_a is the strength of the external magnetic field acting on the magnet. Below the knee point, the magnet loses its magnetizing property.

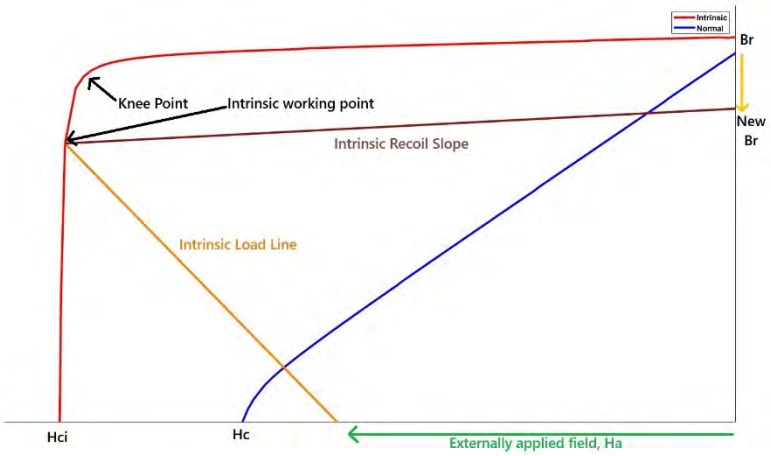

Figure 1 BH Characteristics and demagnetization behavior of sample magnet

Temperature increase and inductive reaction are the leading causes of demagnetization. However, mechanical stresses and eddy currents can also cause magnets to lose their magnetism (S. Wang et al., 2025). One of the most destructive magnetization effects in motors is the Back EMF value, which occurs due to short-circuit currents when the motor rotates at synchronous speed (Hanselman, 2003). In this study, detailed analyses were carried out on the permanent magnet mounted in runner of a designed PMLSM. The investigations were carried out to reveal the demagnetization tendencies that the magnet may be exposed to under high reverse currents and temperature increases under worst-case conditions. Comprehensive simulations were carried out using the FEA. The changes in the flux density (B) value during the demagnetization process of the magnet material were evaluated through the B-H characteristic. Since increasing operating temperature and stator current increase the risk of demagnetization of the magnet, these parameters need to be carefully monitored and limited. A magnet sample is shown in Figure 2-a, and magnetic equivalent circuit models are shown in Figure 2-b.

The magnetomotive force is the total magnetic voltage difference between the ends of the permanent magnet, and it is calculated as follows.

$$F = \emptyset_r * R_m \tag{1}$$

where $\emptyset_r$ is the magnetic flux generated by the single magnet, and R_m [A/Wb] is the total reluctance of the magnetic circuit.

Considering the electromagnetic conversion laws, the magnetomotive force can be also defined.

$$F = H * l_m \tag{2}$$

where H [A/m] is magnetic field intensity, l_m [m] is the magnetic path length of the magnet. The magnetomotive force (MMF) resulting from the passage of current through a coiled winding is defined as follows.

$$F = N * I \tag{3}$$

where N is the total number of turns, and I is the current flowing through the winding. Accordingly, the MMF statement.

$$H = \frac{N*I}{h_{pm}} \tag{4}$$

$$N * I = \emptyset_r * R_m = \frac{B_r * l_m}{\mu_0 * \mu_r} \tag{5}$$

Total flux linkage of a phase:

$$\lambda = N * \emptyset \tag{6}$$

Magnetic flux value per pole for PMLSM:

$$\emptyset = \frac{\frac{2}{\pi} B_{airgap} L_s W_s}{p} \quad (7)$$

where L_s and W_s are the width and length dimensions of the motor. Magnetic flux density is:

$$B = \mu * H \quad (8)$$

Stator reference frame d-q currents.

$$i_{d_srf} = I_s \cos(\alpha_{Is_srf}) \text{ and } i_{q_srf} = I_s \sin(\alpha_{Is_srf}) \quad (9)$$

Reference frame currents a,b,c according to the Inverse Clarke Transform.

$$i_a = i_{d_srf}, \quad i_b = -\frac{1}{2} i_{d_srf} + \frac{\sqrt{3}}{2} i_{q_srf}, \quad i_c = -\frac{1}{2} i_{d_srf} - \frac{\sqrt{3}}{2} i_{q_srf} \quad (10)$$

In this study, the NdFeB class magnet was preferred in the single-sided PMLSM design. The main reason for this preference is that the magnet in question has a high permanent flux density and energy multiplier, allowing more compact motor designs compared to other magnets of similar power. A total of 16 magnets are placed on the secondary of the motor, with opposite poles side by side, in line with the structure shown in Figure 3. Detailed magnetic characteristics of the magnet used are presented in Table 1.

Table 1 Properties of the N38UH 150C permanent magnet material used in the design

Parameter	Type	Value	Unit
Relative permeability	Nonlinear	B-H Curve	-
Bulk conductivity	Simple	555555.5556	siemens/m
Magnetic coercivity (H_C)	Vector	-922100	A/m
Mass density of core	Simple	7500	kg/m³
Remanence flux	Simple	1.0634	T
Max. working temp.	Simple	150	℃

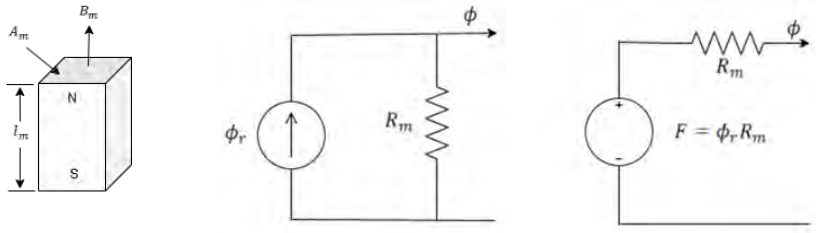

(a) (b)

Figure 2 a-) Sample of permanent magnet b-) Norton and Thevenin magnetic equivalent circuits

3. Analysis of demagnetization in PMLSM design

In this study, two methods were applied in demagnetization analysis. Firstly, demagnetization due to overload under worst-case conditions was investigated. In the analysis, the magnetic field distributions of PMLSM under worst-case conditions were obtained with a magnetostatic solvent. The operating points on the B-H curve of a selected magnet on the secondary were determined and shown in the figure. Then, demagnetization due to temperature rise was investigated. A three-phase time-dependent transient analysis was performed for a single magnet. In this context, the demagnetization tendencies of magnets with different

temperature levels under different current conditions were examined, and the effects of demagnetization were analyzed, especially considering the change in E_q value.

3.1 Analysis of demagnetization caused by overload

The B and H distributions obtained because of the no-load analysis of the magnet located in the primary of the PMLSM and marked in the circle are presented in Figure 3. When the B and H magnetic flux distributions on the PMLSM are analyzed separately, comments can be made due to the magnet-material interaction. Accordingly, it is seen that the B value is higher at the ends of the magnet and lower in the center. The reason for this is that the magnetic flux density accumulates at the ends of the magnet, and the magnetic flux starts inside the magnet and goes out from the ends. In Figure 3, the magnetic field strength is maximum in the center of the magnet as the largest MMF is formed. Towards the end, H decreases because the leakage fields become larger. Although the magnetic flux density is directed toward the ends of the magnet, the field generating power is low there because there is MMF loss at the ends, and the H (A/m) value is low. Therefore, demagnetization is easier in these regions.

In the study, analyses were carried out at various current levels using Ansys Maxwell 2D Magnetostatic solver. The type of magnet used is Arnold Magnetics N38UH 150C. The analyses were repeated for no-load ($1.I_{s_pu}$) and loaded/loading operation state ($5.I_{s_pu}$, $9.I_{s_pu}$, $13.I_{s_pu}$, $17.I_{s_pu}$, $20.I_{s_pu}$). The analysis was positioned along the magnet with respect to the distance axis for each parameter, and three graphs were obtained. Accordingly, Figure 4-a shows the average magnetic flux density at the magnet (B_{magnet}), Figure 4-b shows the magnetic field strength at the center of the magnet (H_{magnet}), and Figure 4-c shows the average magnetic flux density in the air gap ($B_{air\ gap}$).

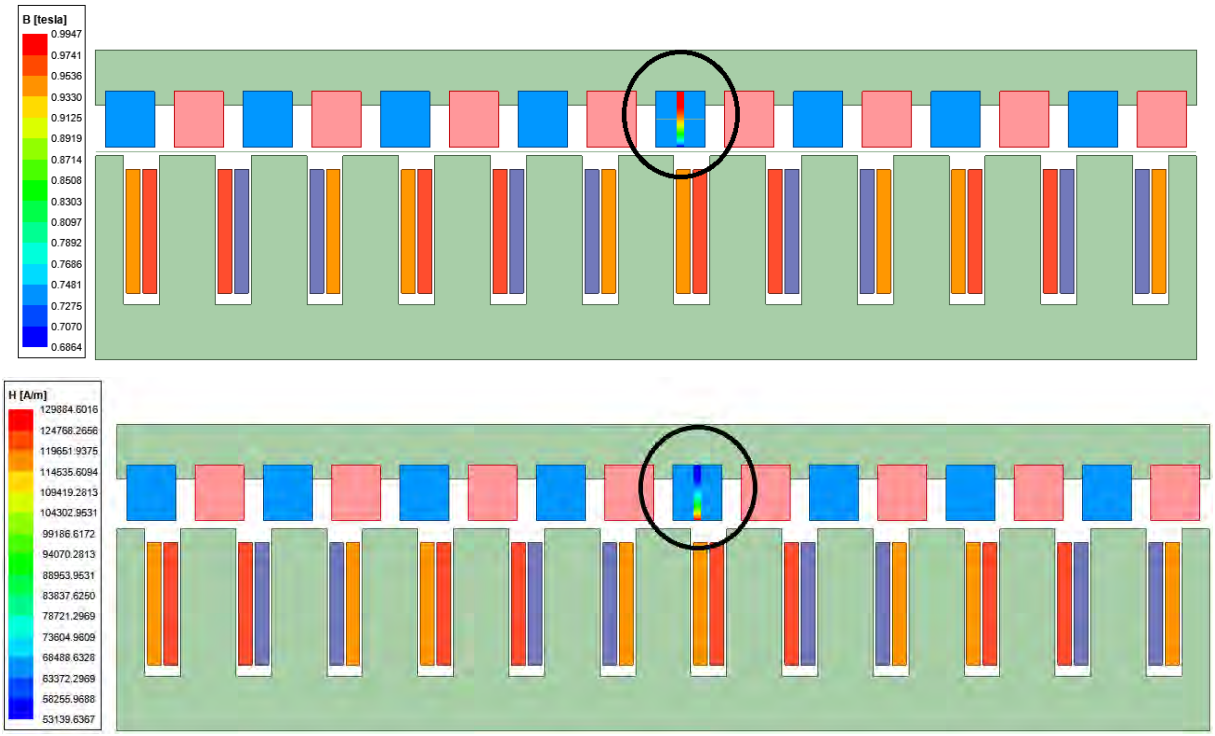

Figure 3 B and H distribution obtained from the no-load analysis

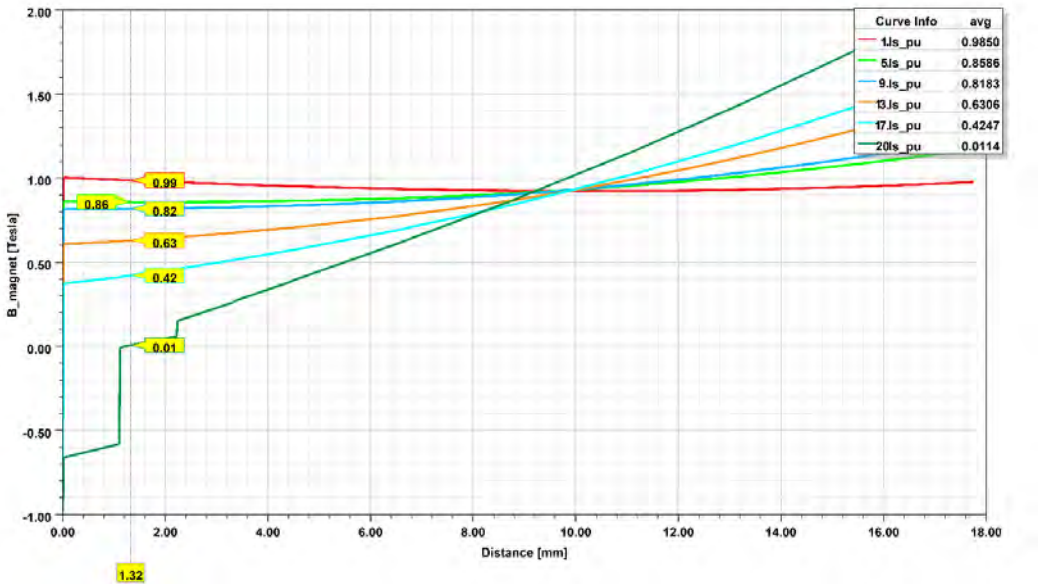
Curve Info
avg
1.Is_pu 0.9850
5.Is_pu 0.8586
9.Is_pu 0.8183
13.Is_pu 0.6306
17.Is_pu 0.4247
20.Is_pu 0.0114
0.99
0.86
0.82
0.63
0.42
0.01
1.32
B_magnet [Tesla]
Distance [mm]

(a)

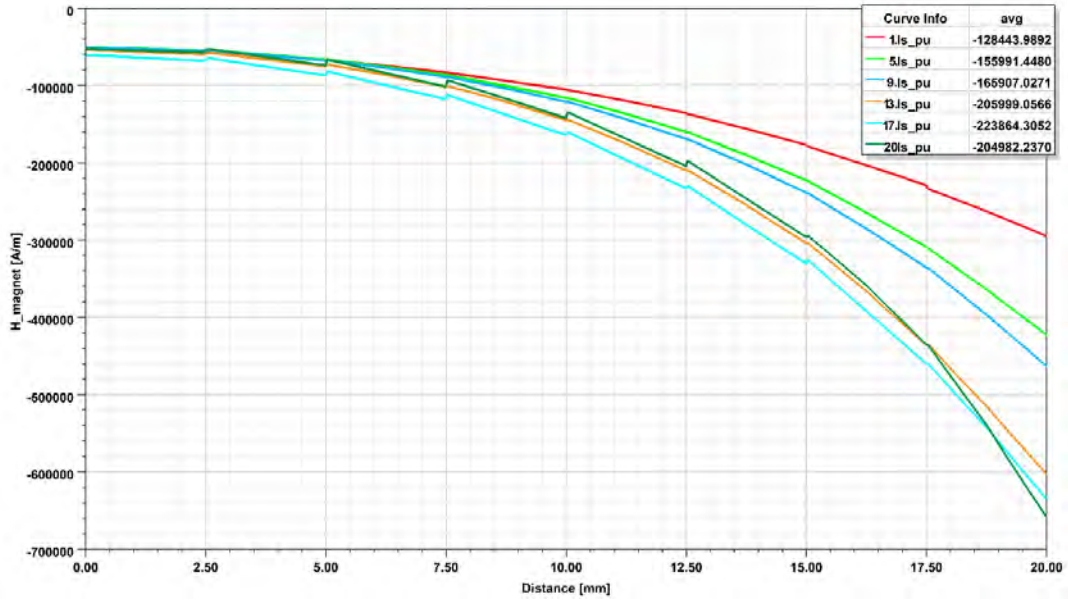
Curve Info
avg
1.Is_pu -128443.9892
5.Is_pu -155991.4480
9.Is_pu -165907.0271
13.Is_pu -205999.0566
17.Is_pu -223864.3052
20.Is_pu -204982.2370
H_magnet [A/m]
Distance [mm]

(b)

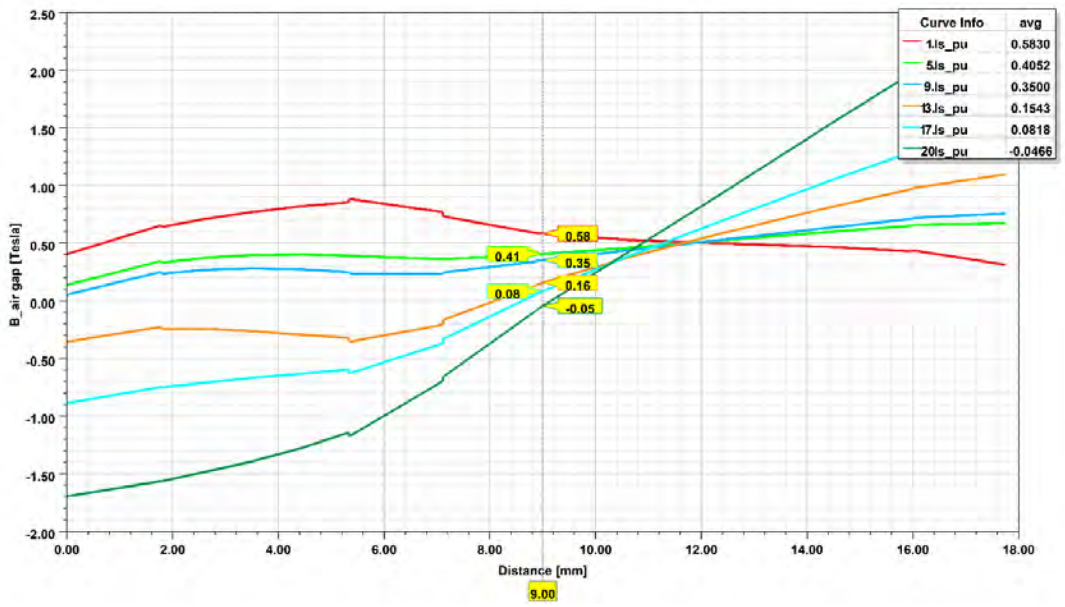

(c)

Figure 4 Results of comparison along the length of the magnet a) Average magnetic flux density b) Magnetic field intensity at the center of the magnet c) Average magnetic flux density in the air gap

While H_{magnet} value is around -128,000 A/m at no-load operation, the H value becomes more negative as the load increases, reaching -610,000 A/m at 20.I_(s_pu) current. This shows that as the reversing current passing through the stator winding increases, the reversing H value in the magnet increases and approaches the coercive force of the magnet. While $B_{magnet} = 0.99\ T$ at no-load operation, this value decreased to 0.86 T, 0.82 T, 0.63 T, 0.42 T and 0.01 T, respectively, as the current increased. Especially at $20.I_{s_pu}$, the B_{magnet} value approaches almost zero, indicating that the magnet is severely demagnetized. The $B_{air\ gap}$ value in the air gap also decreases with the load. This decrease indicates that the magnetic field generated by the magnet is weakened by the reverse current flowing through the stator windings, and as a result, the total net magnetic flux in the air gap may decrease. This makes it difficult for the motor to operate correctly. In a motor with a loss of magnetization, the stator current must be increased to achieve the same electromagnetic torque. This creates serious problems for thermal insulation and significantly shortens the life of the motor (Gyftakis, Ab Rasid, Skarmoutsos, & Mueller, 2021).

The simulation results were utilized to determine the working points on the B-H curve of the magnet analyzed in the PMLSM. Based on the analysis, the H_{magnet} and the corresponding B_{magnet} values, measured at the center of the magnet, were identified as the working points for the specified load conditions and are presented in Figure 5.

When the graph is examined, it is observed that at low current levels, such as I_{s_pu}, the magnet still operates within the linear region. After the value, the working points move into the region where the slope of the curve decreases, approaching partial saturation or the demagnetization zone. As seen from the graph, the B_r value of the magnet is 1.06 Tesla. At the $20.I_{s_pu}$ level, the working point drops below the knee point of the B-H curve, indicating that the magnet is significantly stressed and irreversible demagnetization may have occurred. When B_{magnet} is 0.01T, $H_{magnet} = -739{,}434\ A/m$ is -739.434 a/m, which corresponds to the intrinsic coercivity point H_{ci} where full demagnetization occurs. Therefore, it can be concluded from the graph that the magnet retains its magnetization until the reverse magnetic field reaches -739 kA/m.

Furthermore, the graph clearly illustrates how the working points approach the demagnetization region as the magnet is subjected to negative H_{ci} fields. To avoid reaching this critical limit, the MMF value can be constrained, or the magnet thickness can be increased, as indicated in Equation 6.

3.2 Analysis of demagnetization caused by temperature increase

Three-phase transient analysis was performed, and E_q was monitored for the rotor reference frame. The mathematical expression of E_q is given as:

$$E_q = \omega_e * \lambda_M \tag{11}$$

where ω_e represents the electrical angular velocity of the rotor (rad/s), and λ_M denotes the flux linkage of the magnet, which is predominantly defined along the d-axis. As can be understood from the equation, when no current is applied to the stator windings ($I_d = 0$, $I_q = 0$) under a constant electrical angular velocity, the windings do not generate any magnetic field, and all the magnetic flux in the system originates solely from the permanent magnets. Therefore, E_q is directly proportional to the magnet flux. During the analysis process, the remanent flux linkage λ_M cannot be directly measured, but E_q can be measured. Thus, demagnetization detection was carried out by tracking the E_q voltage. The simulation procedure was structured into three periods: initially, the motor was operated under no-load conditions, followed by the application of loaded operation, and finally, the system was returned to the no-load state. This approach enabled a comparative evaluation of magnet behavior before and after loading.

In the first period, when no current is applied to the system, the stator current vector angle between the stator current vector and the stator d-axis (α_{Is_srf}) is set to 90 degrees, and only the magnet-induced voltage (E_{q1}) is generated. In this condition, as illustrated in Figure 6, the magnet flux λ_M, aligned along the d-axis in the rotor reference frame, produces an E_q voltage along the q-axis. This induced voltage is designated as the reference point E_{q1} for subsequent comparative analyses.

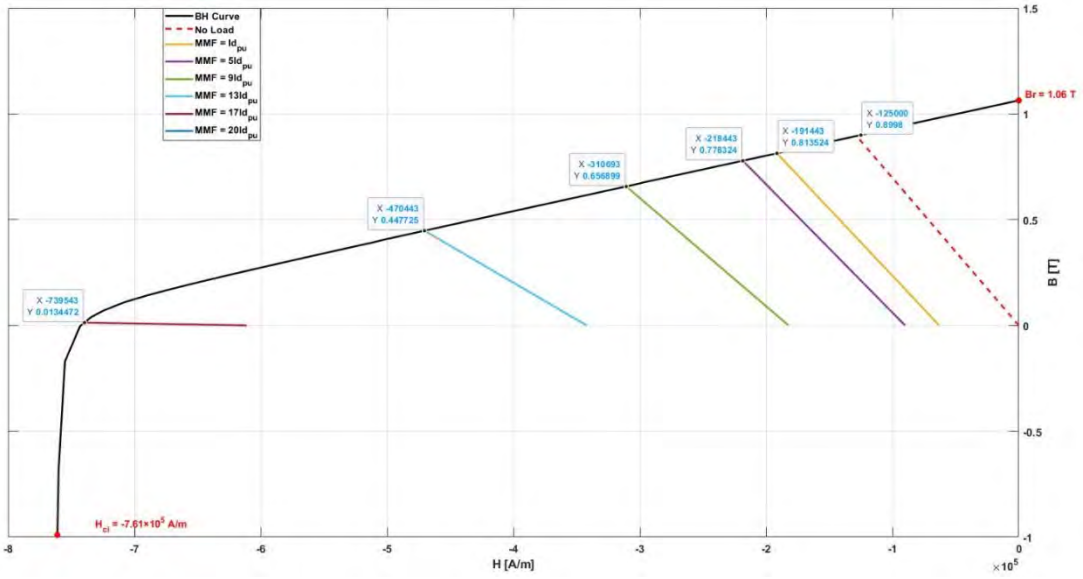

Figure 5 B-H Curve of the Magnet for Operating Points at Different Load Conditions

In the second period, as shown in Figure 7, current is applied such that the stator current vector angle α_{Is_srf} is 180 degrees in the rotor reference frame. This creates a stator magnetic field density (B_S) directly opposing the magnet flux. In this worst-case scenario for the magnets, the λ_M value weakens, resulting in a decrease in theE_q voltage. The analysis was repeated for various load conditions (1.I_{s_pu}, 5.I_{s_pu}, 9.I_{s_pu}, 13.I_{s_pu}, 17.I_{s_pu}, 20.I_{s_pu}) and for magnets with three different operating temperature classes: Arnold Magnetics N38UH 80C, Arnold Magnetics N38UH 120C, and Arnold Magnetics N38UH 150C.

In the third period, I_{s_pu} is reset to zero. During this phase, the obtained E_{q3} value is compared with E_{q1} to detect demagnetization. If $E_{q1} = E_{q3}$, it indicates that the magnet has not been permanently affected, the system has remained within the linear region of the B-H curve, and the B_r value has not changed. However, if $E_{q3} < E_{q1}$, it indicates that the magnet has undergone demagnetization and a permanent flux loss has occurred. During demagnetization, a new B_r value is formed, and this new remanent flux density is reached along the intrinsic recoil slope.

As a result of the analyses performed with these parameters, the graphs presented in Figure 8 were obtained. In the tables embedded within the graphs, the "avg." value corresponds to the voltage induced by the magnet in the coils during the first period when no current is applied. The "avg_1" value refers to the induced voltage measured during the third period after the application of high currents. Since magnets lose their energy with increasing temperature, this behavior is directly related to their demagnetization temperature. A lower operating temperature for the magnet reduces the risk of demagnetization. For most magnets, both the remanent flux density and the magnetic coercivity decrease with increasing temperature (Campbell, 1996). Simulations were repeated for three types of magnets characterized by different temperature classes (80^0C, 120^0C, and 150^0C). According to Figure 8a, for the low-temperature class magnet (20C), E_{q3} remains approximately equal to E_{q1} at low I_{s_pu} levels, but as the current increases, E_{q3} deviates from E_{q1}. As shown in Figure 8b, for the medium-temperature class magnet (120^0C), at higher I_{s_pu} levels, E_{q3} becomes significantly lower than E_{q1}, indicating the appearance of an intrinsic recoil slope. In Figure 8c, this difference is even more pronounced for the high-temperature class magnet (150C). At 20.I_{s_pu}, E_{q3} shows a substantial drop compared to E_{q1}, suggesting that the magnet has fallen below its knee-point and can no longer maintain its initial B_r value. According to the analysis, for the same I_{s_pu} level, magnets with higher operating temperatures exhibit lower E_q values and, thus, lower B_r values. FEM analysis was performed on three different magnets, and B_r values decreased gradually as the operating temperatures of the demagnetized magnets increased.

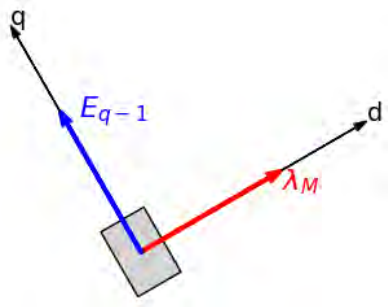

Figure 6. Vector representation of E_{q1} induced by the permanent magnet flux under no-load condition

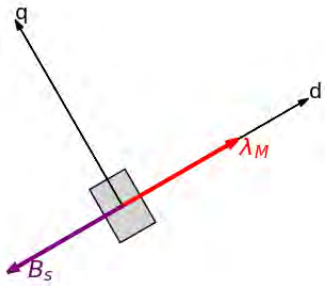

Figure 7 Vector diagram of the stator magnetic field B_S opposing the magnet flux at α_{Is_srf} = 180°

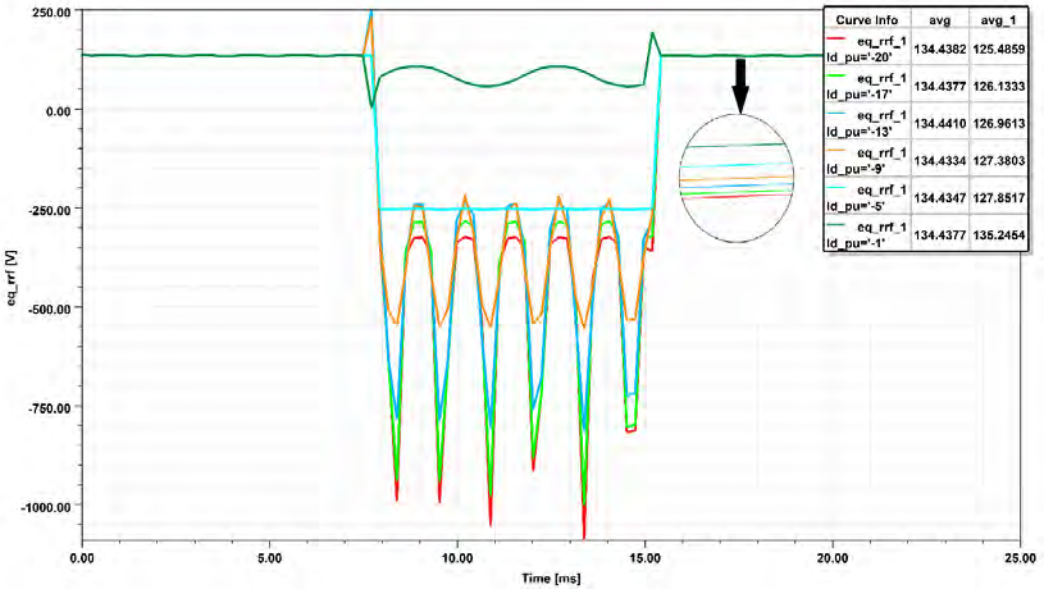

(a)

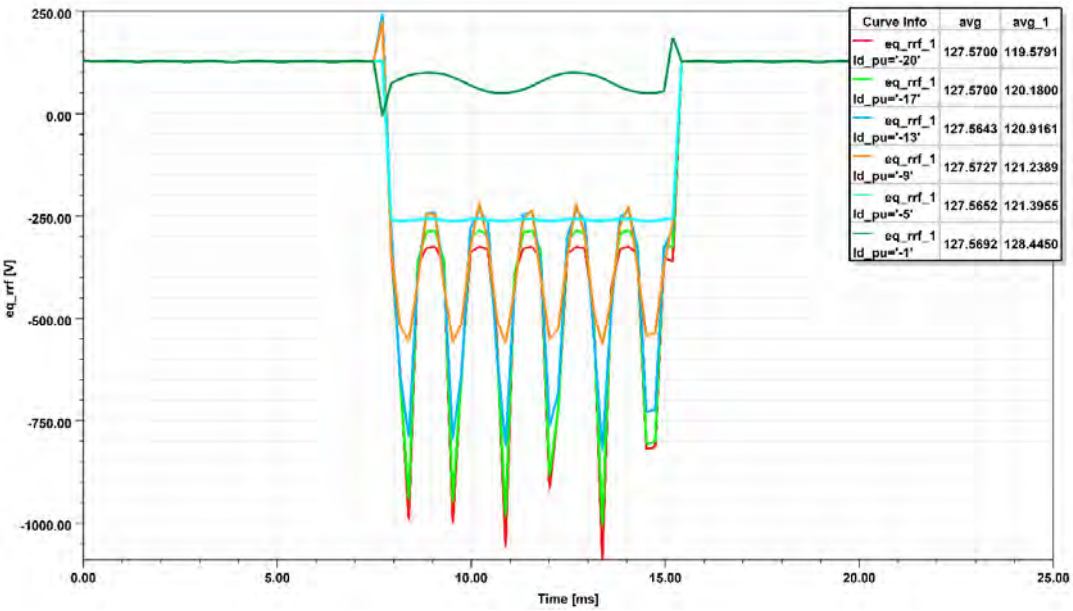

(b)

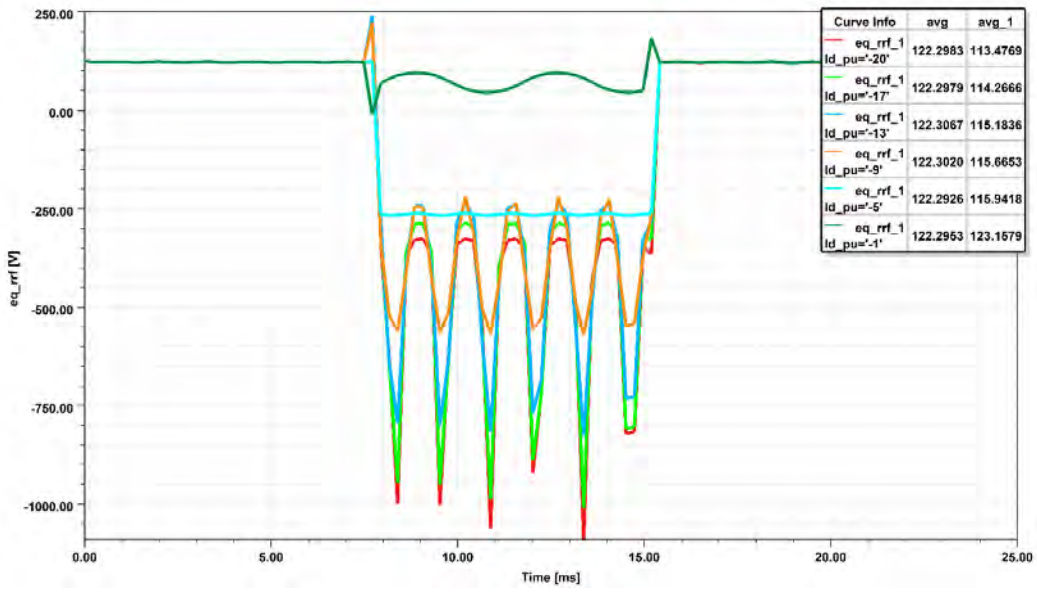

(c)

Figure 8 Time dependent variation of Eq voltages obtained at different I_{s_pu} levels. a-) for 80C magnet b-) for 120C magnet c-) for 150C magnet

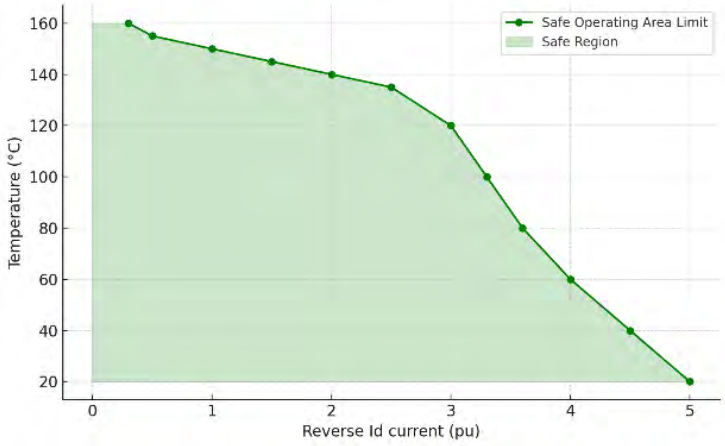

Figure 9 Safe operating area

Additionally, the resulting graphs demonstrate that with increasing temperature, the magnet becomes demagnetized at lower reverse current levels. As a result of these analyses, a Safe Operating Area (SOA) graph was obtained, which determines the safe operating limits in terms of motor design, as shown in Figure 9. The area under the graph represents the safe operating area without the risk of demagnetization. This graph allows a more accurate selection of the magnet class to be used in PMLSM design.

4. Conclusions

In this study, the demagnetization tendencies of permanent magnets in a PMLSM under overload and temperature rise conditions were evaluated through both the BH curve and the E_q voltage. The results indicate that as the temperature increases, PM experience irreversible magnetic losses at lower reverse current levels. The comparison between E_{q1} and E_{q3} emerges as a simple yet effective method for detecting demagnetization. Furthermore, the progression of the operating points on the BH curve directly reveals

whether the magnet has fallen below its "knee point". Through this PMLSM-specific design study, the critical thresholds for magnets under temperature rise due to motor operation and potential short-circuit current scenarios were identified, and a corresponding SOA diagram was established. Future research can focus on the optimization of the MMF value and magnet sizing to ensure safer and more efficient operation of the motor. In future research, we will combine the developed mathematical model of the PMLSM developed in Ansys with the optimization algorithm. Next, the optimization will be carried out.

Declaration of Ethical Standards

As the authors of this study, we declare that he complies with all ethical standards.

Credit Authorship Contribution Statement

E.Yucel: Conceptualization, Methodology, Software, Validation, Formal analysis, Writing -Original Draft, Visualization.
M. Çunkaş: Investigation, Resources, Writing, Review & Editing, Supervision, Funding acquisition.
Ł. Knypiński: Writing, Review & Editing.

Declaration of Competing Interest

The authors declared that they have no conflict of interest.

Funding / Acknowledgements

The authors were supported within the scope of the research by the Selcuk University Scientific Research Projects Unit with Project No: 24111004.

Data Availability

No datasets were generated or analyzed during the current study.

References

Almandoz, G., Gómez, I., Ugalde, G., Poza, J., & Escalada, A. J. (2019). Study of demagnetization risk in PM machines. *IEEE Transactions on Industry Applications, 55*(4), 3490-3500.

Campbell, P. (1996). Permanent magnet materials and their application.

Eker, M., & Özsoy, M. (2022). Effect of demagnetization faults on line start AF-PMSM performance. *Journal of Power Electronics, 22*(6), 1001-1009.

Gyftakis, K. N., Ab Rasid, S., Skarmoutsos, G. A., & Mueller, M. (2021). The demagnetization harmonics generation mechanism in permanent magnet machines with concentrated windings. *IEEE Transactions on Energy Conversion, 36*(4), 2934-2944.

Hanselman, D. C. (2003). *Brushless permanent magnet motor design*: The Writers' Collective.

Hoang, D.-T., Nguyen, M.-D., Kim, S.-M., Bang, T.-K., Kim, Y.-J., Shin, K.-H., & Choi, J.-Y. (2024). Irreversible Demagnetization Prediction Due to Overload and High-Temperature Conditions in PMSM Based on Nonlinear Analytical Model. *IEEE Transactions on Energy Conversion*.

Mahmouditabar, F., Vahedi, A., & Marignetti, F. (2023). The demagnetization phenomenon in PM machines: principles, modeling, and design considerations. *IEEE Access, 11*, 47750-47773.

Song, J., Dong, F., Zhao, J., Lu, S., Dou, S., & Wang, H. (2017). Optimal design of permanent magnet linear synchronous motors based on Taguchi method. *IET Electric Power Applications, 11*(1), 41-48.

Üstün, Ö. (2000). Sürekli Mıknatıslı Baskılı Devre Endüvili Doğrusal Fırçasız Doğru Akım Motoru Tasarımı.

Wang, H., Li, J., Qu, R., Lai, J., Huang, H., & Liu, H. (2018). Study on high efficiency permanent magnet linear synchronous motor for maglev. *IEEE Transactions on Applied Superconductivity, 28*(3), 1-5.

Wang, S., Chen, J., Yang, J., Zhang, C., Qiu, S., Liu, K., & Lyu, B. (2025). Analysis of Temperature Rise in Short-Term High Overload Torque Motor with LPTN Considering Demagnetization and Saturation. *IEEE Transactions on Energy Conversion*.

Xiong, H., Zhang, J., Degner, M. W., Rong, C., Liang, F., & Li, W. (2016). Permanent-magnet demagnetization design and validation. *IEEE Transactions on Industry Applications, 52*(4), 2961-2970.

Yang, D,. Feng, H., Zhang, W., Zhang, H., & Xu, X. (2023). Design and Optimization of Permanent Magnet Linear Synchronous Motor for Direct Drive Multi-car Elevator Variable Rail System. *IEEE Transportation Electrification Conference and Expo,* Chiang Mai, Thailand, 28 November 2023 - 01 December 2023.